

AFAL-TR-76-35



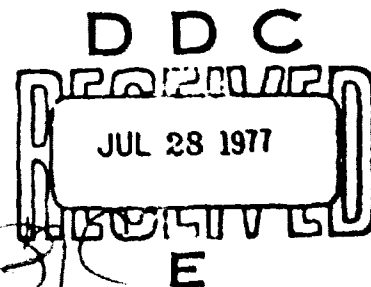
AD A 042253

STUDIES OF Na_2KSb (Cs) PHOTOCATHODES

*ELECTRICAL ENGINEERING DEPARTMENT
UNIVERSITY OF MINNESOTA*

MAY 1977

TECHNICAL REPORT AFAL-TR-76-35
FOR PERIOD JULY 1972 - MAY 1975



Approved for public release; distribution unlimited

AD No. _____
DDC FILE COPY

AIR FORCE AVIONICS LABORATORY
AIR FORCE WRIGHT AERONAUTICAL LABORATORIES
AIR FORCE SYSTEMS COMMAND
WRIGHT-PATTERSON AIR FORCE BASE, OHIO 45433

Best Available Copy

NOTICE

When Government drawings, specifications, or other data are used for any purpose other than in connection with a definitely related Government procurement operation, the United States Government thereby incurs no responsibility nor any obligation whatsoever; and the fact that the government may have formulated, furnished, or in any way supplied the said drawings, specifications, or other data, is not to be regarded by implication or otherwise as in any manner licensing the holder or any other person or corporation, or conveying any rights or permission to manufacture, use, or sell any patented invention that may in any way be related thereto.

This Technical Report has been reviewed and is approved for publication.

This report has been reviewed by the Information Office (OI) and is releasable to the National Technical Information Service (NTIS). At NTIS, it will be available to the general public, including foreign nations.

Clyde L. Woodard
 CLYDE L. WOODARD, Chief
 Electro-Optic Detectors Group
 Electro-Optics Technology Branch

FOR THE COMMANDER

William C. Schoonover
 WILLIAM C. SCHOONOVER, Chief
 Electro-Optics Technology Branch
 Electronic Technology Division

ACCESSION for	
NTIS	White Section <input checked="" type="checkbox"/>
DOC	Bull Section <input type="checkbox"/>
UNANNOUNCED	<input type="checkbox"/>
JUSTIFICATION	
BY	
DISTRIBUTION/AVAILABILITY CODES	
ENTER	AND/OR SPECIAL
A	

Copies of this report should not be returned unless return is required by security considerations, contractual obligations, or notice on a specific document.

7 Tech. Rep. 15. 72-31 Aug 75

UNCLASSIFIED

SECURITY CLASSIFICATION OF THIS PAGE (When Data Entered)

REPORT DOCUMENTATION PAGE		READ INSTRUCTIONS BEFORE COMPLETING FORM	
1. REPORT NUMBER AFAL-TR-76-35	2. GOVT ACCESSION NO.	3. RECIPIENT'S CATALOG NUMBER	
4. TITLE (and Subtitle) Studies of $\text{Na}_2\text{KSb}(\text{Cs})$ Photocathodes		5. TYPE OF REPORT & PERIOD COVERED Technical Report July 1/72 - May 31/75	
		6. PERFORMING ORG. REPORT NUMBER	
7. AUTHOR(s) Paul A. Lindfors		8. CONTRACT OR GRANT NUMBER(s) F33615-72-C-2105	
9. PERFORMING ORGANIZATION NAME AND ADDRESS University of Minnesota, Dept of Electrical Engr Minneapolis, Minn. 55455		10. PROGRAM ELEMENT, PROJECT, TASK AREA & WORK UNIT NUMBERS 2001-03-4	
11. CONTROLLING OFFICE NAME AND ADDRESS AFAL/DHO-3 Wright-Patterson AFB, OH 45433		12. REPORT DATE May 77	
		13. NUMBER OF PAGES 145 (12) 133 p.	
14. MONITORING AGENCY NAME & ADDRESS (if different from Controlling Office)		15. SECURITY CLASS. (if this report) UNCLASSIFIED	
		15a. DECLASSIFICATION/DOWNGRADING SCHEDULE n/a	
16. DISTRIBUTION STATEMENT (for this Report) Approved for public release; distribution unlimited.			
17. DISTRIBUTION STATEMENT (for the abstract entered in March 20, if different from Report)			
18. SUPPLEMENTARY NOTES			
19. KEY WORDS (Continue on reverse side if necessary and identify by block number) Photocathode Photoemission Auger LEED AES Tri Alkaline			
20. ABSTRACT (Continue on reverse side if necessary and identify by block number) More than 15 years after its discovery, $\text{Na}_2\text{KSb}(\text{Cs})$ remains an important photocathode material, but control of its formation remains a problem. In these studies Auger electron spectroscopy (AES) was used to determine the atomic species present in the surface region during formation of $\text{Na}_2\text{KSb}(\text{Cs})$ films. It was found that the electron bombardment incidental to the use of the			

DD FORM 1473 1 JAN 75 EDITION OF 1 NOV 65 IS OBSOLETE

UNCLASSIFIED

SECURITY CLASSIFICATION OF THIS PAGE (When Data Entered)

233 630

UNCLASSIFIED

SECURITY CLASSIFICATION OF THIS PAGE(When Data Entered)

AES technique could cause sample changes, but this problem was eliminated for samples that were heated during or after constituent depositions. Important conclusions derived from these studies are as follows:

1. Heating to temperatures $> 200^{\circ}\text{C}$ at the $2\text{Na} + \text{K}_3\text{Sb} \rightarrow 2\text{K} + \text{Na}_2\text{KSb}$ stage of formation is probably required to produce antimony-rich material, if formation is approached from an alkali-rich standpoint. Alkali antimonide photocathodes of high sensitivity are thought to be $\text{p}^{\text{+}}$ type due to an excess of antimony.

2. The relative populations of the constituents are factors in determining which alkali species will leave when an alkali antimonide film is heated.

3. An alkali overlayer can exist on an alkali antimonide sample that is alkali-deficient in the bulk.

4. An alkali overlayer is probably present on photocathodes of high sensitivity, and Cs is probably present in that overlayer.

5. The output of an alkali metal source (Na, K, or Cs) can be contaminated by other alkali species, and this could be a source of control problems.

6. Oxygen is not a required constituent of photocathodes of high sensitivity.

UNCLASSIFIED

SECURITY CLASSIFICATION OF THIS PAGE(When Data Entered)

PREFACE

The research described in this report was carried out in the Physical Electronics Laboratory of the University of Minnesota under Contract No. F33615-72-C-2105 - Project 2001, Task 03, Work Unit 31, between July 1, 1972 and May 31, 1975. The work was supervised by W. T. Peria, Professor of Electrical Engineering, University of Minnesota, Minneapolis, Minnesota. The project monitor is W. H. Nelson, AFAL/DHO Air Force Avionics Laboratory, Wright-Patterson Air Force Base, Ohio. The report was submitted by the authors on October 12, 1975.

TABLE OF CONTENTS

	Page
I. Introduction	1
1. History of photocathodes through discovery of $\text{Na}_2\text{KSb}(\text{Cs})$	1
2. Factors affecting photoemission from semi-conductors	1
3. Comparison of $\text{Na}_2\text{KSb}(\text{Cs})$ with new generation photocathodes	3
4. Related research	4
5. Typical formation schedule for $\text{Na}_2\text{KSb}(\text{Cs})$ photocathodes	6
6. Motivation for these studies	7
II. Experimental Apparatus and Techniques	8
1. Vacuum system and processing	8
2. Substrate	8
a. Manipulator assembly and substrate design	8
b. Positioning procedures	9
c. Heating and temperature measurement	10
d. Sputter cleaning	10
3. Deposition chamber and constituent sources	11
a. Deposition chamber	11
b. Antimony source	11
c. Alkali metal sources	12
d. Chamber and source degassing	13
e. Deposition monitoring	14
4. Photoemission measurements	14
a. Optics system and calibration	14
b. Accuracy of quantum yield measurements	16
c. Energy distributions of photoelectrons	17

TABLE OF CONTENTS (cont'd.)

	Page
5. Auger electron spectroscopy (AES)	17
a. General description of AES	17
b. AES spectra particular to these studies	18
c. Depth sensitivity of AES and sensitivity of AES to constituents	18
6. Schedule of deposition and analysis used in these studies	19
7. Transmission mode and reflection mode utilization of photocathode	21
III. Results and Discussion	22
1. Monitoring sample formation via photoemission	22
2. Substrate effects	23
3. Sb depositions	26
4. Alkali depositions	27
5. Sample uniformity	30
6. Effect of AES analysis on samples	32
7. AES results and bulk conditions	35
a. Information contained in AES results concerning bulk conditions	35
b. Calibration of the Sb AES peak vs. the alkali/antimony ratio	36
c. The alkali/antimony ratio as a function of heating	37
d. The alkali/antimony ratio of the sample with the highest spectral yield	40
8. Stability of the alkali constituents with the deposition of other alkali species and heating	41
IV. Conclusions and suggestions for continued investigations	45
REFERENCES	48

LIST OF ILLUSTRATIONS

- Figure 1 Energy band diagram for an ideal semiconductor at 0°K.
- Figure 2 Energy band diagrams for two semiconductor materials with differing E_A/E_G ratios.
- Figure 3 Energy band diagrams showing result of band bending on E_{Aeff} for "n" and "p" type semiconductor materials.
- Figure 4 Spectral yield curves for $Na_2KSb(Cs)$.
- Figure 5 Spectral yield curves for $Na_2KSb(Cs)$, GaAs-Cs-O, and Si-Cs-O photocathods.
- Figure 6 B Electron energy band diagram for $Na_2KSb(Cs)$.
- Figure 7 Phases present in the $Na_{3-x}K_xSb$ system.
- Figure 8 Light absorption of $Na_2KSb(Cs)$ as a function of photon energy.⁴³
- Figure 9 Overall view of vacuum system.
- Figure 10 Top view of experimental chamber.
- Figure 11 Sample manipulator assembly.
- Figure 12 Substrate assembly.
- Figure 13 Circuit used for sputter cleaning of substrate.
- Figure 14 Deposition chamber.
- Figure 15 Deposition chamber shown with cover removed.
- Figure 16 Construction of antimony evaporator.
- Figure 17 Construction of alkali channels.
- Figure 18 Vapor pressure curves of sample constituents.⁴⁵
- Figure 19 Light source optics for photoemission measurements.
- Figure 20 Hemispherical grid system for photoemission measurements.
- Figure 21 Circuit used for quantum yield measurements.
- Figure 22 Circuit used for measurement of energy distributions of photoelectrons.
- Figure 23 Circuit used for Auger electron spectroscopy measurements.
- Figure 24 Information regarding principal Auger electron energy peaks found in these studies.

- Figure 25 Crystal lattice structures for Na_3Sb , K_3Sb and Na_2KSb .
- Figure 26B Reflection mode application of photocathode.
- Figure 27 Reflectivity of Ta vs. wavelength of incident light.⁴⁶
- Figure 28 Spectral yield results for samples on differing substrates.
- Figure 29 AES results from glass-Au substrate.
- Figure 30 AES results from sample with peak spectral yield of those deposited on glass-Au substrates.
- Figure 31 AES results from sputter cleaned Ta substrate.
- Figure 32 AES results from sample with peak spectral yield of those deposited on a clean Ta substrate.
- Figure 33 AES results from partially cleaned Ta substrate.
- Figure 34 AES results from sample with peak yield of those deposited on a partially cleaned Ta substrate.
- Figure 35 AES results after depositions on sample with peak spectral yield of those formed on a partially cleaned Ta substrate.
- Figure 36 AES results from contaminated Ta substrate.
- Figure 37 AES results from sample with peak yield of those deposited on a contaminated Ta substrate.
- Figure 38 AES results after heating of sample with peak spectral yield of those deposited on a contaminated Ta substrate.
- Figure 39 AES results from S20(24)-Sb(1).
- Figure 40 AES results from S20(20)-Sb(1).
- Figure 41 AES results from S20(5)-Sb(1).
- Figure 42 Spectral yield curves for K, Na, K_3Sb and Na_2KSb .
- Figure 43 Change in spectral yield with excessive Cs deposition.
- Figure 44 Changes in spectral yield of S20(21) due to Na(1) deposition and subsequent heating.
- Figure 45 Spectral yield results of S20(21)-K(1) and those of K_3Sb reported by Spicer and Jeanes.

- Figure 46 Residual gas analyzer data from K channel operation.
- Figure 47 Contaminant gases output of alkali dispenser channels.
- Figure 48 Map of relative quantum yield of S20(8)-Na(1).
- Figure 49 Summation of AES peak height changes from two locations on S20(25)-Cs(1).
- Figure 50 Schedule of heating temperatures and duration of heating periods for S20(25)-Cs(1).
- Figure 51 Spectral yield results from two locations on S20(25)-Cs(1).
- Figure 52 Summation of AES peak height changes from two locations on S20(25)-K(1).
- Figure 53 Spectral yield results from two locations on S20(25)-K(1).
- Figure 54 Spectral yield results from five locations on S20(24)-K(2).
- Figure 55 Summation of AES results from 5 locations on S20(24)-K(2).
- Figure 56 Changes in AES peaks due to electron bombardment.
- Figure 57A Change in K AES peak under electron bombardment.
- Figure 57B Stability of K AES peak under electron bombardment.
- Figure 58 Spectral yield changes due to electron bombardment of S20(21)-K(2).
- Figure 59 Stability of spectral yield of S20(21)-K(2) under electron bombardment.
- Figure 60 Spectral yield results from single crystal Na₃Sb before and after electron bombardment.
- Figure 61 Map of substrate showing position of electron beam for AES analysis.
- Figure 62 Stability of spectral yield of S20(24)-K(2) under electron bombardment.
- Figure 63 Summation of AES peak height changes due to heating S20(24)-K(2).
- Figure 64 Schedule of heating temperatures and duration of heating periods for S20(24)-K(2).
- Figure 65A Pictorial representation of S20(24) deposition schedule through K(2) deposition.
- Figure 65b Pictorial representation of assumed layering of S20(24)-K(2) before heating.

- Figure 66 Spectral yield of Na_3Sb .
- Figure 67 Summation of AES peak height changes due to Na(1) deposition on and subsequent heating of S20(21).
- Figure 68 AES evidence of the Sb population vs. heating temperature.
- Figure 69 Variation in duration of heating periods.
- Figure 70 Summation of AES peak height changes with heating of S20(24)-Cs(2).
- Figure 71 Schedule of heating temperatures and duration of heating periods for S20(24)-Cs(2).
- Figure 72 Summation of AES peak height changes due to K(1) depositions and heating of S20(25).
- Figure 73 Schedule of depositions, heating temperatures, and duration of heating periods for S20(25)-K(1).
- Figure 74 Summation of AES peak height changes with Na(1) deposition and heating of S20(25).
- Figure 75 Schedule of depositions, heating temperatures, and duration of heating periods for S20(25)-Na(1).
- Figure 76 Summation of AES peak height changes with heating of S20(25)-Cs(2).
- Figure 77 Alkali specie(s) remaining in samples after maximum temperature heating of samples.

Best Available Copy

I. INTRODUCTION

1. History of photocathodes through discovery of $\text{Na}_2\text{KSb}[\text{Cs}]$

From 1887 when H. Hertz¹ made the original discovery of photoemission phenomena they were generally regarded as laboratory curiosities, significant in the understanding of solid state physics, but of little practical value. However, in 1929 L. R. Koller² and N. R. Campbell³ discovered that a combination of silver, cesium, and oxygen had sufficient photoemission for practical applications. After 1929, applications spurred a search for other photocathode materials, but lack of understanding of the photoemission process and of solid state physics, made the search for such materials one of trial and error.⁴

In 1936 Gorlich⁵ found Cs_3Sb to be an excellent photocathode, and this led to subsequent investigation of the photoemission of other alkali antimonide materials. Discovery of the photoemission properties of Na_2KSb occurred accidentally in 1955 when A. Sommer⁶ was investigating the photoemission of Li_2Sb . The Li sources used in that work were contaminated with K and Na which were released from the evaporation source at lower temperatures than was Li. The resulting films were formed of Na, K and Sb, and Li was not a constituent. These Na_2KSb films demonstrated very high quantum efficiency from the near ultra-violet through the near infrared region of the electromagnetic wave spectrum. (Quantum efficiency is defined as electrons emitted/incident photon.)

The discovery of Na_2KSb showed that a bi-alkali antimonide photocathode could have greater photoemission than a mono-alkali antimonide photocathode. Cs was then added to Na_2KSb to determine whether a tri-alkaline antimonide material would be even better.⁷ The addition of Cs extended the useful response of the photocathode to lower photon energies.

From analysis of the photocathode materials found by trial and error, and from a knowledge of semiconductor physics, has come an understanding of factors affecting the spectral yield of a material. Some of these factors are discussed in Section I.2.

2. Factors affecting photoemission from semiconductors

Photoemission is a process in which electrons are ejected from a material due to absorption of incident electromagnetic radiation. For this discussion only those electromagnetic waves with wavelengths from 2200 - 13000 Å, including the near ultra-violet, visible, and near infrared regions of the electromagnetic spectrum and corresponding to photon energies from 5.50 - 0.95 eV will be considered.

Electrons associated with an atom can only occupy fixed energy states, and can absorb energy only in amounts equal to the difference between allowed states. Due to the earlier restriction on photon energies (0.95 - 5.50 eV) only the highest lying electron energy states in semiconductor materials, called the valence band (filled)

and conduction band (unfilled) and separated by a gap of unallowed states, are of interest in this discussion. An energy level diagram for an ideal semiconductor at 0°K is shown in Fig. 1. For the semiconductor represented, photoexcitation, hence optical absorption, could occur only for photon energies, $h\nu > E_G$.

Not all incident light is absorbed by the first monolayer of atoms at the surface of a material. Frohlich and Sack⁸ have presented a theoretical argument that the surface monolayer could absorb no more than 10% of the incident radiation, and experimental evidence indicates the absorption is $< 10\%$.⁹ For this reason photoemission from the bulk is important for high quantum yield.

Following absorption of a photon an electron excited in the bulk may diffuse in the direction of the surface, and energy losses may occur during diffusion. These energy losses are due to collisions with the crystal lattice and/or with other electrons.

The loss per event for electron-lattice collisions is low (0.02 - 0.03 eV), and both Burton¹⁰ studying Cs₃Sb and Dekker¹¹ studying MgO concluded that the average escape depth for photoelectrons was ~ 250 Å when only electron-lattice collisions contributed to energy losses during diffusion.

For electron-electron collisions both collision partners must emerge with sufficient energy to exist in allowed conduction band states. Thus the excited electron must possess energy $> E_V + 2E_G$ for electron-electron collisions to occur. If such collisions are possible the minimum loss per event would be E_G and the mean free path between events is short, 15 - 100 Å.⁹

After diffusion to the surface an excited electron must overcome the surface barrier, called the electron affinity (E_A), in order to escape from the material. The ratio of E_A to E_G for a material can be significant regarding the energy losses suffered during diffusion of an excited electron. Consider the two semiconductors represented by the electron energy band diagrams shown in Fig. 2. The similarities and differences between the two examples shown in Fig. 2 are listed in the table below.

Example I		Example II
$E_A + E_G$	=	$E_A + E_G$
$E_A > E_G$	=	$E_A < E_G$
$h\nu_1$	=	$h\nu_1$

In Example I an electron excited by a photon of energy, $e = h\nu_1$, could collide with another valence band electron providing both collision partners with sufficient energy to be conduction band electrons, but not enough to be emitted as photoelectrons. In Example II electron-electron collisions could not occur for $e = h\nu_1$ because both collision partners could not be raised to

allowed energy states. Photoelectrons in Example I material would be subject to larger energy losses and a shorter mean free path than photoelectrons in an Example II material. Thus higher quantum yield would be expected from materials where $E_A < E_G$.

Consider the two semiconductor materials represented by the electron energy band diagrams shown in Fig. 3. Crystal defects, due either to impurity atoms or lattice imperfections, can result in electron energy states in the forbidden gap creating "p" and "n" type materials with the Fermi level moved in close proximity to the valence band edge or conduction band edge respectively. Surface states at the vacuum interface can create the band bending shown with the Fermi level pinned at the surface. Spicer¹³ has pointed out that "p" type material with a band bending depth, d , much less than the escape depth of the electrons (as shown in Example I of Fig. 3) would create a favorable situation for photoemission. In such a case the effective electron affinity, E_{Aeff} , would be less than the actual electron affinity. This would extend the threshold for photoemission to lower photon energies. In the case of "n" type material band bending would increase the effective electron affinity (as shown in Example II of Fig. 3) and would be detrimental to photoemission. For "p" type material, if the band bending depth was greater than the escape depth of the electrons then the effective electron affinity would equal the actual electron affinity and there would be no enhancement of photoemission due to the band bending.

The intensity, $I(x)$, of light at a distance, x , into a material of uniform absorption is given by the expressions, $I(x) = I_0 e^{-\alpha x}$ (I_0 = intensity incident at the surface, α = absorption constant of the material). For high quantum yield the incident light should be absorbed in a distance comparable to the escape depth of the photoelectrons. An escape depth of 250 Å would require an absorption coefficient of 1×10^6 . In semiconductor materials absorption coefficients of $\sim 1 \times 10^6$ are associated only with interband transitions.⁹ Electron energy states in the forbidden gap due to crystal defects can result in photoemission at a lower threshold than emission from valence band states, but generally the quantum yield of such emission is below the level of practical application.

3. Comparison of $Na_2KSb(Cs)$ with new generation photocathodes

Spectral yield curves for typical $Na_2KSb(Cs)$ photocathodes reported by Sommer in 1968 are shown as Curves A and B of Fig. 4. Note there is a wide variation in response in the threshold region. Control of the photocathode sensitivity in the threshold region is critical for most applications, and is the most difficult problem in commercial production. The spectral yield curve for $Na_2KSb(Cs)$ reported by Spicer¹⁴ in 1958 is shown as Curve C in Fig. 4, and was used as a standard in these studies. The difference between Curve C and Curves A and B probably stems from the steady increase in sensitivity achieved with $Na_2KSb(Cs)$ photocathodes as commercial producers have gained experience with their formation.

In recent years there has evolved a new generation of photocathode materials derived from knowledge of the photoemission process and the electronic structure of semiconductor materials. Prominent in this new generation are the GaAs-Cs-O and Si-Cs-O photocathodes. A comparison is made in Fig. 5 of the spectral yield curves for GaAs-Cs-O reported by Klein¹⁵ (Curve D), Si-Cs-O reported by Martinelli¹⁶ (Curve E), and the typical response curves for Na₂KSb(Cs) (Curves A and B) repeated from Fig. 4. Note the spectral yields from the new generation of photocathodes are superior to those from Na₂KSb(Cs) photocathodes, but the latter remain competitive because the lifetimes¹⁷ of the new generation materials have been significantly shorter and the thermal noise greater.¹⁸

In the literature the terms S-20, tri-alkaline antimonide, multi-alkaline antimonide, and Na₂KSb(Cs) are used interchangeably. Only the last designation will be used in this report.

4. Related research

Technical difficulties have hampered research efforts concerning Na₂KSb(Cs) photocathodes. Both alkali metals and the alkali antimonide compounds are highly reactive with oxygen and water in the air, and alkali antimonide films must be formed and stored under high vacuum conditions. In commercial formation of Na₂KSb(Cs) photocathodes the vacuum tube that will contain the photocathode film is degassed at 300-450°C before the film is deposited. During formation the vacuum tube is heated to 160-220°C, and the very reactive alkali vapors are present in the tube at that time. The chemical activity of the constituents and the need for heating in the processing and formation have hindered or precluded the inclusion of analytical apparatus in a vacuum tube with a Na₂KSb(Cs) film. There also has been a lack of success of formation of high sensitivity photocathodes in anything other than a standard photocathode tube assembly,¹⁸ and such tube assemblies have limited space and accessibility for analytical instruments. The equipment necessary for deposition and analysis of alkali antimonide materials is complex and expensive. As a semiconductor for general use in the electronics field, Na₂KSb(Cs) offers no advantage over other more easily handled materials. With rare exception only users and/or manufacturers of photocathodes have deemed it worthwhile to overcome the technical difficulties listed above and have investigated the properties of Na₂KSb(Cs) and the other alkali antimonide materials.

From previous investigations by others much information concerning Na₂KSb(Cs) has been obtained. Electron energy band diagrams for Na₂KSb and Na₂KSb(Cs) are shown in Fig. 6, with values of E_A and E_G from the reports of Spicer¹⁴ and Jeanes.²⁰ Note that $E_A(0.45 - 0.55) < E_G(1.0)$.

Note also in Fig. 6 that the energy gap for both Na₂KSb and Na₂KSb(Cs) is 1.0 eV. This similarity in E_G supported an early model of the Na₂KSb(Cs) photocathode as a bulk of Na₂KSb and an overlayer of Cs. Experiments by McCarroll²¹ however, have

produced evidence that Cs is present in the bulk, and the exact nature of the role of Cs in the $\text{Na}_2\text{KSb}(\text{Cs})$ photocathode remains a question. In any case, the amount of Cs included in the photocathode is very small.

A diagram of the phases present in the Na_2KSb system reported by McCarroll²² is shown in Fig. 7. The stoichiometry allowing a completely cubic structure is narrowly defined around the Na_2KSb formula. This cubic phase has been identified by McCarroll and Simon²³ as being much more photosensitive than a hexagonal phase with the same constituents. The cubic phase also demonstrates two other characteristics that distinguish it from the hexagonal phases. First, the conductivity of the cubic phase is "p" type due to a stoichiometric excess of Sb. Small additions of Sb increase the conductivity, and small additions of alkali reduce the conductivity.⁶

The conductivity of the hexagonal phase is "n" type.²⁴ Sommer²⁵ reports that in production of Na_2KSb photocathodes there is a reversal of the polarity of conduction from "n" to "p" type at about the moment of maximum photosensitivity. Second, McCarroll²² reports that the cubic phases of all the alkali antimonide materials are more densely packed than the hexagonal phases. Note in Fig. 6 that there is a choice in the energy band diagram for $\text{Na}_2\text{KSb}(\text{Cs})$. Two possibilities are included because it is not possible to experimentally distinguish between real and effective electron affinities. Arguments supporting band bending and a reduction of the effective electron affinity (Fig. 6B) as the source of the photoemission properties of $\text{Na}_2\text{KSb}(\text{Cs})$ are based on the "p" type conductivity of this material and the discussion in Section 1.2. Arguments supporting a reduced real electron affinity as the source of the photoemission properties of $\text{Na}_2\text{KSb}(\text{Cs})$ are based on the observation that for electron emitting semiconductors low electron affinity values are associated only with cubic phase materials. However, there is a reduction of ~ 0.5 eV in the measured value of E_A between Na_2KSb and $\text{Na}_2\text{KSb}(\text{Cs})$, and there is no change in phase. Thus the electron energy band diagram for $\text{Na}_2\text{KSb}(\text{Cs})$ shown in Fig. 6B is more probable.

Also note in Fig. 6 that $E_G + E_A = 1.45 - 1.55$ eV, placing the threshold for photoemission from $\text{Na}_2\text{KSb}(\text{Cs})$ in the near infrared region of the electromagnetic spectrum, a region of interest for many applications.

A possible role for oxygen in the formation of $\text{Na}_2\text{KSb}(\text{Cs})$ photocathodes has been considered. Oxidation of the same alkali antimonide materials (Cs_3Sb^5 , $\text{K}_2\text{CsSb}^{26}$) does increase the red response of these materials. Also there have been reports that oxidation of some $\text{Na}_2\text{KSb}(\text{Cs})$ films has increased their photoemission,²⁷ but in such cases the original response was below average. Sommer²⁸ reports there have been no cases in the literature where superficial oxidation has increased the emission of a $\text{Na}_2\text{KSb}(\text{Cs})$ photocathode with high sensitivity.

A plot of the absorption constant of $\text{Na}_2\text{KSb}(\text{Cs})$ as a function of photon energy is shown in Fig. 8. Note that for $h\nu < 3 \text{ eV}$ the absorption constant is $< 1 \times 10^6$ and, as discussed in Section I.2, this would imply that not all the incident radiation is absorbed within the escape depth of the photoelectrons.

5. Typical formation schedule for $\text{Na}_2\text{KSb}(\text{Cs})$ photocathode

Control of the formation of $\text{Na}_2\text{KSb}(\text{Cs})$ photocathodes in commercial production has been a problem. A common formation schedule reported by Sommer³⁵ is as follows:

"The formation process of Na-K-Sb and Cs-Na-Sb cathodes is much more cumbersome than that of the monoalkali materials. The latter can be made quite simply by introducing a stoichiometric excess of the alkali metal and subsequently removing the excess by baking until peak sensitivity is obtained. No corresponding method is known whereby the ratios of Na to K can be controlled in the same way as the ratio of one alkali metal to antimony. Therefore the following multistep process, or a variation of it, is usually applied.

1. Sb is evaporated, until a light transmission drop to about 70% of the original value indicates that the film has the desired thickness.

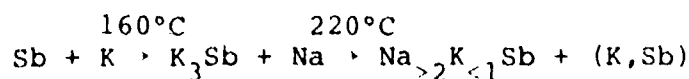
2. A K_3Sb cathode is formed by exposing the Sb film to K vapor at about 160°C .

3. The K_3Sb is exposed to Na vapor at about 220°C . During this step the K in K_3Sb is gradually displaced by Na, but it has so far not been possible to stop this replacement process at the required 2:1 ratio of Na to K. Therefore it is common practice to continue the introduction of Na until a sharp drop in photosensitivity indicates the presence of excess Na. At this stage the compound can be symbolized by the formula $\text{Na}_{>2}\text{K}_{<1}\text{Sb}$.

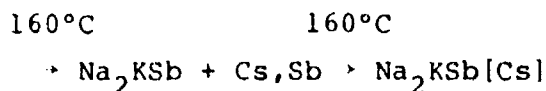
4. To restore the correct Na:K ratio, small amounts of Sb and K are added in alternating steps, at about 160°C , until peak sensitivity is obtained. Depending on the amount of excess Na introduced in step 3, as many as 50 or more Sb-K alternations may be required. This completes the process for the formation of the two-alkali compound Na_2KSb .

5. If the three alkali cathode is to be formed, Sb and Cs have to be added in alternating steps, similar to the K-Sb process of step 4. The Cs-Sb process is also performed at about 160°C , until peak sensitivity is reached.

The whole process can be symbolized by the following diagram:



(1) (2) (3)



(4) (5)

Numerous modifications of these processes exist. To give a few examples, different sequences in the introduction of the alkali metals are possible in which either Na or Cs, rather than K, is introduced first. There is also considerable latitude in the temperature used for the different steps of the process. Further, the thickness of the original Sb film does not appear to be very critical; this point, however, is difficult to check because the thickness of the final cathode film depends not only on the amount of Sb in the first deposit but also on the additions during the alterations with alkali metal. At present there is no convincing evidence that any particular modification produces consistently higher sensitivity."

The alternations in the formation process described by Sommer above are often referred to as "yo-yo" processing. Details of the formation schedules used by the producers of $\text{Na}_2\text{KSb}(\text{Cs})$ photocathodes have been kept secret because the formation process is not under complete control. Commercial processors have advised that their control of the formation process and the photosensitivity of their product have both improved with experience. Production methods that work have been learned through considerable time, experiment, and expense, and such information is considered proprietary as a result.

6. Motivation for these studies

In recent years Auger electron spectroscopy (AES) has provided an analytical technique to determine the atomic species present in the top few atomic layers of a material. AES analysis of $\text{Na}_2\text{KSb}(\text{Cs})$ photocathodes held promise of providing information on such questions as:

- 1) The role of Cs?
- 2) A possible role for oxygen?
- 3) Influence of surface contamination?
- 4) The populations of the constituents in the surface region?
- 5) Chemical changes in the surface region associated with photocathode fatigue?

This laboratory was equipped with the necessary experimental apparatus, and preceding researchers had developed some experience with alkali metals and alkali antimonide compounds. Neither AES nor other similar techniques had been applied previously in investigations of $\text{Na}_2\text{KSb}(\text{Cs})$.

The $\text{Na}_2\text{KSb}(\text{Cs})$ photocathode has been of economic importance since its discovery in 1955, and it is still competitive with new generation photocathode materials. However, the production of $\text{Na}_2\text{KSb}(\text{Cs})$ photocathodes is still done following several different, unsystematic, and sometimes inconsistent schedules because the formation process is only partly understood. Thus in these studies AES was used to study the formation of $\text{Na}_2\text{KSb}(\text{Cs})$ films with the hope of gaining better understanding of the formation process.

II. EXPERIMENTAL APPARATUS AND TECHNIQUES

1. Vacuum system and processing

A twelve inch diameter, stainless steel belljar system by Ultek was used as the experimental chamber. Using a specially made stainless steel collar the chamber was connected to a 300 liter/second sputter ion pump by Consolidated Vacuum Systems. A standard copper gasket ring was used to seal the experimental chamber to the collar, while a 0.020 inch diameter gold wire was crushed between flat flanges to seal the collar to the sputter ion pump chamber. A view of the overall system is shown in Figure 9. Rough pumping of the system from atmospheric pressure to approximately 1×10^{-3} Torr was accomplished with two Zeolite filled sorption pumps chilled to liquid nitrogen temperature. Vacuum conditions during measurements were consistently $<1 \times 10^{-10}$ Torr. Pressure measurements in the vacuum chamber were made with a Bayard - Alpert type ionization gauge, Model No. 715 by General Electric, and a Granville - Phillips Model 20/006 ionization controller. A schematic view of the experimental chamber is shown in Figure 10. The individual pieces of apparatus used for deposition and analysis of the samples are discussed in Section II.2 and through II.5. Processing the ultra high vacuum chamber described above consisted of an initial pumpdown, degassing, and leak checking. The initial pumpdown was continued for 12 - 24 hours and generally resulted in pressures of 3 to 7×10^{-9} Torr. The vacuum system was then degassed via baking at $200 - 250^\circ\text{C}$ for 12 - 48 hours. After cooling the chamber pressure was normally $<1 \times 10^{-10}$ Torr. Regardless of the pressure however, a leak check was made by immersing the entire system in He gas and using an EAI QUAD 150A residual gas analyzer. If no leaks were detected, deposition and analysis of a $\text{Na}_2\text{KSb}(\text{Cs})$ photocathode film was begun.

2. Substrate

a. Manipulator assembly and substrate design

A diagram of the manipulator used to move the sample to the various positions in the experimental chamber is shown in Figure 11.

Only the apparatus shown attached to the vacuum side of the flange feedthroughs was designed and constructed for these studies. The general purpose portion of the manipulator assembly was designed and built by other members of the Physical Electronics Laboratory. It provided 360° of rotation, two tilting planes (approximately orthogonal), and 5 centimeters of vertical motion. These motion capabilities were more than adequate for use in these studies.

The sample films were deposited on a tantalum (Ta) substrate fabricated of 0.010 inch thick sheet as shown in Figure 12. The Ta piece at the end of the manipulator arm was changed for the deposition of each sample in order to eliminate possible contamination by residue left from a previous sample.

b. Positioning procedure

Critical to these studies was the ability to control positioning of the samples relative to the incident electron beam used in AES measurements and the incident light beam used in photoemission measurements. Sample non-uniformities and sample changes due to electron bombardment necessitated this positioning information. The location of the light and electron beams were fixed relative to the experimental chamber. Positioning the sample relative to these fixed beams was accomplished in the following manner. The rotation cylinder of the sample manipulator shown in Figure 11 had a flat top and a degree of rotation indicator. The manipulator assembly was leveled at a fixed rotation position by placing a machinists level on the rotation cylinder and manipulating the two tilting planes. The substrate was located ~5.75 cm from the axis of rotation of the manipulator, and one degree of rotation translated into ~1 mm of horizontal motion of the substrate relative to the fixed electron and light beams. Three sets of threaded rods and threaded sleeves were used to produce vertical motion of the manipulator. The threadpitch of the sleeves and rods translated into ~0.9 mm of vertical motion of the substrate per sleeve rotation. A zero for vertical motion was established relative to the fixed experimental chamber. The accuracy of the positioning system was checked by comparison of the substrate edges as seen by AES and photoemission measurements with the actual dimensions of the substrate, and by repeated measurements. Consistent positioning to within $\frac{1}{2}$ mm was obtained in this manner.

At an early stage of these studies a phosphor target was substituted for the auxiliary target on the sample manipulator. Visual observation of the light beam size and the AES incident electron beam size on the target indicated both were ~1.5 mm in diameter. The size of the light beam on the target was difficult to determine due to its orthogonal position relative to the experimental chamber viewport. Confirmation of the light beam size on the sample was obtained by tests of the optics system made independent of the experimental chamber.

c. Heating and temperature measurement

Sample temperatures were measured using the Pt and Pt + 10% Rh thermocouple spot welded to the back of the substrate as shown in Figures 11 and 12. The substrate was heated by passing current through a tungsten filament which was mounted behind the substrate and also shown in Figures 11 and 12. Before the start of sample deposition a correlation between substrate temperature and heater filament current was established. Subsequently the substrate heater filament current was used as a measure of substrate heating. Consistent temperature readings to within 10°C were obtained in this manner. Additional substrate heating also occurred due to the deposition chamber wall heater when the substrate was in the deposition chamber window, but this additional heating was less than 5°C for the normal deposition times used. The deposition chamber is discussed in Section II.3a.

The substrate and its heater filament were degassed following the vacuum system processing and prior to sample deposition. The degassing process was to heat the substrate at 200°C until the ionization gauge pressure reading went through a maximum and stabilized. This pressure stabilization required <60 minutes and degassing times used were >60 minutes.

d. Sputter cleaning

A sputtering chamber and xenon gas admission system were included in the experimental apparatus for three possible uses: 1) sputter cleaning of the substrate between sample depositions, 2) cleaning of the substrate before sample deposition, and 3) depth profiles of the sample components via AES. All three possible uses were tested and eventually abandoned.

When sputtering was done, the circuit shown in Figure 13 was used.

Sputter cleaning of the substrate between sample depositions to allow multiple samples to be deposited with only one vacuum chamber opening did not prove to be a practical idea. Complete removal of an existing sample required extended sputtering times, and electrical insulators throughout the experimental chamber were repeatedly shorted by sputtered material. Much time was lost to opening the vacuum system and cleaning these insulators. In addition, at the end of most sample depositions one or more constituent sources needed to be replenished, and the vacuum chamber had to be opened for that reason.

Most use of the sputtering capability was for substrate cleaning prior to sample deposition; the effects of substrate cleaning are discussed in Section III.2.

Attempts to obtain depth profiles of the sample components were also unsuccessful for a number of reasons. Sputtering products contaminated the experimental chamber. The relative sputtering

rates of the constituents were not known. The xenon gas pressures ($\sim 1 \times 10^{-3}$ Torr) necessitated long pumpdown periods between sputtering and AES analysis. Some contaminants were introduced to the experimental chamber with the xenon gas.

The sputtering capabilities in the experimental chamber were used only early in these studies.

3. Deposition chamber and constituent sources

a. Deposition chamber

Diagrams of the chamber used for deposition of the constituents are shown in Figures 14 and 15. This deposition chamber was fabricated from 0.020 thick stainless steel sheet, and in such a manner that the top and one side could be removed to allow replacement of the alkali metal dispensers and reloading of the antimony evaporator. When the constituents were deposited the substrate was moved into the deposition chamber window.

b. Antimony source

The antimony source used was a resistively heated Ta evaporator filled with Sb powder. A diagram of the Sb evaporator is shown in Figure 16. It was constructed of 0.0002 inch thick Ta sheet into which cup shaped depressions were formed with a round ended tool. The hole in the top cup was drilled, and the two halves were spot welded together. The top hole in the evaporator and the chute directly above it in the deposition chamber served to channel the Sb vapor to the deposition chamber window. Fisher's²⁹ experience with a similar Ta evaporator in his studies of Na_3Sb showed that such an evaporator would be suitable as an Sb source for these studies.

The powdered Sb was obtained by crushing small crystals of the metal with a mortar and pestle immediately prior to loading the evaporator. The Sb metal was obtained from the J. T. Baker Chemical Company of Phillipsburg, Pennsylvania. Chemical analysis of the Sb by the supplier is shown in Table A.

Table A

Element	
Antimony	100
Iron	0.002
Arsenic	0.004
Lead	0.004
Copper	0.002

These concentrations of the contaminants are below the sensitivity of AES analysis.

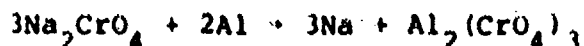
Loading the Sb evaporator was more involved than might appear on the surface. Pouring Sb powder into the evaporator until the cup was full did not provide sufficient Sb for formation of samples of the desired thickness. The procedure used to get enough Sb into the evaporator was to pour it full and then pack the Sb with a wire mounted on a handle. Twenty to thirty pouring and packing operations were required to fill the evaporator.

During the loading of the Sb evaporator the deposition chamber had to remain in approximately the orientation it would have when mounted on the experimental chamber or the Sb powder could spill out. A special stand was built for this purpose because the normal stands for holding the deposition chamber flange would have resulted in positioning orthogonal to the experimental position. Loading the Sb evaporator would have been impossible in such a case.

Immediately prior to the first Sb deposition the evaporator was degassed by passing current below the threshold for Sb evaporation through the evaporator for 60 seconds followed by current at the threshold level for 30 seconds.

c. Alkali metal sources

The alkali metal sources used in this study were dispenser channels manufactured by SAES Getters, Inc. of Milan, Italy. Diagrams of the channel construction are shown in Figure 17. Such channels are the normal means used to introduce the alkali metals in commercial photocathode production, and SAES Getters, Inc. does supply channels to some photocathode producers for this purpose. Detailed information regarding the fabrication of the channels was considered proprietary and was not available from the manufacturer for that reason. The information that was available concerning the channels indicated the alkali metals were probably present in chromate salts. The alkali metal was released as a vapor by reaction of the chromate salt with a reducing agent. Reducing agents used for this purpose include Si, Al, Zr, W, and Fe. The reducing agent used in the SAES channels was probably a combination of 84% Zr and 16% Al. Reactions in the channels for these two reducing agents would be as follows:



The chromate salts and the reducing agents meet a number of requirements mandated by photocathode production. Their reaction temperatures are greater than the maximum temperature (450°C) used to degas vacuum tubes prior to photocathode deposition. They are stable in atmosphere and do not absorb much water vapor. The reaction products, other than the alkali vapors, are minimal. Control of current through the channels controls their temperature

and thereby the reaction rate of the chromate salt and reducing agent.

The alkali channels did not have line-of-sight to the deposition chamber window. In order to move the alkali vapors from the channel space in the deposition chamber to the samples, the walls of the channel space were heated. The heater used was a 0.007 inch diameter, resistively heated tungsten wire shown in Figures 14 and 15. This heater was necessary for successful deposition of all the alkali constituents. If the heater was not used it was not possible to move Na to the samples. K could be moved, but only to a limited extent. Only Cs was easily moved to the samples. The vapor pressure curves of the alkali constituents are shown in Figure 18, and they explain the differences in deposition ease when the heater was not used. When the heater was used it was no problem to move any of the alkali constituents to the samples. The effectiveness of the deposition chamber heater was evidenced by examination of the residue left in the channel space following sample formation. This examination was done while replenishing the constituent sources when the deposition chamber was exposed to the atmosphere. If the deposition chamber heater had been utilized no residue was found on the walls of the channel space. If the heater had not been used a white, crystalline residue was found. Exposure of alkali metals to air results in formation of white compounds such as NaOH, etc. During alkali depositions a current of 2.1 amperes was passed through the deposition chamber heater causing the filament to glow a dull red color.

d. Chamber and source degassing

Before deposition of a sample the deposition chamber was degassed by leaving its heater operating for 20 - 48 hours. Prior to each alkali deposition the heater was turned on for 5 - 10 minutes to allow the chamber walls to heat. After the first alkali deposition on a sample this chamber warmup prior to alkali deposition also served to remove residue from a previous alkali deposition.

Degassing of the alkali channels was done before the first deposition of each alkali. The currents used for the degassing were different for each alkali and are shown in Table B.

Table B

Alkali	Min. and Max. Currents to start reactions	Degassing current 30 seconds	Degassing current 15 seconds
Na	6.5 - 6.8 Amp	6.0 Amp	7.0 Amp
K	4.9 - 5.4 Amp	4.5 Amp	5.5 Amp
Cs	4.3 - 4.4 Amp	4.0 Amp	4.5 Amp

Information on the minimum and maximum currents to start reaction in a channel was obtained from SAES Getters, Inc.

Use of pure alkali metal sources for alkali depositions on the samples was considered but not attempted for a number of reasons. Using the alkali channels paralleled commercial production of $\text{Na}_2\text{KSb}(\text{Cs})$ photocathodes. Pure alkali metals are very reactive chemically in air, and this would have created many handling difficulties. The room temperature vapor pressure of K and Cs would have required cooling of the K and Cs sources and a more complex and expensive experimental apparatus. Pure alkali metal sources were not a proven means to deposit alkali materials at the start of these studies, and when they were tried by others their operation was not entirely successful.

c. Deposition monitoring

Unsuccessful attempts were made to monitor the photoemission of the samples in response to a white light during deposition of the constituents. The white light source was a piece of 0.040 x 0.001 inch tungsten ribbon heated resistively to an incandescent state and located inside the deposition chamber as shown in Figure 14. Photoelectrons emitted by the samples were collected by placing a positive bias on the stainless steel collector plate located ~2 cm from the deposition chamber window. (This was ~2 cm from the sample when the substrate was placed in the deposition chamber window.) A hole in the collector also served as the last of three collimating apertures. Discussion of the failure of this scheme and suggestions for an improved monitoring capability are included in Section III.1.

Photoemission of the samples was monitored by taking spectral yield data or the quantum yield at a single photon energy. Any check of sample photoemission required stopping the deposition then in progress, turning off the deposition chamber heater and moving the sample to the photomeasurements position in the experimental chamber. Monitoring caused the deposition process to be a step by step procedure, and it is possible that peak sample photoemission was elusive because it occurred at the midpoint of a deposition step and thereby went undetected.

4. Photoemission measurements

a. Optics system and calibration

Measurements of photoelectric yield and energy distributions of photoelectrons from the samples were made using the light source and optics system shown in Figure 19 and the three-grid hemispherical analyzer shown in Figure 20. Design of the photoemission measurements system was by D. G. Fisher of this laboratory; some of the details of the system are explained in the following text.

The light source was a 150 watt xenon lamp powered and ignited by a Bausch and Lomb Model No. 33-86-20 power supply. The xenon lamp had reasonably consistent and sufficient intensity over the

photon energy range (1.35-5.50 ev) used in these studies. Downstream from the xenon lamp were two monochromators. Monochromator No. 1 was a Bausch and Lomb Model No. 33-86-25 High Intensity Monochromator which used three different gratings as shown in Table C.

Table C

Photon energy (ev)	Grating (Bausch and Lomb Model No.)	
4.00 - 3.15	UV	33-86-02
3.10 - 1.60	Visible	33-86-01
1.55 - 1.35	IR	33-86-03

Monochromator No. 2 was a Bausch and Lomb Model No. 33-86-40 and used a single, 250 mm grating.

The first monochromator was dominant in the determination of the bandwidth of the light passed by the optics system. The bandwidth of the light passed by this monochromator was dependent upon both the grating and the size of the exit used. Table D shows the bandwidth of the light passed by the system.

Table D

Grating	Grating Bandwidth	Exit slit size	Bandwidth of light passed
UV	3.2mm/mm	0.75 mm	2.4 μ m
Visible	6.4mm/mm	0.75 mm	4.8 μ m
IR	12.8mm/mm	0.75 mm	9.6 μ m

It is not possible to eliminate all stray light with a single monochromator due to reflections from optical surfaces, mountings, walls, etc. Because the two monochromators used here were of considerably different design it is unlikely that any stray light emitted from the first might also pass through the second. The main function of the second monochromator was to insure the spectral purity of the light.

Following the monochromators were filters employed to eliminate higher order harmonics of the frequency selected by the monochromators. Following the filters were plates of quartz set at an angle to reflect a fraction of the light to the active areas of two photocells. The photocells used were a RCA Model No. 917 and a RCA Model No. 935. Two photocells were required because of the range of photon energies used in these studies. The 935 photocell has a high, uniform response in the ultraviolet and visible regions of the spectrum, but its response drops rapidly in infrared

regions where the 917 photocell was employed because of its more uniform response. The response of the photocells was calibrated as a measure of the light incident on the samples. This calibration was done using a thermopile in a position comparable to the sample position and correlating the thermopile response with that of the photocells at 0.05 eV intervals.

Particulars concerning the thermopile were as follows: manufactured by Eppley, Serial No. 4100, special circular type, 16 junction, silver bismuth, and mounted in a vacuum enclosure. The thermopile was calibrated against the radiant flux from Radiation Standard No. C 631 from the National Bureau of Standards. The photocell current was measured both during calibration and spectral yield data collection using a Keithley Model 620 electrometer. The circuit used for making quantum yield measurements is shown in Figure 21. A collector voltage, $V_C = +135$ V, was found to be sufficient to saturate the photocurrent from the samples. A Keithley Model 620 electrometer was used to measure current in the sample lead.

b. Accuracy of quantum yield measurements

Detailed analysis by Fisher²⁹ showed that yield measurement error due to the bandwidth of the light passed by the monochromators was $\pm 1\%$. If stray light was passed by the monochromators then the spectral yield curves could be expected to have a tail in the threshold region. No such tail was found. The accuracy of the sample and photocell current meters was 1% , and could introduce a maximum of 2% error.

The cumulative error in quantum yield measurements introduced by the succession of instruments required to calibrate the optics system is estimated to be $\pm 3\%$.

Probably the greatest single uncertainty in the yield measurements was due to the non-uniformity of the active areas of the 917 and 935 photocells. The arc in the xenon lamp would occasionally change position on the lamp electrodes, and this would cause a slightly different part of the active areas of the photocells to be illuminated. A crude estimate of the non-uniformity in the active area of the photocells would be 10% . When such arc movement occurred the intensity through the optics system sometimes changed markedly. Countering the possible error introduced here was the procedure used in these studies of adjusting the position of the lamp arc at the beginning of each yield data run. This arc alignment was also done at any time the photocell readings indicated a change in lamp arc position. Using this procedure the photocell readings from one yield data run to the next were kept quite uniform, and this implied the same active area of the photocells was being used.

Considering all possible sources of photoelectric yield measurement error the absolute accuracy of such measurements is estimated to be $\sim 10\%$.

c. Energy distribution of photoelectrons

Measurements of energy distributions of photoelectrons were done on only a few samples, and no pertinent data was derived from these measurements. The circuit that was used is shown in Figure 22. As a result of depositions of the sample constituents electrical resistance paths from the sample to ground were sometimes formed and were of the order 1×10^9 to 1×10^{11} ohms. The input resistance of the vibrating reed electrometer, used here in the feedback mode, was $\sim 1 \times 10^{10}$ ohms. When the leakage paths formed it proved to be impossible to obtain energy distribution data from the samples.

5. Auger electron spectroscopy

a. General description of AES

Auger electron spectroscopy (AES) was used to determine the atomic species present in the first few atomic layers of the samples. Details of AES have been discussed by several authors;^{30,31} only a brief description will be included here.

A target material under AES analysis is bombarded with a beam of electrons. If the energy of these incident electrons is sufficient they may ionize a target atom by removing an electron from an inner shell. The target atom then relaxes by transition of an outer shell electron to the inner shell vacancy. Conservation of energy requires the atom emit either an x-ray or an electron as a result of the relaxation process. Electrons emitted in such fashion are called Auger electrons. The electron energy levels of an atomic specie are discrete and unique, so an Auger electron is emitted with an energy identifying the specie of its origin. Energy analysis of electrons emitted by a target material due to interaction with the incident electron beam comprises the second part of AES. In these studies a four grid hemispherical LEED - Auger optics system and the circuit shown in Figure 23 were used for electron energy analysis. Weber and Peria³² have shown the suitability of using such a system.

A retarding potential curve obtained using the grid system shown in Figure 23 is measurement of the electron current from the target to the collector as a function of the potential on the retarding grids, G_2 and G_3 . The number of Auger electrons emitted is small compared to the total emission from a sample. For this reason the second derivative of the retarding potential curve was obtained electronically, as proposed by Harris,³³ to make evidence of Auger electrons more prominent in the data.

Not all atoms have the same probability of emitting an Auger electron due to electron bombardment, and not every electron transition within an atom is equally probable. Identification of atomic species represented by peaks in the AES spectra was aided by charts and example spectra reported by other researchers and equipment manufacturers.

The energy of the incident electrons, 1500 eV, was determined to some extent by limitation of the electron gun power supply, but this energy proved to be sufficient. The parameters of incident beam current, 20 μ A, and modulation amplitude, 10 V peak-to-peak, were selected by trial with the AES system to obtain maximum sensitivity while using minimum incident current.

b. AES spectra particular to these studies

Figure 24 lists the AES peaks found. If more than one AES peak representing an atomic specie was available in the spectra, the largest and most noise free peak was selected to monitor the population of that specie in the first few atomic layers of the target. Note that there are two AES peaks listed for use in monitoring the Cs population. The Cs AES peak doublet appearing at 565 - 575 eV was used for all but the last few samples. At the start of these studies the following arguments were presented against use of the Cs AES peak appearing at 47 eV. Work by others³⁴ of this laboratory indicated all AES peaks at <75 eV were poor monitors for specie population. A large number of true secondary electrons emitted from the samples at <75 eV cause a large and rapidly changing background in the AES spectrum from 0 - 75 eV energy. Also a great many species have AES peaks at <75 eV separated by only a few eV, and resolution is often difficult. For instance, antimony has an AES peak appearing at 50 eV. Later in these studies the large magnitude of the Cs 47 eV AES peak prevailed over the arguments listed above.

If two values are indicated for the electron energy at which an AES peak occurred (Column 2, Figure 24) the peak was a doublet.

Note the letters found in Column 3 of Figure 24. The first of the three letters indicates the atomic shell ionized by the incident electron beam. The second letter identifies the atomic shell from which an electron made the transition to the first shell in order to relax the ionized atom. The third letter indicates the atomic shell from which the Auger electron was emitted.

c. Depth sensitivity of AES and sensitivity of AES to constituents

The escape depth of the Auger electrons is somewhat dependent upon their energy as shown in Column 4 of Figure 24. The escape depths listed are estimates based on a compilation³⁵ of escape depth studies by several researchers. Of special note is the great difference in the escape depths of the Auger electrons (~10 Å) compared to the escape depth of photoelectrons for alkali antimonide materials (250 Å).

During formation of the samples both hexagonal and cubic crystal structures were expected to be present for the various combinations of alkali antimonide compounds that comprised the

films. Representative of these crystal structures are the unit cells for Na_2KSb (cubic) and Na_3Sb , K_3Sb (hexagonal) shown in Figure 25. Comparison of the crystal lattice dimensions shown in Figure 25 with the escape depths of the Auger electrons listed in Column 4 of Figure 24 shows AES analysis was sensitive to species in the first 3 - 4 atomic monolayers. There was no way to distinguish whether a specie was present only in the surface monolayer.

Studies by others³⁶ have determined the sensitivity of AES analysis to the presence of Na, K, and Cs on ordered Ge surfaces; the results of such studies are shown in Table E.

Table E

Alkali specie	Smallest % of mono-layer detected	Substrate
Na	5 - 10%	Ge
K	1%	Ge
Cs	1%	Ge

There can exist some differences in the magnitude of the AES signal from a specie depending upon the presence of other species in the target. These differences in AES signals are believed to be due to differences in electron backscattering of species.³⁷ However, it is not known whether the limit of detectability of a specie would be affected by differences in electron backscattering. In addition no large differences in the electron backscattering of Ge and alkali antimonides are expected. Thus the AES sensitivity to Na, K and Cs in these studies should be similar to that found in the studies of alkali overlayers on Ge substrates. The sensitivity of AES to Sb was estimated by assuming a linear reduction of the Sb AES peak size with reducing Sb population and knowledge of the Sb peak size from clean, pure Sb. Such a calculation would give 2-3% Sb as the threshold amount for AES detection in these studies.

The estimates of AES sensitivity to Na, K, Cs, and Sb were used only to judge the minimum specie population that would be detected. The calibration of AES peak height with species population is discussed in Section III.7b.

6. Schedule of deposition and analysis used in these studies

Before deposition of a sample visual and AES inspections were made of the substrate. Sample formation always began with deposition of Sb while the substrate was at room temperature. This first Sb deposition was then checked visually and via AES for uniformity and possible contamination. K was the next constituent deposited with the substrate normally at room temperature although occasionally it was heated. Collection of spectral yield data began at this stage with visual and AES analysis continuing.

With the K deposition the photoemission of the sample became great enough to allow correlation of the manipulator position with the position of the light beam on the sample. Prior to this point the photoemission of the Ta substrate and of the original Sb deposition were not large enough to permit good resolution of the sample edges as seen by photoemission measurements. Positioning of the AES analysis locations had been done on the substrate earlier, and now a correlation between AES and yield data positions could be made. Several K depositions were usually required at this stage, and the sample was sometimes heated between deposition attempts.

To determine when Na was to be deposited a comparison was made between the spectral yield of the sample and the spectral yield results for K_3Sb reported by Spicer¹⁴ and Jeanes.²⁰ If the sample spectral yield equalled or exceeded that of the standards set then Na deposition was initiated. The Na deposition was also done at either room temperature or at elevated temperatures, and the sample was sometimes heated between deposition attempts. To decide whether the sample was ready for Cs deposition the spectral yield of the sample was compared with the spectral yield of Na_2KSb reported by Spicer.¹⁴

When the spectral yield results were not comparable to the standards set, and especially after all constituents had been deposited, the decision whether or not to heat the sample or which constituents to deposit came from a comparison of the AES results from the sample with those from the most successful sample formed previously. Positive or negative spectral yield changes due to the heating or deposition then determined to what extent the heating or deposition was continued. The spectral yield standards for the final stage of the samples were the spectral yield results for $Na_2KSb(Cs)$ reported by Spicer¹⁴ and the typical S-20 photocathode response curve published by ITT.³⁸ Depositions of the constituents and/or sample heating was continued until the effect of such attempts was either detrimental or had no effect on sample photoemission.

Iterative depositions of the constituents to achieve maximum sensitivity (the "yo-yo" process or alternations discussed in Section 1.5) were generally not successful in increasing sample photoemission. When iterative depositions were attempted they normally resulted in decreasing the photoemission of the samples.

The visual and AES inspections of the first Sb deposition beginning sample formation were not sufficient to determine whether the original Sb deposition was adequate to result in a final film of desired thickness. (As discussed in Section 1.2 a final sample thickness $>250 \text{ \AA}$ was required to achieve maximum quantum yield.) Visual observation was only capable of detecting gross sample changes and the deposition of Sb on Ta was very difficult to detect. AES was inadequate to determine the thickness of the original Sb deposition as the following calculation demonstrates.

The bulk of the sample films consisted of Na_2KSb .

Let: F = atomic weight of Sb/atomic weight of Na_2KSb

$$= 122 / (2 \times 23 + 39 + 122) = 0.59$$

$$v_B = \text{volume of film } 250 \text{ \AA thick} = 1 \times 1 \times 250 \times 10^{-8} \text{ cm}^3$$

$$d_B = \text{density of } \text{Na}_2\text{KSb} = 2.937 \text{ gm/cm}^3$$

$$d_A = \text{density of Sb} = 6.691 \text{ gm/cm}^3$$

t = thickness of original Sb layer for sample 250 \AA thick

$$t = \frac{F \times v_B \times d_B}{d_A} \sim 65 \text{ \AA}$$

Comparison of t above with the escape depth of Auger electrons (Column 4, Figure 24) shows the depth of AES analysis, $\sim 10 \text{ \AA}$, as too shallow to detect sufficient thickness of the original Sb deposition.

To determine whether an original Sb deposition was sufficiently thick a comparison was made between the quantum yield (measured at 4.00 eV photon energy) of the sample and that of K_3Sb , Na_2KSb , and $\text{Na}_2\text{KSb}(\text{Cs})$ reported by Spicer¹⁴ and Jeanes.²⁰ Samples $\sim 250 \text{ \AA}$ thick would be expected to demonstrate lower quantum yield values than those $\sim 250 \text{ \AA}$ thick because of light absorption by the Ta substrate as is discussed in Section II.7. The same Sb evaporator was used for several samples and after the first sample deposition, the time and evaporator current values needed for adequate Sb deposition were established for later samples.

7. Transmission mode and reflection mode utilization of photocathodes

Photocathode films are utilized in either transmission mode, or reflection mode. In transmission mode applications the light is incident through a transparent substrate on one side of the film, and the photoelectrons are emitted on the opposite, vacuum interface as shown in Figure 26A. In reflection mode applications both the incident light and the emitted electron appear at the same vacuum interface as shown in Figure 26B. Most applications of $\text{Na}_2\text{KSb}(\text{Cs})$ photocathodes are transmission mode, but in these studies reflection mode measurements were used because of the need to deposit and analyze the samples at different locations in the experimental chamber.

Transmission mode applications require a compromise between absorption of the incident light and the escape depth of the photoelectrons. If a photocathode film is too thin then the light will pass through it without being absorbed. If the film is too thick then electrons excited near the surface where the light is incident will lose too much energy during diffusion to be able to escape at the vacuum interface. $\text{Na}_2\text{KSb}(\text{Cs})$ photocathode

films of $\sim 100 \text{ \AA}$ thickness have proven to have the highest quantum yield in transmission mode applications.

Reflection mode applications require film thickness $>$ the escape depth of the photoelectrons to result in maximum quantum yield. Consider now the effect of film thickness $< 250 \text{ \AA}$ on reflection mode measurements of quantum yield in these studies. The reflectivity of tantalum vs. wavelength of incident light is shown in Figure 27. Note that at $h\nu = 4.00 \text{ eV}$ the reflectivity of Ta is 20-25%. Thus, 75-80% of the light not absorbed by a film $< 250 \text{ \AA}$ thick would be absorbed by the substrate and would produce negligible photoemission. Therefore one would expect samples $< 250 \text{ \AA}$ on a Ta substrate thick to produce a lower quantum yield at $h\nu = 4.00 \text{ eV}$ than films $> 250 \text{ \AA}$ thick.

Surprisingly theory predicts the quantum yield can be greater in transmission mode for $\text{Na}_2\text{KSb}(\text{Cs})$ films of optimum thickness than for thicker films in reflection mode. Ramberg³⁹ has considered the transmitted and reflected light at the various interfaces of photocathode film, substrate, vacuum and atmosphere in a comparison of transmission mode and reflection mode applications. Due to the interactions of the reflected and transmitted waves he found the optical stimulus in a photocathode film could be greater for optimum thickness films in transmission mode than for thicker films in reflection mode. However, the differences expected by Ramberg's calculations are not large, $< \times 5$. Measurements⁴⁴ done both in reflection and transmission on the same $\text{Na}_2\text{KSb}(\text{Cs})$ films have demonstrated higher quantum yield for transmission mode, but the yield differences were not large, and there was no difference in the threshold region. For these reasons the reflection mode data from these studies is considered applicable to transmission mode films.

III. RESULTS AND DISCUSSION

1. Monitoring sample formation via photoemission

It was originally intended that sample formation would be monitored continuously by measurement of sample photoemission in response to a white light source during deposition of the constituents. The light source for this monitoring was a resistively heated tungsten filament shown in Figure 14 and discussed in Section II.3e. This method of monitoring was not successful, although it appeared promising on occasions. After elimination of several possible reasons for failure of the continuous monitoring system the actual cause of failure was established. The white light source was not enough to ionize alkali vapors released during operation of the constituent sources, and it was also not enough to release electrons. The ions and electrons made meaningful photoemission measurements impossible during operation of the sources regardless of the sample and/or photoelectron collector potentials.

For these studies monitoring of the formation process was intermittent and required moving the samples from the deposition

chamber window to the photoemission measurements grids. This sample repositioning and subsequent data acquisition required 1 - 15 minutes, and the deposition chamber heater had to be turned off during the measurements. Deposition chamber warmup required an additional 5 - 10 minutes before a deposition could be continued.

The ability to monitor the photoemission of the samples during constituent depositions would be desirable, because such monitoring would parallel the commercial processing of $\text{Na}_2\text{KSb}(\text{Cs})$ photocathodes, and optimization of sample photoemission would be greatly simplified and probably enhanced. With major modification of the deposition chamber and mounting flange, sample photoemission could possibly be monitored during depositions of constituents by use of an external, chopped light source and a synchronized detector. A potential problem with an external light source would be depositions on the light entrance window (changing its transmission characteristics). In addition the required modifications of the deposition chamber might result in alkali contamination of the vacuum chamber (causing electrical leakage paths). Following deposition of the alkali constituents leakage paths were sometimes found between the AES analyzer grids. This effect occurred even though the sample filled most of the deposition chamber window which was the only hole in the deposition chamber walls, and the AES grids were located several centimeters from the deposition chamber. Additional holes in the deposition chamber for an external light to fall upon the sample during depositions could result in excessive alkali contamination of the experimental chamber. An optical window in the deposition chamber would pass the needed light and eliminate the extra escape channel for alkali vapors, but such a window would be especially subject to depositions changing its transmission characteristics. In an early model of the deposition chamber an optical window in the deposition chamber was quickly coated with alkali metals. The possibility of low resistance paths appearing as a result of alkali depositions should be considered when choosing and placing the meter used to measure sample photocurrent.

As explained in Section II.3c the deposition chamber was constructed to eliminate line-of-sight between the alkali channels and the sample. Sb depositions required line-of-sight between the S₁ source and the sample, and the Sb evaporator could possibly be a secondary light source leading to confusion in measurement of sample photoemission. In these studies the Sb evaporator was an appreciable light source when operated at maximum current, 20 A, but no significant effect was detected using 15 A current. Use of an external, chopped light source and a synchronized detector would eliminate this potential problem.

2. Substrate effects

The substrate did not appear to be a significant factor in the photoemission from samples in these studies, and AES evidence indicated little, if any contamination of the samples by species from the substrate. Before presentation of the

evidence to support these statements the notation used to distinguish the various stages of formation of the samples will be introduced.

All stages of sample formation due to the operation of a set of alkali channels and a loading of the Sb evaporator are designated by the same prefix, S20(X), where X is the general sample number. The second segment of sample designation is used to indicate the constituent which had been deposited on a particular sample. For example, S20(21)-Na(1) designates the first sodium deposit on sample S20(21). Only a review of the notebooks kept during sample formation and analysis would reveal what events preceded the first sodium deposit on S20(21), but where the history of a sample formation is pertinent to the discussion it will be given in the text. The third segment of sample designation refers to a particular data collecting session called a data point and will often be omitted. The third segment is most often used to distinguish among sample conditions differing only in the degree of heat treatment.

The first few samples were deposited on glass substrates with either gold or aluminum tabs as electrical contacts. Tantalum sheet was the substrate material used for the latter, and more significant samples. When use of the Ta substrates was begun they were sputter cleaned before sample deposition. Due to the problems of sputtering in the experimental chamber discussed in Section II.2e the amount of substrate sputtering was later reduced and finally eliminated. The last few samples were deposited on Ta substrates heavily contaminated by C and O.

A comparison of spectral yield curves from samples deposited on the various substrates is shown in Figure 28. Curves A, B, C, and D are, respectively, the highest spectral yields from samples deposited on:

- A) a glass substrate with Au contacts,
- B) a sputter cleaned Ta substrate,
- C) a partially cleaned Ta substrate, and
- D) a contaminated Ta substrate.

Curve D was the highest spectral yield from any sample in these studies. Most samples had peak spectral yield curves lying between Curves A and B. As will be discussed in the following four paragraphs, AES evidence accompanying Curves A, B, C, and D indicated substrate species were not contaminants of the samples deposited.

Curve A spectral yield data was obtained from S20(2)-Cs(1). An AES spectrum from the substrate before deposition of S20(2) is shown in Figure 29,* and an AES spectrum coincident with

*Note in Figures 29 and 30 the ordinate axis is labelled differently, and the incident electron energy is 2000 eV not 1500 eV, when compared with the bulk of the AES data presented here. These differences from the normal AES data occur because samples S20(1) and S20(2) were deposited in a borrowed system with a cylindrical electron energy analyzer for AES analysis.

Curve A in Figure 30. The strong Au AES peak at 70 eV in Figure 29 is absent in Figure 30 and suggests no Au contamination of the sample. The AES peaks at 40 and 60 eV in Figure 30 may indicate contamination, but they were not identified with any element. The contamination of S20(2)-Cs(1) by O and C could have been the result of diffusion from the substrate. However, both O and C could have been present from other sources, and results discussed below argue against diffusion of O and C from the substrate.

Curve B spectral yield data was obtained from S20(9)-Cs(1). An AES spectrum from the substrate before deposition of S20(9) is shown in Figure 31, and an AES spectrum coincident with Curve B is shown in Figure 32. Comparison of Figures 31 and 32 shows no AES evidence of Ta in the sample. Oxygen and chlorine were present in the sample but were not on the substrate, and this suggests that both arrived by means other than thorough diffusion from the substrate.

Curve C spectral yield data was obtained from S20(20)-Cs(1). An AES spectrum from the substrate before deposition of S20(20) is shown in Figure 33, and an AES spectrum coincident with Curve C is shown in Figure 34. Note in Figure 34 that the AES analysis did not include the energy range 100-200 eV where the largest Ta peaks would appear. The next sweep, shown in Figure 35, which included the 100-200 eV energy range was obtained after continued Cs(1) plus the Na(2), Cs(2), and K(2) depositions on S20(20). Comparing the Sb AES peak height coincident with Curve C and that of Figure 35 shows the latter to be 27% smaller. This implies that the additional alkali depositions could have masked possible sample contamination. Note in Figure 35, however, that there is no AES evidence of Ta contamination of the sample. Oxygen, a prominent contaminant of the substrate, did not appear in the AES evidence from the sample, and this suggests no diffusion of oxygen from the substrate.

As a final example, Curve D spectral yield data was obtained from S20(24)-K(2). An AES spectrum from the substrate before deposition of S20(24) is shown in Figure 36, and an AES spectrum coincident with Curve D is shown in Figure 37. As in the previous example, there was a time interval between Curve D data gathering and a complete AES search (Figure 38) for possible contamination. During this interval only sample heating was done. Comparison of the Sb AES peak height in Figure 37 (before heating) with that of Figure 38 (after heating) shows a 61% increase and suggests no masking of possible contamination by alkali metals. It is doubtful that the Sb AES peak height increase was due to a flood of Sb to the surface (masking evidence of contamination). The heating between collection of AES spectra for Figures 37 and 38 was 175°C for 10 hours and 30 minutes. Note that in Figure 38 there is no evidence of contamination.

Consideration of the spectral yield and AES evidence presented above leads to the conclusions that neither substrate constituents nor contaminants were present near the surface of the samples and that the substrate was not a significant factor in the photo-emission results achieved.

3. Sb depositions

Sb depositions for sample formation involved only minor technical problems and were consistently free of contamination. The greatest technical difficulty encountered was a lack of adequate Sb in some early samples. The Sb evaporator packing procedure described in Section II.3b eliminated this problem. Neither the Sb evaporator current nor the alkali channel degassing schedule appeared to affect the Sb depositions.

Current passed through the Sb evaporator ranged from 15 amperes, the threshold for Sb deposition, to a maximum of 20 amperes. If contamination was present in the Sb depositions it is probable that evidence of same would have been most prominent at either of the extremes of evaporator operation. An AES spectrum from S20(24)-Sb(1), deposited using 15 amperes, is shown in Figure 39. Note in Figure 39 that only AES peaks for Sb appear. An AES spectrum from S20(20)-Sb(1), deposited using 20 amperes, is shown in Figure 40. Again there is no evidence of contamination.

Listed in Table F are the different degassing schedules used before the Sb(1) depositions of three samples.

Table F

Sb evaporator degassing schedules

Sample	Sb evaporator current	Time (minutes, seconds)
S20(5)	7.5 amperes	(2:00)
	10.0 amperes	(178:00)
S20(20)	10.0 amperes	(1:00)
	12.0 amperes	(1:00)
S20(24)	10.0 amperes	(1:00)
	15.0 amperes	(0:30)

For S20(20) the degassing currents used were below the threshold for Sb evaporation. For S20(24) the degassing current for the last 30 seconds was at the Sb deposition threshold. For S20(5) the degassing currents used were below the threshold for Sb evaporation but were maintained for three hours instead of the 2 minutes or less used for S20(20) and S20(24). An AES spectrum from S20(5)-Sb(1) is shown in Figure 41. Note the Auger spectra from S20(20), S20(24), and S20(5) (Figures 39, 40 and 41) are quite similar. The Sb evaporator degassing schedule evolved during the course of these studies from long and complex to short and simple. This simplification took place because the Sb(1) deposition from a succession of samples with simpler degassing schedules

produced the same AES evidence showing no contamination. No depositions were tried without degassing of the Sb evaporator.

The peak pressures during Sb evaporator degassing were $1-3 \times 10^{-8}$ Torr, and pressures during Sb depositions were only slightly higher. For degassing currents below the threshold for Sb evaporation the pressure peak was transient, while during Sb depositions the pressure was sustained.

Most samples were formed with only one Sb deposition. Sb depositions after the first generally caused reductions in the spectral yield.

As noted in Section II.3b, Fe, Ar, Cu, and Pb were listed as very low concentration contaminants of the Sb used. There was no AES evidence in these studies suggesting contamination of the Sb depositions, or any other sample stage, by Fe, Ar, Cu, or Pb.

4. Alkali depositions

Alkali depositions were troublesome for several reasons:

- 1) The alkali channels did not function consistently.
- 2) The success of an alkali deposition was dependent upon many factors.
- 3) The output of an alkali channel was contaminated with other alkali species.

These topics will be discussed more thoroughly below. In these studies the channel current required to obtain a given alkali deposition was found to vary, and the currents used were often greater than those anticipated by information from SAES Getters, Inc. One example of this was the contrast between the Cs(1) depositions of two samples. In both cases the same channel degassing time and current procedure, deposition chamber heater current, and substrate temperature were used. For S20(20)-Cs(1) AES evidence of Cs deposition on the sample was found after only 20 seconds of operation at 5 amperes. For S20(25)-Cs(1) AES evidence of Cs deposition on the sample was not found until after operation at 5 amperes for 45 seconds, plus 6 amperes for 60 seconds, plus 7.5 amperes for 60 seconds. Once deposition had been achieved from a particular channel, later operation of that channel indicated alkali vapors were sometimes released at currents below those expected.

Another example of inconsistent channel functioning was the appearance of shiny, metallic, almost liquid appearing puddles on the surface of four samples as a result of alkali deposition attempts. It is believed that these puddles were the result of excess alkali depositions. The spectral yield of the samples dropped ~ 10 when the puddles appeared. This reduction in photoemission could be explained by comparison of the spectral yield curves of Na and K with those of K_3Sb and Na_2KSb as shown in Figure 42. Note that the spectral yield curves for Na and K

are below the spectral yield curves of K_3Sb and Na_2KSb by at least a factor 10. The reduction in spectral yield due to the Cs(1) deposition on S20(12) is shown in Figure 43. Curve S20(12)-K(3) was the response before the deposition. The reduction in spectral yield due to the Na(1) deposition on S20(21) is shown in Figure 44. Curve S20(21)-K(1) was the sample response before, and Curve S20(21)-Na(1)-5 after, the deposition. Spectral yield data appropriate to this discussion was not available from S20(7)-Na(1) and S20(8)-Cs(1). When the puddles appeared on sample S20(7)-Na(1), S20(8)-Cs(1), and S20(12)-Cs(1) only peaks for Na, K, and Cs were found in the AES spectra. The Sb AES peak had been present before the puddle producing deposition. Sample S20(12)-Cs(1) was left for 21 hours at room temperature. This resulted in disappearance of the puddles, increased sample spectral yield, and a return of the Sb peak in the AES spectra. For S20(21) the Sb AES peak was not eliminated from the spectra by a puddle producing Na(1) deposition, but it was much reduced. Both the AES and spectral yield evidence discussed above supports the interpretation that the appearance of puddles on the sample surface was the result of excessive alkali deposition. These excessive depositions were probably due to a large variation in the rate of reaction in the channels. Identical or almost identical degassing and operation of the channels in some cases produced puddles, and in other cases did not.

Besides proper functioning of the channels the success of alkali depositions depended upon such factors as operation of the deposition chamber heater, the substrate temperature, and the condition of the sample prior to deposition. As discussed in Section II.3c the deposition chamber heater was necessary to effectively move Na and K from the channel space in the deposition chamber to the samples. Early in this study the deposition chamber heater current and the chamber warmup period were fixed. Operation of the deposition chamber heater was not considered a factor in varying alkali deposition success thereafter. Substrate temperatures greater than room temperature could affect the success of an alkali deposition because heating reduced the alkali population of the samples (See Section III.7). Sample conditions could affect the success of alkali depositions because of the ability or inability of one alkali to displace another (See Section III.8).

Another problem with alkali depositions was the presence of more than one alkali in the output of a single channel. Some examples of this cross-contamination are presented below.

Sample formation normally began with the Sb(1) and K(1) depositions; K_3Sb was the anticipated result. Consistently the spectral yield at this stage of sample formation had a significantly lower threshold than the spectral yield results for K_3Sb reported by Spicer¹⁴ and Jeanes.²⁰ An example of such a lower threshold is shown in Figure 45. AES results from the K(1) stage consistently showed the presence of Cs in addition to K and Sb. A test for

contamination of K channel output was done during the formation of S20(21). The sample at the Sb(1) stage was positioned in the deposition chamber window for 20 minutes with the chamber heater operating, but subsequent AES analysis detected no deposition of any alkali on the sample. After operation of the K channel for two minutes AES evidence of both K and Cs was found. No evidence that Na contaminated the output of the K channels was found. In the formation of S20(25), Cs was deposited on the Sb(1) stage, prior to any K or Na depositions. AES spectra from S20(25)-Cs(1) showed peaks for Cs, K and Na. This verified Na and K contamination of the Cs channel output. There was occasional indication that a Na channel output was contaminated by K and/or Cs but this was not verified.

Besides the tests for cross-contamination, other tests were done for possible sample contamination due to alkali depositions. The residual gas analyzer was used to monitor the output of the alkali channels. Mass spectra obtained before and during operation of a K channel are shown in Figure 46. Note that the overall experimental chamber pressure was 1×10^{-10} Torr before operation of the K channel. The K output of the channel was very large relative to the background pressure, and only CO was detected as a significant contaminant. A check of Na channel output produced similar evidence. It was not possible to have the Cs peak (at 133 a.m.u.) and the normal contaminant peaks (at 1 - 50 a.m.u.) appear in the same mass sweep so no comparable data was obtained during operation of a Cs channel. For the residual gas analyzer tests the Na and K channels were operated at 7.5 amperes which was the current normally used for sample formations. Information from SAES Getters, Inc. concerning the gaseous products released during operation of the alkali channels is shown in Figure 47. Note that at 7.5 amperes H_2 and CO are shown as the principal contaminants of channel output. Due to an idiosyncrasy of the residual gas analyzer, including the H_2 peak in the spectra created zeroing problems, and the H_2 peak was not included for that reason. In addition the presence of H cannot be detected via AES analysis, and no conjecture is made as to what role H_2 might play, if any, in the formation of a few $Na_2KSh(Cs)$ photocathodes.

Possible evidence of CO contamination of the samples was tested. A peak for O was occasionally found in the AES spectra. When the O peak was present however, its appearance did not correlate with the use of a channel, nor did its size correlate with the time or intensity of channel operation. A peak for C appeared in the AES spectra only during formation of early samples. Others⁴¹ in this laboratory have investigated CO deposition on sample surfaces. Under electron bombardment the CO dissociated; oxygen left, and carbon remained on the surfaces. From this information one would expect a peak for C to be present in the AES spectra if CO was present. The absence of the C AES peak is interpreted to mean that CO did not contaminate the samples.

Miscellaneous information concerning alkali depositions is included below. Peaks for Zr and Al (the reducing agents in the alkali channels) were sought in the AES spectra but not found. The channel degassing procedure used is listed in Section II.3d, Table B. Many different degassing procedures were recommended, and more complex and longer lasting procedures were used early in these studies. However, no evidence was produced to show that one degassing procedure was better than another so a simple procedure evolved. The vacuum chamber pressure during alkali depositions varied from 1×10^8 to 1×10^7 Torr.

5. Sample uniformity

Sample non-uniformity and the apparent sample changes due to AES analysis (discussed in Section II.6) were the reasons for instituting the sample positioning system described in Section II.2b. Although a significant fraction of a typical sample demonstrated relatively uniform photoemission, the non-uniformities that existed limited the amount of AES analysis that could be done in the early part of these studies.

An example of typical uniformity of sample photoemission is shown in Figure 48. The x's in the figure indicate the location of the center of the light beam used to make photoemission measurements. There was some overlap between the positions as shown by the dotted circle. The numbers above each "x" indicate the yield at that point relative to the maximum yield obtained for this sample at the photon energy employed (3.50 eV). Emission near the bottom edge of the sample was weak because of inadequate Sb deposition.

Commercially produced photocathodes are rated by their response (in microamperes/lumen) to a tungsten lamp of 2870°K color temperature. The photon flux from such a W lamp changes by a factor greater than 100 over the energy range 1.30 - 3.50 eV. The photocathode rating method is an integration over photon energy, of the product of the W lamp output curve times a spectral yield curve. Because of the variation of the W lamp output in the threshold region of the photoemission from $\text{Na}_2\text{KSb}(\text{Cs})$, small difference in spectral yield curves can result in large differences in $\mu\text{A/lumen}$ ratings. Thus even the variations found within the indicated contours of Figure 48 could be significant. For example consider the four spectral yield curves shown in Figure 28. A listing of their $\mu\text{A/lumen}$ response and commercial rating is shown in Table G.

Note in Figure 28 that at photon energy = 3.50 eV, Curves A, C, and D are approximately equal, and recall that all data for Figure 48 was collected at this same photon energy.

The normal procedure used to test sample uniformity was to take quantum yield measurements over the sample (as in Figure 48) using either 3.50 or 4.00 photon energy. Areas were considered equivalent only if their quantum yield values were within 10%. Other procedures used to monitor sample uniformity (use of photon

Table G

Curve (from Fig. 29)	$\mu\text{A/lumen}$	Commercial rating
A	30	Poor
B	<1	Ridiculous
C	85	Good
D	130	Very good

energies <3.50 eV, collection of complete or partial spectral yield curves) did not improve identification of equivalent areas, and took considerably more time.

The incident electron beam used for AES analysis covered an area approximately equal to that shown for the light beam in Figure 48. As will be discussed in Section III.6, it appeared that AES analysis resulted in sample changes, and any area used for AES analysis had to be written off for future sample formation. Correlation of AES spectra and spectral yield results was valid only if the locations measured were equivalent (or the same location). Sample non-uniformity reduced the area where spectral yield data and AES spectra could be correlated. As a result the use of AES analysis was restricted in the early part of these studies.

For the discussion immediately following, and much of the discussion in Sections III.7 and III.8, use is made of a summation format for presentation of the AES results. These summation figures are explained below. Figures 49, 50, and 52 will serve as examples for the text.

- 1) At the end of each curve is the chemical symbol of the element represented, the electron energy of the AES peak used to monitor the population of that specie, and the relative sensitivity of the AES analyzer, (X20 means the analyzer was 20 times more sensitive for measurement of that particular peak than for another labelled X1). The same base sensitivity is common to all AES results in this report.
- 2) Depositions and the time of sample heating periods are listed in some figures at convenient locations among the curves and parallel to the peak height axis. The time of sample heating is given in parentheses in hours and minutes. [Example: 2 hours and 45 minutes = (2:45)]. For other summation results the depositions, heating temperatures, and heating periods are listed in table form in a separate figure.
- 3) Data points, shown along the horizontal axis, represent data collecting sessions. Spectral yield and AES results collected at the same session are given the same data point number.

- 4) The temperatures of sample heating periods are given at convenient locations among the curves and parallel to the data point axis.
- 5) At a convenient point on each curve the error limits of the AES analyzer for that particular peak are shown.

Heating the sample generally resulted in more uniform samples, but, in addition, heating usually reduced the spectral yield. For two sample stages, S20(25)-Cs(1) and K(1), AES spectra and spectral yield data were obtained from two sample locations. These locations were separated by a distance such that there was no overlap in the areas used to make measurements. The AES results in Figures 49, 50 and 52 show uniformity with heating, but the locations were very equivalent at the start. The spectral yield results shown in Figures 51 and 53 were also similar. Note that heating reduced the spectral yield but improved the areal uniformity.

Heating the substrate during deposition of the constituents, as was done for S20(24)-K(2), resulted in even better uniformity. In Figure 54 are shown spectral yield results from five different locations on S20(24)-K(2) at approximately the time of its highest sensitivity. In Figure 55 is shown a summation of the AES results from the same five locations. A map of the data acquisition sites is included in Figure 55.

The problems associated with sample non-uniformity were removed when the effect of AES analysis on the samples was understood and eliminated as explained in Section III.6. Subsequent spectral yield data and AES spectra were collected at the same location on the samples.

6. Effect of AES analysis on samples

Evidence from some early samples indicated AES analysis could result in changes in AES spectra and reduction of spectral yield. However, evidence supporting the idea of such changes was not consistent. Several examples of changes in AES spectra as a result of electron bombardment are presented below.

Figure 56A shows AES peaks for sulfur and chlorine, contaminants of S20(2). The chlorine AES peak was reduced as a result of several minutes of electron bombardment from the size shown in Curve A1 to that shown in Curve A2.

Figure 56B shows the complete disappearance of the K AES peak of S20(5) due to several minutes of exposure to the incident electron beam. Curve B1 was obtained at the start of, and Curve B2 after, the electron bombardment. Carbon was a contaminant of S20(5), and its peak masked the K peak to some extent.

Figure 57A shows an increase in the K AES peak of S20(19)-Cs(1) due to a few minutes of electron bombardment. Curve C1 was obtained from the first sweep of the AES analyzer, Curve C2 from a second sweep a few minutes later, and Curve C3 from a third. Note K peak

increased from C1 to C2, but no change occurred between C2 and C3. Curves C1 and C2 are shown displaced with respect to the electron energy axis and are indicated by dashed lines for that reason.

The changes in AES peaks discussed above imply changes occurred in the populations of species in the surface region of the samples. Electron bombardment could cause dissociation and/or heating, resulting in evaporation of one or more species from the surface. A decrease in the height of a given AES peak could be the result of evaporation from, or diffusion into, the sample by the particular specie. A decrease could also result from diffusion of another specie from the bulk to the surface. The reversal of any of these processes could result in an increase in the size of an AES peak.

Other results indicated that the populations of the sample species were stable under electron bombardment. Figure 57B shows the stability of the K AES peak of S20(19)-Na(2) under electron bombardment. Curve D1 was obtained at the beginning, and Curve D2 after several minutes, of AES analysis. Curve D1 is shown displaced with respect to the electron energy axis, and is indicated by a dashed line for that reason. Note the last two examples, one of change, and the other of stability, were taken from different stages of formation of the same sample.

Typical changes in the spectral yield of a sample due to electron bombardment were 10 - 30%; an example is shown in Figure 58. When spectral yield changes did occur they were almost always in the direction of reduced photoemission from the samples. In contrast, Figure 59 shows the stability of the spectral yield of a sample under electron bombardment. Note that the example of spectral yield change and stability were from the same sample, but at different stages of formation.

Information from other sources was also inconsistent. Concurrent with these studies was a study in this laboratory of single crystals of Na₃Sb, K₃Sb, Cs₃Sb, Rb₃Sb, and Na₂KSb by Dr. M. R. Jeanes.²⁰ Data from the study of single crystal materials gave evidence that electron bombardment was damaging to the spectral yield of all the materials tested. An example of such spectral yield changes is shown in Figure 60. Note the spectral yield of single crystal Na₃Sb was reduced by about a factor 10 as a result of AES analysis. No change in AES spectra from the single crystal Na₃Sb accompanied the spectral yield change, however, AES studies of alkali metal overlayers deposited on Si and Ge single crystals in this laboratory⁴² had not indicated any changes, to either the substrates or the alkali overlayers, occurred during AES analysis.

For at least one early sample deposited on a glass substrate there was visual evidence of sample changes due to electron bombardment. Following AES analysis of S20(5) (276001), a spot the size of the incident electron beam, and in the location of the beam, was noted on a previously uniform sample.

In an attempt to circumvent the problem of apparent sample changes due to electron bombardment the following procedures were initiated:

- (1) The sample positioning system described in Section II.2b was devised.
- (2) Collection of AES spectra was minimized and done only at a few stages of sample formation.
- (3) Photoemission data was collected at several sample locations. AES data was collected at a location equivalent in yield but removed from other locations needed for subsequent sample formation and analysis. (Acquisition of yield data had no measureable effect on the samples.)
- (4) When AES spectra were collected the time of sample exposure to the incident electron beam was minimized. Sweeps of the AES analyzer were made only through restricted electron energy ranges where AES peaks were expected or suspected, and the sweep speed and direction were kept carefully uniform from one data run to the next. Sweep speeds were maximized, with some compromise of AES analyzer resolution as a result.

As stated and shown above there was a inconsistency in the evidence supporting the idea that AES analysis results in sample changes. Some samples appeared to have stable spectral yield and AES results under electron bombardment, but most of the early evidence implied sample changes were occurring. It should be noted that changes in the AES peaks or spectral yield of a sample due to electron bombardment occurred in unison. There was no example of a change in one without a change in the other. However, the changes in AES spectra and spectral yield data were not always proportional.

Investigation of the inconsistency in the data finally led to the conclusion that electron bombardment caused heating of the samples, and this heating did or did not cause the aforementioned changes depending upon sample conditions. Direct proof of the heating effect came from substrate thermocouple readings taken before, during, and after electron bombardment. The electron beam was positioned at several points on the substrate and readings were taken for each beam position. The results are shown in Figure 61 and can be summarized as a 15 - 16°C substrate temperature rise when the beam was positioned on the upper half (where the thermocouple was located), and a 14°C rise when the beam was positioned on the lower half.

The sample with the highest spectral yield in these studies, S20(24)-K(2), was not affected by electron bombardment. The stability of its spectral yield and AES peaks are illustrated in Figures 62 and 37. Note that (Figure 62) the spectral yield curves before and after 15 minutes of electron bombardment are almost identical. In Figure 37 Curves Cs1 and K1 show AES peaks for Cs and K from the first sweep of the AES analyzer. Cs2 and K2 show the same peaks after 12 minutes of electron bombardment.

Comparison of Curves Cs1 and Cs2 or K1 and K2 shows no change. From earlier samples it has been found that the Sb and Na AES peaks were not particularly sensitive to electron bombardment so these peaks were not checked a second time. It should be noted that the substrate was heated during the deposition of this sample. Heating during or following depositions was always found to eliminate subsequent changes due to electron bombardment. Many stages of S20(24) and other samples also displayed the stability illustrated in the examples above.

7. AES results and bulk conditions

a. Information contained in AES results concerning bulk conditions

Although AES analysis was sensitive to only the first few atomic layers of a sample (as explained in Section II.5c), the AES results from the alkali antimonide samples in these studies were sometimes indicative of conditions in the bulk. Part of the evidence relating the AES results with bulk conditions was derived from AES peak changes as a function of heating S20(24)-K(2). Figure 55 shows that the surface region of this sample was quite uniform before heating. On the other hand, Figures 63 and 64 show that heating caused large changes in the K and Cs populations at the particular location sampled. The population changes due heating were much larger than any population differences found among the five locations checked before heating. Note also in Figure 64 that the K AES peak goes through two maxima, and the Cs AES peak through two minima, due to the heating. These phenomena would be difficult to explain by surface diffusion. However, they could be explained by diffusion of waves of alkali metals from layers within the bulk. Of interest in this connection is the deposition schedule for S20(24)-K(2). This schedule was Sb(1), K(1), Sb(2), Na(1), Sb(3), and the K(2). Both the K(1) and K(2) depositions were contaminated with Cs from the K channel. A schematic representation of the deposition schedule is shown in Figure 65A. It will now be argued that the depositions probably resulted in the layered structure shown in Figure 65B. For most of the samples in these studies the Sb(1) and K(1) depositions were made with the substrate at room temperature. As a result of the K(1) depositions the photoemission of the sample changed to a level indicative of K_3Sb , and much greater than would be expected from K alone. This is taken as evidence that K was reacting with Sb at room temperature to form K_3Sb . This reaction occurred within the time (usually less than one minute) necessary to move the samples from the deposition position to the photomeasurements position. From a study of Na_3Sb , Fisher²⁹ reported that the reaction of Na and Sb was complete at room temperature. Thus there is evidence that some alkali-antimony reactions occur* and may be complete, at room temperature. From

* Commercial producers of alkali antimonide photocathodes are often insistent that heating is necessary for alkali antimony reactions because, in commercial production, the alkali metals are only introduced at elevated temperatures. In addition the elevated temperatures are thought to be necessary to speed reactions and to prevent excess alkali metals from shorting electrodes in the tube assembly.

this evidence it is argued that S20(24)-k(2) was a layered structure as shown in Figure 65B. At Data Point 1 of Figure 63, however, Na was present, and this indicates some mixing of the layers. Cesium is shown as free Cs in Figure 65 because it is not known whether it was combined with Sb. Note in Figure 65B that there were two layers containing K and Cs, and diffusion from these layers could account for the double extrema in Figure 63.

Alkali metal diffusing from the bulk to the sample surface would evaporate readily at the elevated temperatures applied to S20(24)-K(2), and the entire vacuum chamber would be a sink for the evaporated material. The mass spectrometer shown in Figure 10 was employed to test for alkali species leaving due to heating, but no evidence of same was found. It is probable that the concentration of alkali atoms leaving the sample was below the sensitivity threshold of the mass spectrometer.

The important conclusion from this discussion is that the changes in the AES peaks of the constituents shown in Figure 63 can be explained by diffusion of alkali from the bulk. This suggests that the alkali/antimony ratio in the bulk was reduced by sample heating.

Note in Figures 63 and 64 the steady increase in the height of the Sb AES peak as a result of heating. This indicates that the alkali/antimony ratio was steadily decreasing in the surface region. The vapor pressure curves for Sb, Na, K, and Cs shown in Figure 18 show that the vapor pressure of Sb is several orders of magnitude below those of the three alkali metals. It is therefore probable that Sb would be stable while the alkali metals were evaporating from the sample.

Thus the evidence from the heating of S20(24)-K(2) shows that the alkali/antimony ratio was decreasing in the surface region of the sample. As was argued above, a similar change was occurring in the bulk. Other evidence relating AES results and bulk conditions is discussed in Section III.7c.

b. Calibration of the Sb AES peak height vs. alkali/antimony ratio

Results from S20(21)-Na(1), and from Na₃Sb reported by Fisher,²⁹ provided a first approximation calibration of the height of the Sb AES peak corresponding to Na₃Sb. Figure 44 shows a comparison of the spectral yield results for Na₃Sb reported by Fisher with those of S20(21)-Na(1). Fisher's control of the stoichiometry of his samples was precise, and in his experiments, depositions of excess Na on Na₃Sb resulted in the appearance of a "knee" in the threshold region of the spectral yield curves (as shown in Curve B of Figure 66). Note in Figure 44 that the spectral yield curves for S20(21)-Na(1)-5,6 demonstrate a similar knee, and that the photoemission in the threshold region was above that reported by Fisher for Na₃Sb. For spectral yield Curve S20(21)-Na(1)-7 however, no knee is present, and the curve lies wholly below Fisher's results for Na₃Sb. It is argued that between

Data Point 6 and Data Point 7, S20(21)-Na(1) passed through the Na_3Sb stoichiometry. It is further argued that the AES results for Data Points 6 and 7 should give the bounds on the Sb peak height for 3Na/Sb . A summation of the AES results from S20(21)-Na(1) is shown in Figure 67. On the same scale for the Sb peak height shown in Figure 67, the height of the Sb peak from S20(21)-Sb(1) (clean Sb) was 118 units. Assume for now that the surface composition [indicated in the AES results from S20(21)-Na(1)] persisted throughout the bulk. Then the AES results at Data Points 6 and 7 (corresponding to the spectral yield arguments of the preceding paragraph) should give the bounds on the Sb peak height corresponding to Na_3Sb . Expressed as a fraction of the clean Sb peak height, these bounds are 26-36%. Arguments supporting the validity of the assumption made here are presented in Section III.7c.

c. The alkali/antimony ratio as a function of heating

Except for the evidence from S20(21)-Na(1) (discussed in Section III.7b) there was no calibration of the height of an AES peak vs. constituent population. For this reason, and because the sensitivities of AES analysis to the three alkali constituents are different (see Section II.5c), the Sb peak was chosen as the monitor for the alkali/antimony ratio.

Plotted in Figure 68 are the Sb AES peak heights (in percent of the clean Sb peak height) for various stages of samples S20(21), S20(24), and S20(25) vs. heating temperature. All values shown in a column above a temperature were obtained at the temperature indicated at the center of the column.

Assume for now two conditions:

- 1) The 3Na/Sb calibration point discussed in Section III.7b is applicable to other samples including K and Cs as well as Na and Sb. The bounds of the calibration are shown by the dotted lines in Figure 68.
- 2) The AES results are indicative of bulk composition.

The validity of these assumptions will be discussed later in this section. Using these assumptions the data in Figure 68 indicates that heating alkali antimonide films (for films that are alkali rich before heating) to temperatures $<200^\circ\text{C}$ leaves them alkali rich, while heating them to temperatures $>200^\circ\text{C}$ produces an antimony rich film. This is an interesting result in the light of normal commercial formation of $\text{Na}_2\text{KSb(Cs)}$ photocathodes.

Recall from the discussion in Sections I.4 and I.5 that:

- 1) The $2\text{Na} + \text{K}_3\text{Sb} \rightarrow 2\text{K}_2 + \text{Na}_2\text{KSb}$ stage of formation would leave an alkali rich material unless there was some mechanism to remove the K displaced by Na.

- 2) The temperature used in the formation step listed in 1) above is 220°C.
- 3) Na₂KSb of high photosensitivity is "p" type due to a stoichiometric excess of Sb, and has a densely packed, cubic crystalline structure.

Sommer⁴⁸ has theorized that the cubic phase alkali antimonide materials are "p" type because there is no room in the closely packed cubic lattice for interstitial alkali atoms. In many private conversations, commercial producers of Na₂KSb(Cs) photocathodes have stated that heating to temperatures of at least 200°C, and preferably 220°C, is essential for production of high sensitivity films. The 200 - 220°C temperatures used may be required to remove excess alkali so that a stoichiometric excess of Sb can be achieved. The removal of excess alkali atoms (potential interstitials) might also facilitate recrystallization to the more closely packed cubic form. The correlation between the data in Figure 68, and the normal temperatures used in commercial formation of Na₂KSb(Cs) photocathodes, supports the validity of the assumption relating AES results and bulk composition.

Included in Figure 68 are results from many sample stages containing K and Cs, and none of the AES spectra from these stages showed a peak for Na as tall as those in the spectra from S20(21)-Na(1) (Figure 67), the source of the 3Na/Sb calibration. No AES spectra, except that from S20(21)-Na(1), contained peaks for only Sb and Na. After heating two sample stages [S20(25)-Cs(1), Figure 49; S20(25)-K(1), Figure 72] there was no Na peak present in the AES spectra at all. If the assumption concerning the more general applicability of the 3Na/Sb calibration was not valid, one might expect a large dispersion of the data points in Figure 68. No serious dispersion is present, however. Thus the grouping of the data in Figure 68 supports the validity of the assumption.

Additional support for the validity of applying the 3Na/Sb³⁶ calibration to samples with K and Cs comes from studies by others of controlled alkali depositions on ordered Ge substrates. Results from these other studies indicate the reduction of the Ge AES peak was similar for the same coverage by Na, K, or Cs, as shown in Table H.

Table H³⁶

Substrate	Alkali	% Monolayer Coverage	% Reduction of Ge AES Peak Height
Ge(111)	Na	100	33 - 38
Ge(100)	K	100	40 - 50
Ge(100)	Cs	85	40

This suggests that the effect on the Sb AES peak height should be similar for equal populations of Na, K, or Cs in the samples in these studies.

The possibility that the duration of the heating periods (in addition to the temperature) might be a factor in the distribution of the data points in Figure 68 was considered. The durations of the heating periods are listed with every figure showing a summation of AES results, and a summary of their variation is shown in Figure 69. As an example, note in Figure 69 that at 175°C, the duration of the heating periods ranged from 10 minutes to over 25 hours. Then note the grouping of the data points at 175°C in Figure 68. Similar checks at other temperatures suggest that the data points of Figure 68 were independent of the duration of the heating periods.

Four data points in Figure 68 (shown as Δ 's) are somewhat divergent from the normal pattern, and all were results from S20(25)-Cs(1). It will be argued below that the AES results (Figure 49) suggest that this sample was already alkali deficient for 100 and 150°C temperatures, and that this would have produced the unusually high data points in Figure 68. Recall from the discussion at the beginning of this section that the Sb AES peak height was chosen to monitor the alkali/antimony ratio in the samples. For every sample, except S20(25)-Cs(1), the first heating of the sample resulted in an increase of the Sb AES peak height. Examples of such increases are listed below in Table I.

Table I

Sample	Figure Number	Data Points
S20(21)-Na(1)	67	4 to 5
S20(24)-K(2)	63	1 to 2
S20(25)-Cs(2)	76	1 to 2

Similar increases in the Sb peak height also occurred in almost every case of the first heating of a sample at a higher temperature. These Sb peak height increases are interpreted as an indication that the samples were alkali rich (at least for the particular temperature) before the heating was begun. However, the results from S20(25)-Cs(1) (Figure 49) show a slight decrease in the Sb peak height with the first heating at Location A, and the first two heatings at Location B. This decrease is interpreted as an indication that this sample was alkali deficient (for 100 and 150°C temperatures) before heating was begun. A diffusion of alkali to the surface, or a redistribution of alkali due to surface diffusion, might be the reason for the Sb peak decrease. The important point to note is that the alkali/antimony ratio did not decrease (compared to the ratio before any heating) with the first two heatings of S20(25)-Cs(1).

The formation of S20(24)-K(2) (the sample stage with the highest spectral yield found in these studies) appeared to contradict the arguments presented at the beginning of this section that a minimum temperature of 200°C is necessary to form a high sensitivity Na₂KSb(Cs) photocathode. Temperatures of <175°C only, were used in its formation. However, the Sb depositions for the formation of this sample stage were much larger than normal, and the sample was probably antimony rich as a result. This suggests that formation of Na₂KSb(Cs) photocathodes would be possible at a temperature of 175°C, and perhaps at lower temperatures, if the formation was approached from an antimony rich standpoint. Approaching the formation in this manner, however, would not be practical for commercial production because of the limited control of the alkali depositions. Attempting to achieve the correct proportions of Na and K in the photocathodes almost inevitably results in excess depositions of alkali metals, and some mechanism (heating) is required to remove this excess.

If Na₂KSb(Cs) photocathodes could be formed at room temperature, some heating might still be necessary to achieve the desired result. McCarroll⁴⁷ reported that Cs₃Sb deposited at room temperature was polycrystalline, and annealing to ~200°C was necessary to produce a cubic crystal lattice with high photosensitivity. If annealing would be necessary for Na₂KSb(Cs), the results from S20(24)-K(2) suggest that a temperature no greater than 175°C would be required.

d. The alkali/antimony ratio of the sample with the highest spectral yield

The discussion in Section III.7c suggests the 3Na/Sb calibration discussed in Section III.7b might be applicable to samples containing K and Cs as well. Therefore this calibration will be applied to the sample with the highest spectral yield found in these studies [S20(24)-K(2), Figure 28, Curve D, 130µA/lumen]. The AES spectrum coincident with the highest spectral yield is shown in Figure 37. The AES spectrum from S20(24)-Sb(1) is shown in Figure 39. The Sb peak in Figure 37 is 17% of the height found in the clean Sb case. The 26-36% calibration for 3 alkali/Sb suggests the sample was alkali rich at the time of its highest yield. However, the high photosensitivity found in this case is normally associated only with "p" type materials that are antimony rich. Thus the reduced Sb peak in Figure 37 is interpreted to be an indication of an alkali overlayer on an antimony-rich bulk. Peaks for Na, K and Cs are all found in Figure 37 so it is not possible to say whether the overlayer contained one or more alkali species.

Many of the data points in Figure 68, at temperatures < 200°C, indicate an alkali/antimony ratio > 3/1. These data points may well reflect bulk conditions, and not just an alkali overlayer. Only in the case of S20(24)-K(2) was the photosensitivity high enough to indicate the presence of antimony-rich (p-type, cubic) conditions in the bulk.

8. The stability of the alkali constituents with the deposition of other alkali species and heating.

As discussed in Section III.7c, the alkali/antimony ratio in the samples was reduced by heating; the higher the temperature, the smaller the total alkali population. In this section it will be argued that the relative populations of the alkali constituents may have been factors in determining which alkali species was removed from the samples because of heating, and which remained. Of course, the relative populations of the alkali constituents changed with alkali depositions.

The AES results obtained after heating the samples in these studies ran counter to expectations based on the breakdown temperatures found for monoalkali antimonide photocathodes. Commercial producers of alkali antimonide photocathodes have found a hierarchy in the breakdown temperatures of their monoalkali antimonide products.¹⁸ The photoemission of Cs_3Sb deteriorates at a lower temperature ($\sim 100^\circ\text{C}$) than the photoemission of K_3Sb ($\sim 200^\circ\text{C}$), and the photoemission of K_3Sb deteriorates at a lower temperature than that of Na_3Sb ($\sim 280\text{--}300^\circ\text{C}$). The breakdown in the photocathodes is assumed to be the result of alkali atoms leaving the films. Because the breakdown temperature hierarchy follows a pattern parallel to that of the differences in the vapor pressures of Na, K, and Cs (Figure 18), it is thought that the two phenomena are related.¹⁸ The breakdown temperature hierarchy hints that, if one were to heat a sample containing Na, K, Cs, and Sb, Cs might leave for temperatures $>100^\circ\text{C}$, K for temperatures $>200^\circ\text{C}$, and Na for temperatures $>300^\circ\text{C}$. This was not found in the results in these studies as is illustrated by the data in Figure 77. Of all the examples in Figure 77 those contrasting most with the expectations from the breakdown temperature hierarchy are the results from S20(25)-Cs(1) and S20(25)-K(1).

In the first case, Cs remained in the sample even after heating at a temperature of 240°C for 37 hours. Both K and Na had been present in this sample at lower temperatures, but both were eliminated by heating to a temperature of only 200°C (Figure 49). The possibility that the presence of oxygen as a contaminant of S20(25)-Cs(1) might explain the post heating existence of Cs was considered, because when Cs is combined with O its vapor pressure is reduced significantly.⁴⁹ However, note in the summation of AES results from S20(25)-Na(1) (Figure 74, Data Point 13) that Cs was eliminated with heating to a temperature of only 175°C , and oxygen was present in that sample also. In addition, note in the summation of AES results from S20(25)-K(1) (Figure 72, Data Points A7 - 4) that there was no apparent correlation between the O and Cs AES peak heights. The information from S20(25)-Na(1) and K(1) (Figure 74 and 72) suggests that the presence of oxygen would not account for the Cs signal remaining in the AES spectra after the 240°C heating of S20(25)-Cs(1) (Figure 49, Data Points A7 and B7).

In the case of S20(25)-K(1) (Figures 72 and 73) heating the sample to 100°C left Cs and K remaining in the sample, but not Na, which had been present earlier. The evidence from this sample

is not as definite as that from the example discussed in the preceding paragraph because the many K depositions on S20(25)-K(1) reduced the height of the Sb AES peak enough to allow for the possibility of an overlayer screening Na that might have been in the sample bulk.

Reviewing the examples in Figure 77 it should be noted that all results [except those from S20(21)-Na(1)] contradict the idea that only Na would remain in samples heated to temperatures $>200^{\circ}\text{C}$ for a long duration.

The contradictions between the breakdown temperature hierarchy and the results from the present studies might possibly be related to the mechanism creating high sensitivity in the monoalkali antimonide photocathodes. Support for this idea is presented in the following two paragraphs.

To determine the breakdown temperatures of the monoalkali antimonide photocathodes, changes in the response of high photosensitivity films are monitored. The high photosensitivity of the commercial samples might be associated with the existence of an alkali overlayer on a bulk alkali antimonide. Certainly this could be true of Na on Na_3Sb and K on K_3Sb . Fisher²⁹ has reported that excess of Na deposited on Na_3Sb brought enhancement of the spectral yield of his samples. Similar results for K on K_3Sb have been reported by Spicer.¹⁴ The case of Cs on Cs_3Sb will be discussed later. Now it would probably require less energy to remove an alkali atom from an overlayer than from the sample bulk. Alkali atoms that might leave an overlayer at one temperature might not leave the sample bulk until they are subjected to much higher temperatures. A difference in temperatures for removal of alkali atoms from an overlayer and the sample bulk would reconcile the data in Figure 77 (species remaining at unexpectedly high temperatures) with the breakdown temperature hierarchy.

The case of Cs_3Sb is considerably different from those of Na_3Sb and K_3Sb . Cs_3Sb is a "p" type, cubic-phase material, whereas Na_3Sb and K_3Sb are "n" type and hexagonal. Peak photosensitivity of Cs_3Sb is reached for a stoichiometric excess of Sb. Thus the arguments presented in the preceding paragraph concerning an alkali overlayer on an alkali antimonide bulk would hold for Cs_3Sb only if it were possible to have a Cs overlayer on a Cs_3Sb bulk that is deficient in Cs. It will now be argued that just such a situation can exist.

Support for the idea can be derived from the summation of AES results for S20(25)-Cs(1) shown in Figure 49. It has already been argued in Section III.7c that this sample was alkali deficient before heating was begun. Recall from the discussion in Section II.5c (and Figure 24) that the escape depths of the Auger electrons from Cs at 47 and 565 eV were $\sim 5 \text{ \AA}$ and $\sim 10 \text{ \AA}$ respectively. The shorter escape depth of the 47 eV electrons should make the corresponding peak height more sensitive to the Cs population in

the first monolayer of the sample. Now consider the changes in the heights of the AES peaks at the different energies in Figure 49. Note that from Data Points A1 - A4 and B1 - B4 the height of the 47 eV peak goes through greater reductions than does the 565 eV peak. This is interpreted to indicate the Cs population at the sample surface was decreasing more rapidly than the Cs population in the bulk as suggested above. The sample heating temperatures indicated in Figure 49 show that the larger reduction in the surface population of Cs occurred for heating in the 100-200°C range. Once the height of the 47 eV peak stabilized (Data Points A4 - A7 and B4 - B7) heating to 240°C caused no large additional change. Thus the evidence in Figure 49 can be interpreted to suggest the idea that there was an overlayer of Cs on a Cs deficient Cs₃Sb sample. Further, the Cs in the overlayer was removed at temperatures that did not affect the bulk Cs to any large extent.

Somewhat aside from the theme of this section, the results concerning the AES evidence for an overlayer on S20(25)-Cs(1) will be applied to the AES results from the sample with the highest spectral yield in these studies [S20(24)-K(2), Figure 37]. To do this, an assumption will be made that there was no overlayer present at Data Points A4 - A7 and B4 - B7 of Figure 49. This assumption is plausible because at these data points there are no relative changes of the Cs AES peaks at 47 and 565 eV. Next the average value of the ratio of the height of the 47 eV peak to that of the 565 eV peak (47 eV/565 eV ratio) at Data Points A4 - A7 and B4 - B7 was found to be .2. At Data Points A1 - A4 and B1 - B4 the 47eV/565eV ratio is .2 and this will be interpreted to show that a Cs overlayer exists. Now this criterion will be applied to the Cs peaks in Figure 37. Note first that the AES analyzer sensitivity for the Cs AES peaks in both Figure 37 and Figure 49 is the same. In Figure 37 the 47eV/565eV ratio is 4, and this suggests an overlayer did exist on the sample with the maximum spectral yield found in these studies. In addition it can be said that Cs was a part of the overlayer. This evidence, however, does not exclude the possibility that Na and/or K were also part of the overlayer.

Now the discussion will return to the main theme of this section. The evidence that a Cs overlayer can exist on a Cs deficient Cs₃Sb bulk allows the arguments applied earlier to Na₃Sb and K₃Sb to be applied also to Cs₃Sb. These arguments are that the photoresponse of the alkali antimonide photocathodes is associated with an alkali overlayer on a M₃/Sb bulk. The atoms in the overlayer will leave at a lower temperature than the same specie in the bulk. Thus the apparent conflicts between the breakdown temperature hierarchy and the results from these studies can be reconciled. All this argument goes back to the discussion of the data in Figure 77 showing that temperature alone would not determine which alkali specie would leave a sample if it was heated. In the following paragraphs, examples and arguments will be presented to support the idea that the relative populations of the alkali species may be factors in determining which specie will leave as a result of sample heating. The examples will be presented first.

The summation of AES results from S20(21)-Na(1) (Figure 67) indicate that excessive deposition of Na and subsequent heating of a sample originally consisting of K, Cs, and Sb could result in displacement of both K and Cs from the sample. The Na(1) deposition was excessive because puddles (as discussed in Section III.4) appeared on the sample surface. Note in Figure 67 that the AES results were collected in two locations, but that is not considered critical to this discussion. The centers of the two data collection locations were 2 mm apart, and the 1.5 mm diameter of the electron beam caused a large overlap in the effective size of the two locations. In addition, a comparison of Data Points 2 and 3 shows little change in the AES peak heights accompanied the change in measurement location. After the second sample heating, (Data Point 6), the Sb peak was larger than before the Na deposition, thus eliminating the possibility that a Na overlayer masked K and Cs that might have been in the sample. Furthermore, there was a K AES peak in the spectra at Data Point 2, after the deposition. Also note in Figure 67 that from Data Point 6 through 10 only peaks for Na and Sb were in the AES spectra. Both AES results and spectral yield data indicated K and Cs were present before, at the S20(21)-K(3) stage, so their disappearance could not be due to diffusion into the bulk. Thus the AES results from S20(21)-Na(1) suggest that K and Cs were removed from this sample by a combination of heating and an excess of Na. A review of the data in Figure 77 will show several samples [S20(24)-K(2), S20(24)-Cs(2), S20(25)-Na(1), and S20(25)-Cs(2)] that contained Na at the end of heating, but only in the case of S20(21)-Na(1) was there apparently enough Na to eliminate all the K and Cs. This idea is supported by noting that the Na AES peak was larger in the spectra from S20(21)-Na(1) than in the spectra from any other sample.

From another example, S20(25)-Cs(1), Figure 49, came results that suggested both K and Na could be eliminated from a sample by a combination of heating and a large initial Cs population. Both these first two examples suggest that an excess of one alkali specie might result in the elimination of the other two.

In other cases, especially S20(24)-K(2) (Figure 63), the AES results suggested there was a limit to the ability of K and Cs to displace each other. Note in Figure 63 that the Cs and K AES peaks fluctuate through multiple extrema as a result of heating. The Na AES peak height was quite stable so only the K - Cs dynamics will be considered. If K could always displace Cs, or vice versa, then the AES peak of the dominant species would have grown at the expense of the other as waves of Cs and K moved from the bulk of this sample as discussed in Section III.7a. However, because AES peaks for both K and Cs are left at the end of the sample heating there must have been some limit to the ability of each to displace the other.

The unique flexibility in the formation of K_2CsSb photocathodes correlates with the idea of a limited K-Cs displacement. These

photocathodes can be formed by reacting either K with Cs_3Sb , or Cs with K_3Sb . The result in both cases is K_2CsSb which is a preferred stoichiometry for a combination of K, Cs, and Sb.

Another result relating alkali specie populations before heating with the specie remaining after heating comes from a review of all the AES results from the samples listed in Figure 77. Such a review shows no case where peaks for only Na, Cs, and Sb were found in the AES spectra. In every case that both Na and Cs were present in a sample, K was also present. Similar evidence has been obtained from studies of alkali antimonide compounds¹⁸ where stable compounds such as Na_2KSb and K_2CsSb have been identified, but no stable compound such as Na_2CsSb or Cs_2NaSb .

The examples presented above do suggest that the relative populations of the alkali constituents can be factors in determining which specie leaves if a sample is heated. Now a few remarks will be made about the physics that might be involved.

A specie, or species, might be subject to evaporation from a sample because it is excluded from the bulk crystal lattice which, in turn, is determined by the relative populations of the alkali constituents. Recall from the discussion in Section I.5, (and Figure 7), that the crystal phase of the $\text{Na}_{3-x}\text{K}_x\text{Sb}$ system is subject to change from hexagonal to cubic form depending upon the Na/K ratio that is present. Others have also considered a possible relationship between alkali population and crystal structure. For instance, McCarroll⁵⁰ has theorized that the lack of a stable compound combining Na, Cs and Sb is due to the large difference in the sizes of the Na and Cs atoms. The size difference is thought to put excessive demands on the bonds available in alkali antimonide compounds.

Sommer¹⁸ has theorized that the limited K - Cs displacement in the formation of K_2CsSb photocathode is related to the crystal structure of that material. K_2CsSb demonstrates very high resistivity if precise stoichiometry is obtained, and high resistivity in semiconductor materials is generally thought to be a reflection of a lack of defects in the crystal structure. Unfortunately, no information concerning the crystal structures of the samples was available in these studies.

IV. CONCLUSIONS AND SUGGESTIONS FOR CONTINUED INVESTIGATIONS

At the beginning of these studies it was speculated that application of Auger electron spectroscopy might provide information concerning the formation of $\text{Na}_2\text{KSb}(\text{Cs})$ photocathodes. It is the opinion of this researcher that some new insight was achieved, and comments about the results from these studies, and about the example questions posed in Section I.6, are included in the following paragraphs.

1) (See Section III.2) The substrate material* might not be a significant factor in the control of $\text{Na}_2\text{KSb}(\text{Cs})$ photocathode formation. Although commercial production does not use Ta substrates (as used in these studies), the lack of sample contamination by carbon and oxygen (contaminants of the Ta substrates) may have implication for commercial producers. Carbon and oxygen are highly probable contaminants of many substrate materials.

2) (See Section I.6) Comments regarding a possible role for oxygen in the formation of $\text{Na}_2\text{KSb}(\text{Cs})$ photocathodes can only be made in a negative sense. In the AES spectrum from the sample with the highest spectral yield found in these studies [S20(24)-K(2), Figure 37], there was no peak for oxygen. One can say that oxygen is not required to achieve high photosensitivity.

3) (See Section I.6) Remarks regarding surface contamination must also be made in a negative sense. Very little contamination of the samples (occasionally oxygen) was encountered. No evidence of contamination was found in the case of the highest spectral yield.

4) (See Section I.6) There was no exploration of the question regarding photocathode fatigue.

5) (See Sections III.7 and III.6) Although AES is normally only associated with identification of species on the surface region of a sample it might also provide information concerning bulk composition as was the case in these studies. AES can be used to study alkali antimonide materials, but care must be taken to see that the samples are not changing as a result of the analysis technique.

6) (See Section III.7c) The need for heating the samples to at least 200°C at the $2\text{Na} + \text{K}_3\text{Sb} + 2\text{K} + \text{Na}_2\text{KSb}$ stage of formation appears to be related to the need to produce an antimony rich sample, which is related to a cubic crystal structure, "p" type conductivity and high photosensitivity. High sensitivity can also be achieved with heating to 175°C (and perhaps $<175^\circ\text{C}$) if excess Sb is deposited during formation.

7) (See Section III.8) It is possible that the problems with control of the threshold region response of $\text{Na}_2\text{KSb}(\text{Cs})$ photocathodes are associated with the existence of an alkali overlayer. The results of these studies support the idea that there is an alkali overlayer on samples with high photosensitivity. The number, and perhaps specie, of overlayer atoms might be

*The assumptions are made that the substrate material does not react with the photocathode constituents, and is cleaned for used in an ultra high vacuum environment.

subject to sample temperature and crystal structure. (The crystal lattice can affect the binding sites of the overlayer atoms.)

8) (See Sections III.8 and III.4) The success of an attempt to deposit an alkali specie on a multialkali sample (especially if the substrate is heated) would probably be affected by the same factors that determined which alkali specie left a sample when it was heated (the temperature and the relative populations of the alkali constituents). This might explain some of the inconsistencies found in commercial production. The same deposition procedure may be successful or unsuccessful depending on the consistency of the output of the alkali source, and perhaps the success (or lack of success) of previous alkali deposition attempts. This entire matter could be even more confused if the alkali source outputs are cross-contaminated with other alkali species as was found to be the case in these studies.

9) One important conclusion is general and could easily be overlooked. That conclusion is that $\text{Na}_2\text{KSb}(\text{Cs})$ photocathodes of high sensitivity can be successfully deposited in a large ultra high vacuum chamber as used here. This had not been achieved previous to these studies. A large experimental chamber allows for the use of many analytical instruments for the study of the films. These remarks lead quite naturally to suggestions for continued investigations. If studies of $\text{Na}_2\text{KSb}(\text{Cs})$ photocathodes are continued, analytical tools other than AES should be considered. Compared with AES, improved sensitivity to the chemical composition of only the first atomic monolayer could be achieved (ISS), or information regarding the chemical bonding in the samples could be obtained (ESCA). In short, other analytical tools could provide much new information that might be of value in understanding the $\text{Na}_2\text{KSb}(\text{Cs})$ formation process. The present approach using AES could certainly be continued. In this area a calibration of the AES peak heights for Sb and K or Cs for K_3Sb and Cs_3Sb (similar to the $3\text{Na}/\text{Sb}$ calibration discussed in Section III.7b) would be of value in analyzing the AES results from the multialkali samples. More analysis using the relative changes in the Cs AES peaks at 47 and 565 eV could be used to see if Cs is the most significant (or only) constituent of the alkali overlayer on $\text{Na}_2\text{KSb}(\text{Cs})$ photocathodes of ever higher photosensitivity. Of course samples with a range of high sensitivities would be required for this, and that brings up the final remark regarding further investigations. No matter which method of sample analysis is chosen, a modification of the sample formation apparatus should be done to allow for continuous monitoring of sample photoemission during constituent depositions (as discussed in Section III.1). The present deposition and monitoring scheme is too cumbersome, and the success of sample formation too subject to chance.

REFERENCES

1. Hertz, H., Ann. Physik, 31, 983 (1887).
2. Koller, L. R., Phys. Rev., 36, 1639 (1930).
3. Campbell, N. R., Phil. Mag., 12, 173 (1931).
4. Sommer, A. H., Photoemissive Materials, John Wiley and Sons, Inc., New York, (1968) p. 3.
5. Gorlich, P., Z. Physik, 101, 335 (1936).
6. Sommer, A. H., J. Appl. Phys., 29, 1568 (1958).
7. Sommer, A. H., Rev. Sci. Instr., 26, 725 (1955).
8. Frohlich, H. and R. A. Sack, Proc. Phys. Soc. (London), 59, 30 (1947).
9. Sommer, A. H. and W. E. Spicer, Photoelectronic Materials and Devices, edited by S. Larach, D. van Nostrand Co., Inc., Princeton, N. J. (1965) Chapter 4.
10. Burton, J. A., Phys. Rev., 72, 531(A) (1947).
11. Dekker, A. J., Solid State Physics, Vol. 6, edited by F. Seitz and D. Turnbull, Academic Press, Inc., New York (1958) p. 251.
12. Spicer, W. E., RCA Rev., 19, 555 (1958).
13. Sommer, A. H., Photoemissive Materials, p. 119.
14. Spicer, W. E., Phys. Rev., 112, 114 (1958).
15. Klein, W., J. Appl. Phys., 40, 4384 (1969).
16. Martinelli, R. U., Appl., Phys. Letters, 16, 261 (1970).
17. Fisher, D. G., private communication.
18. Sommer, A. H., private communication.
19. Spicer, W. E., Phys. Rev., 112.
20. Jeanes, M. R., Photoelectric Study of the Alkali Antimonides, Physical Electronics Laboratory, Elec. Engr. Dept., Univ. of Minn., Final Report, Sept. 16, 1970 to Sept. 16, 1971, Contract No. 606177 to Bell Tel. Labs., Whippany, N. J.
21. McCarroll, W. H., R. J. Paff, and A. H. Sommer, J. Appl. Phys., 42, 569 (1971).
22. McCarroll, W. H., J. Phys. Chem. Solids, 16, 30 (1960).

23. McCarroll, W. H. and R. E. Simon, Rev. Sci. Instr., 35, 508 (1964).
24. Sommer, A. H., Photoemissive Materials, p. 131.
25. Sommer, A. H., Photoemissive Materials, p. 121.
26. Sommer, A. H., Photoemissive Materials, p. 125.
27. Guselnikov, V. S., and A. N. Khokhlova, Bull. Acad. Sci. U.S.S.R., 26, 1406 (1962).
28. Sommer, A. H., Photoemissive Materials, p. 115.
29. Fisher, D. G., Ph.D. Thesis, University of Minnesota (1968).
30. Lander, J. J., Phys. Rev., 91, 1382 (1953).
31. Chang, C. C., Characterization of Solid Surfaces, edited by P. F. Kane and G. B. Larrabee, Plenum Press, New York (1974) Chapter 20.
32. Weber, R. E. and W. T. Peria, J. Appl. Phys., 38, 4355 (1967).
33. Harris, L. A., J. Appl. Phys., 39, 1419 (1968a).
34. Oswald, R. C. and R. E. Weber, Auger Spectra of the Elementary Constituents of the III-V and II-VI Compounds, Technical Report AFAL-TR-70-12, Contract No. F33615-69-C-1053, February 1970.
35. Palmberg, P. W., Anal. Chem., 45, 549A (1973).
36. Ericson, R. E., Univ. of Minn., private communication.
37. Tarng, M. L., and G. K. Wehner, J. App. Phys., 44, 1534 (1973).
38. Typical Absolute Spectral Response Characteristics of Photoemissive Devices, ITT Industrial Laboratories, 3700 East Pontiac Street, Fort Wayne, Ind.
39. Ramberg, E. G., Appl. Optics, 6, 2163 (1967).
40. Dickey, J., Phys. Rev., 81, 612 (1951).
41. Coburn, J. W., Surface Science, 11, 61 (1968).
42. Weber, R. E. and A. L. Johnson, J. Appl. Phys., 40, 314 (1969).
43. Kondrashov, V. E., and A. S. Shefov, Bull. Acad. Sci. U.S.S.R. Phys. Ser., 28, 1349 (1964).
44. Chabrier, B., P. Dolizy, G. Eschard, J. P. Goudonnet, and J. Vernier, Acta Electronica (Paris), 16, 203 (1973).

45. Honig, R. E., Vapor Pressure Curves for the More Common Elements, RCA Laboratories, Princeton, N. J.
46. Handbook of the Physichemical Properties of the Elements, edited by G. V. Samsonov, IFI/Plenum, New York, (1968) p. 385.
47. McCarroll, W. H., J. Appl. Phys., 32, 2051 (1961).
48. Sommer, A. H., Photoemissive Materials, p. 123.
49. Martinelli, R. U., unpublished results.
50. McCarroll, W. H., private communication.

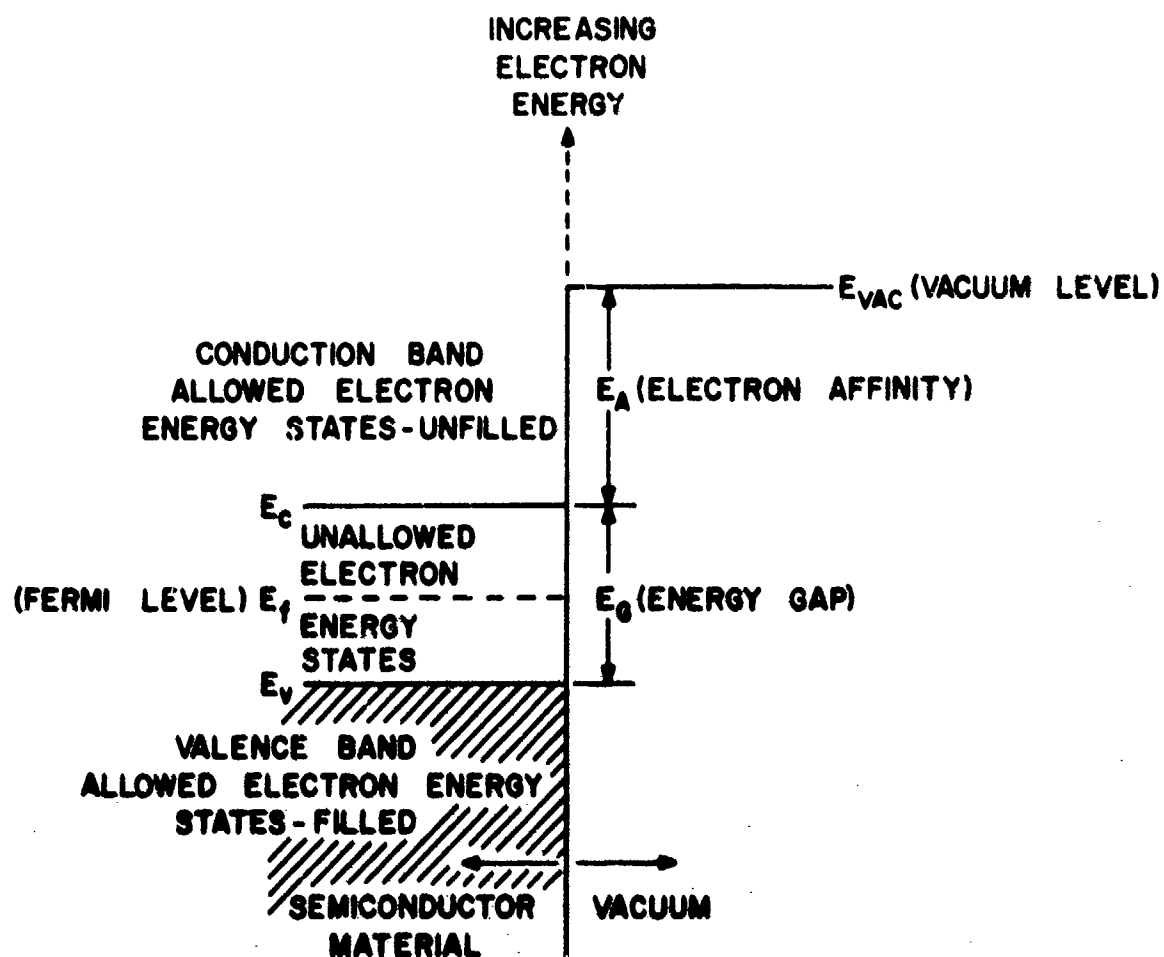


Figure 1 Energy band diagram for an ideal semiconductor at 0°K.

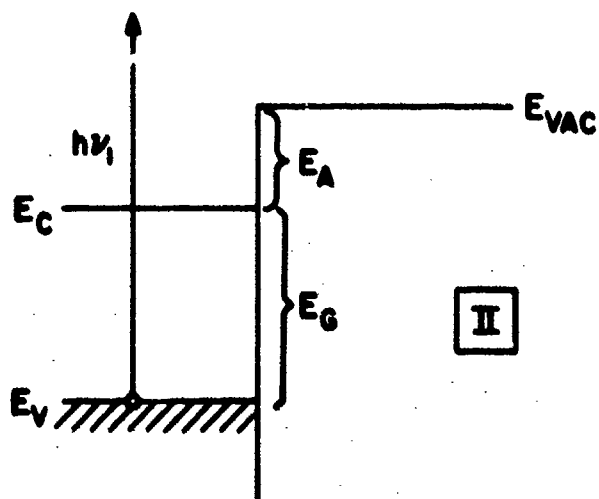
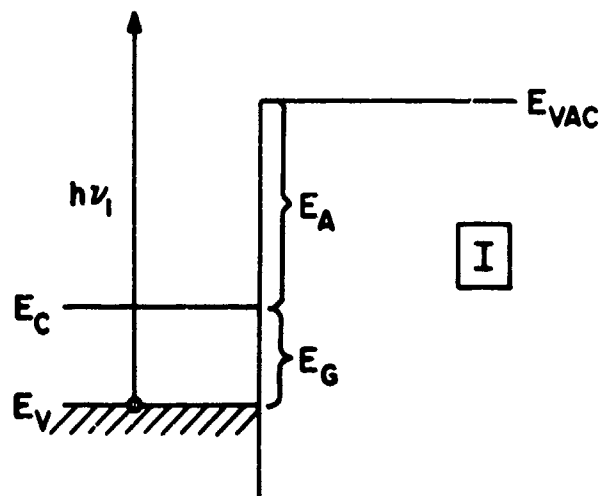


Figure 2 Energy band diagrams for two semiconductor materials with differing E_A/E_G ratios.

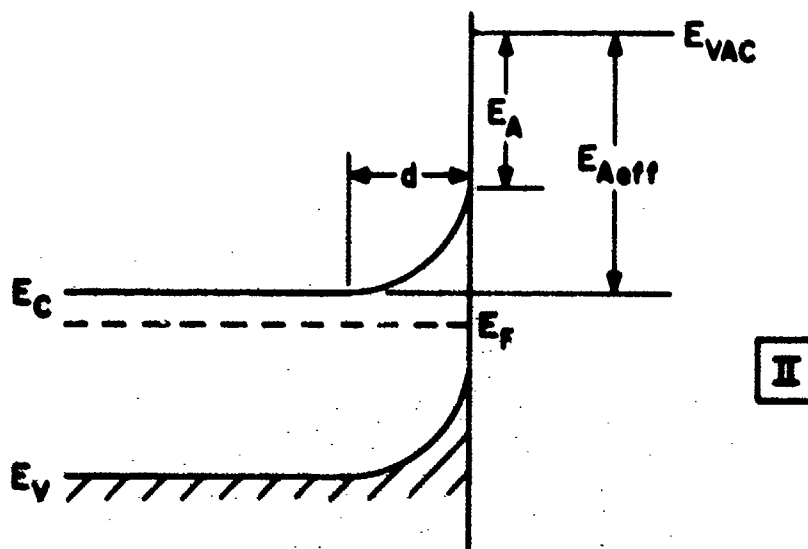
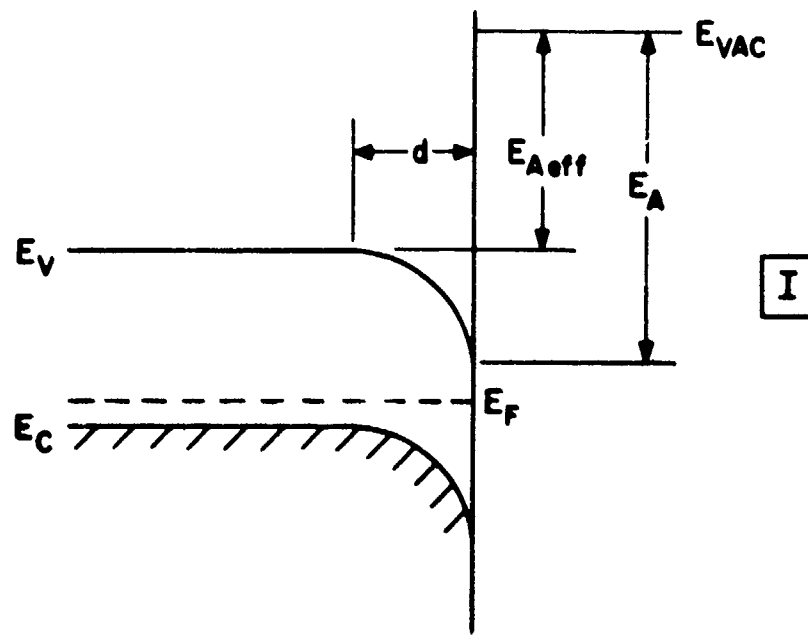


Figure 3 Energy band diagrams showing result of band bending on E_{Aeff} for "n" and "p" type semiconductor materials.

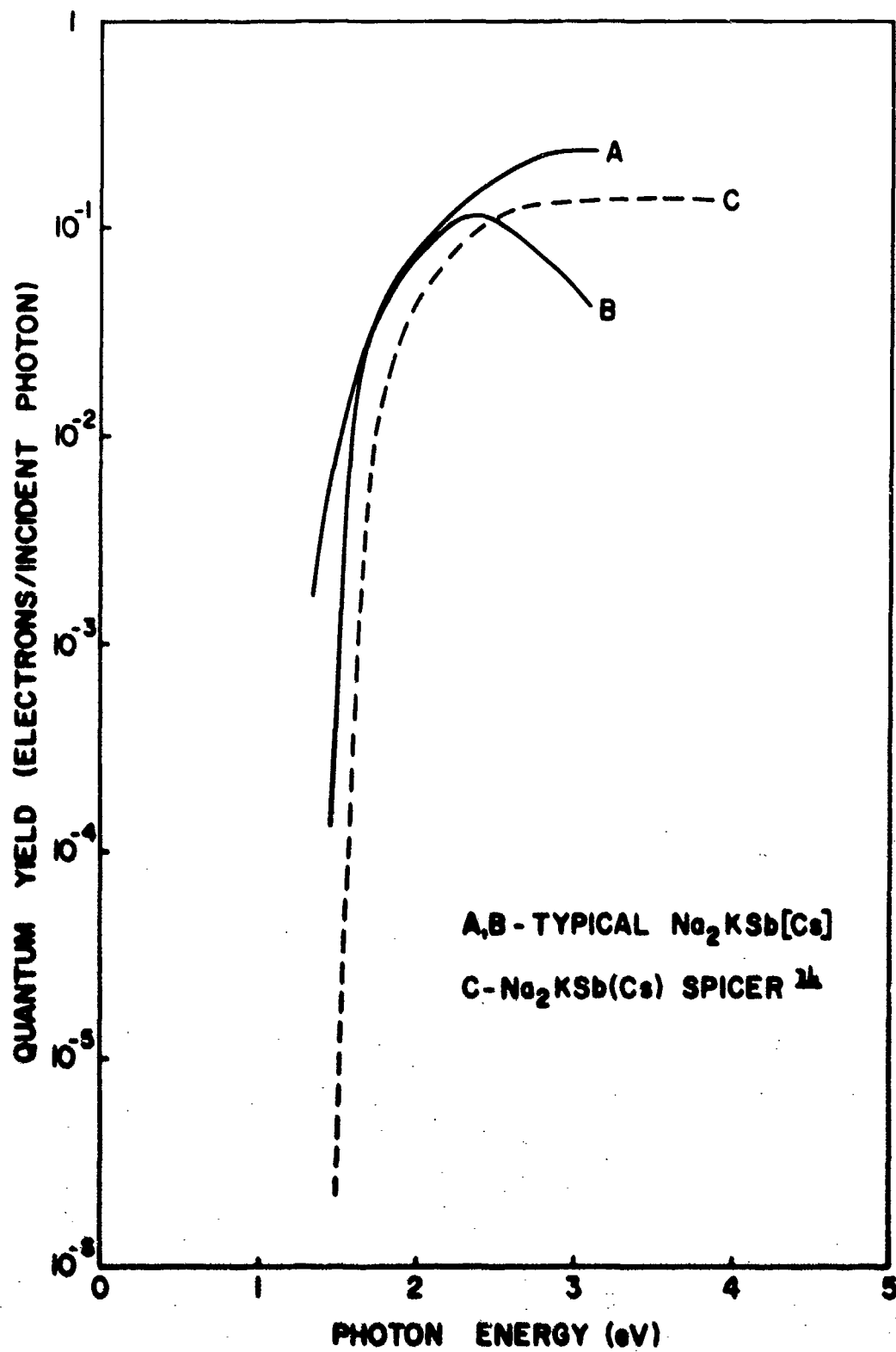


Figure 4 Spectral yield curves for $\text{Na}_2\text{KSb}(\text{Cs})$.

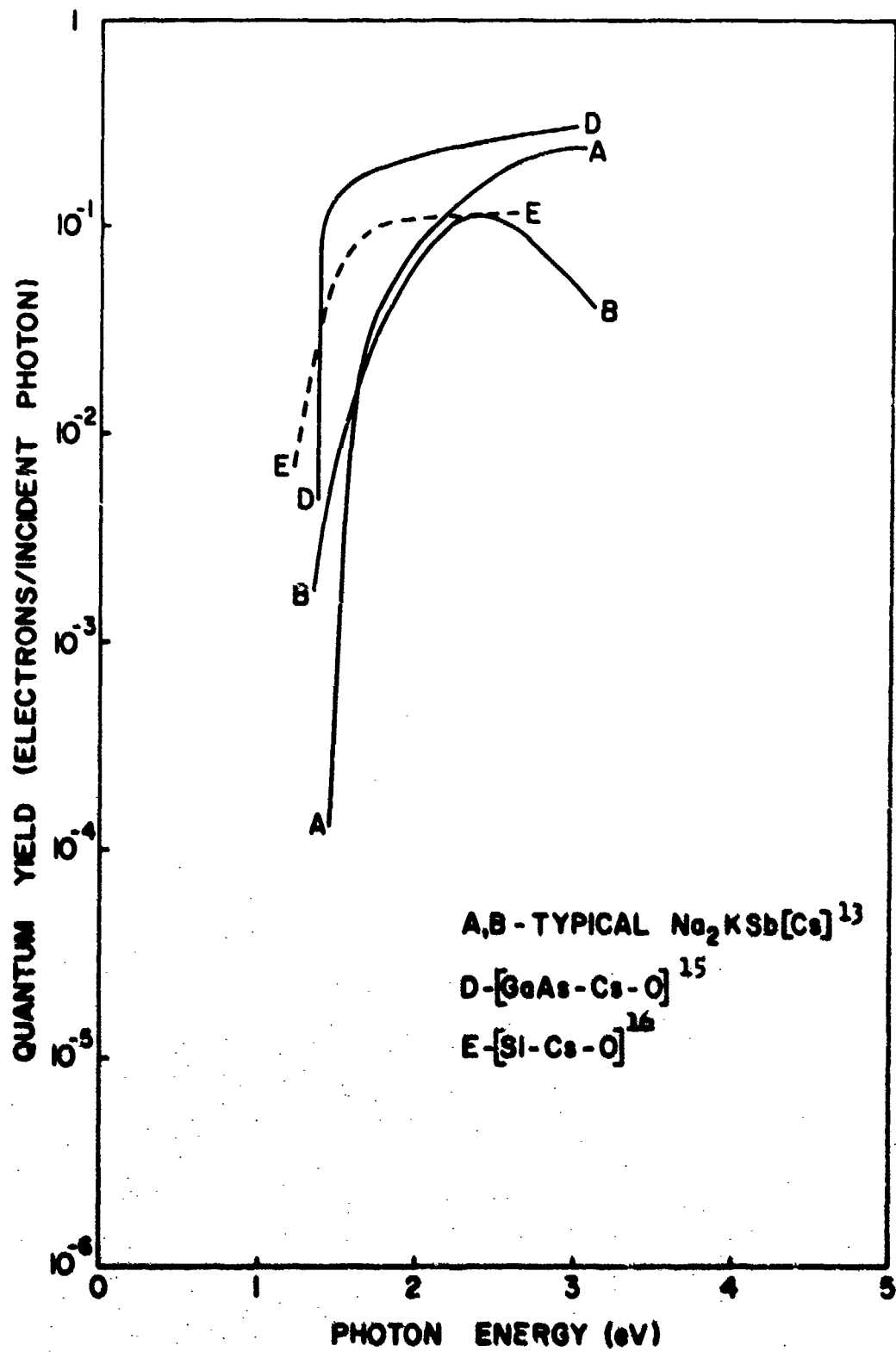


Figure 5 Spectral yield curves for $\text{Na}_2\text{KSb}(\text{Cs})$, $\text{GaAs}-\text{Cs}-\text{O}$, and $\text{Si}-\text{Cs}-\text{O}$ photocathodes.

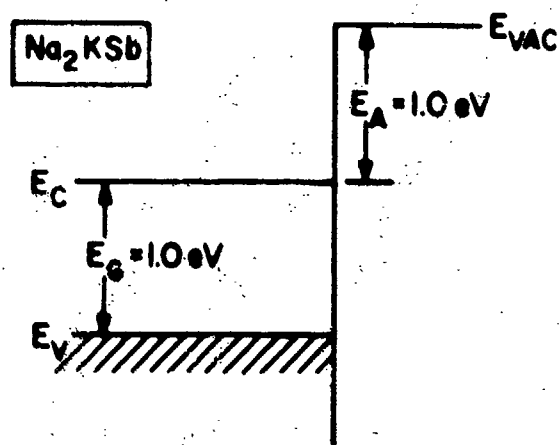


Figure 6A Electron energy band diagram for Na_2KSb .

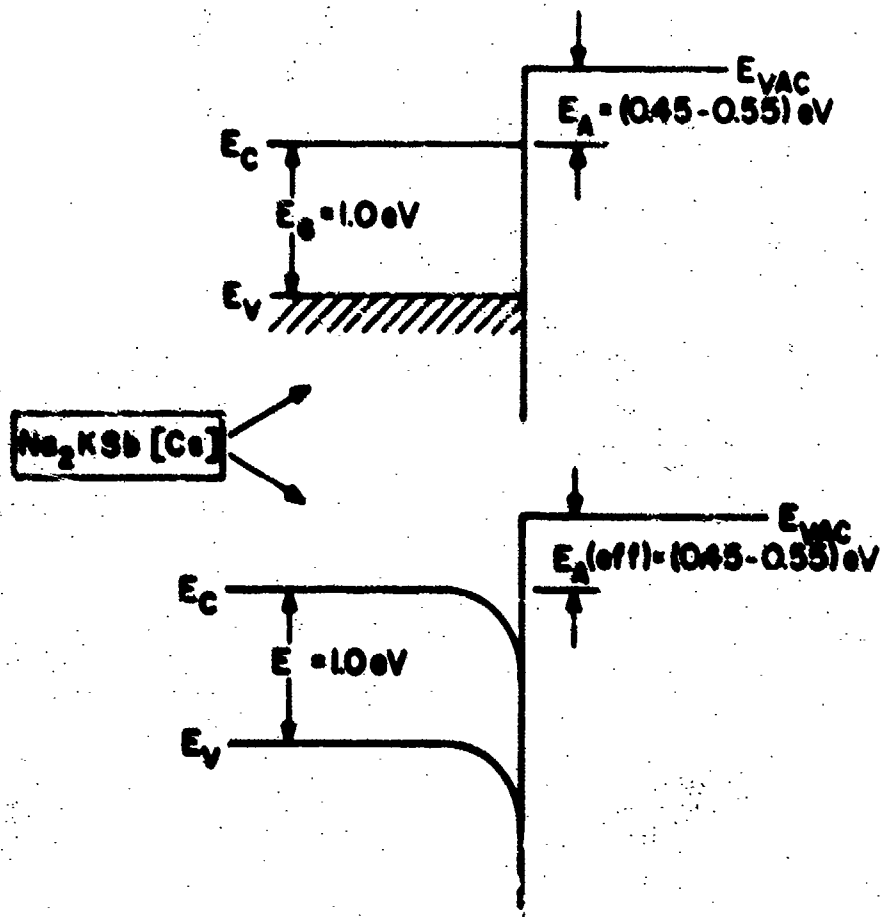


Figure 6B Electron energy band diagram for $\text{Na}_2\text{KSb}(\text{Ce})$.

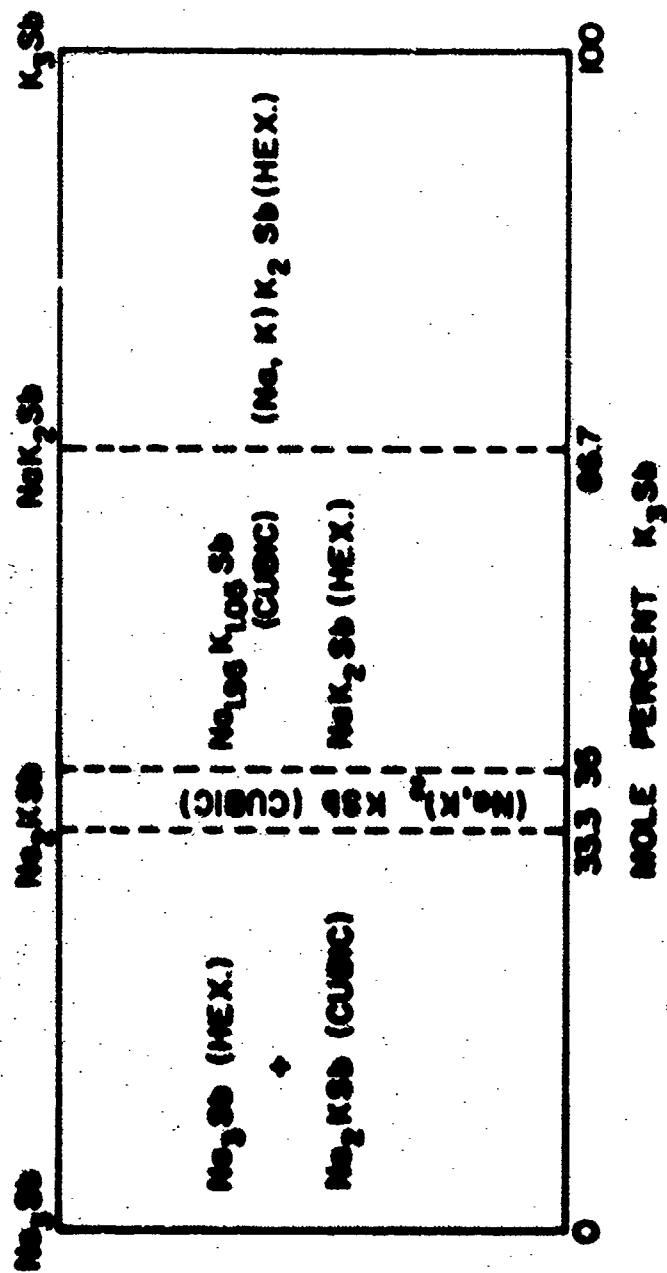


Figure 7 Phases present in the $\text{Na}_3\text{-xK}_x\text{Sb}$ system.

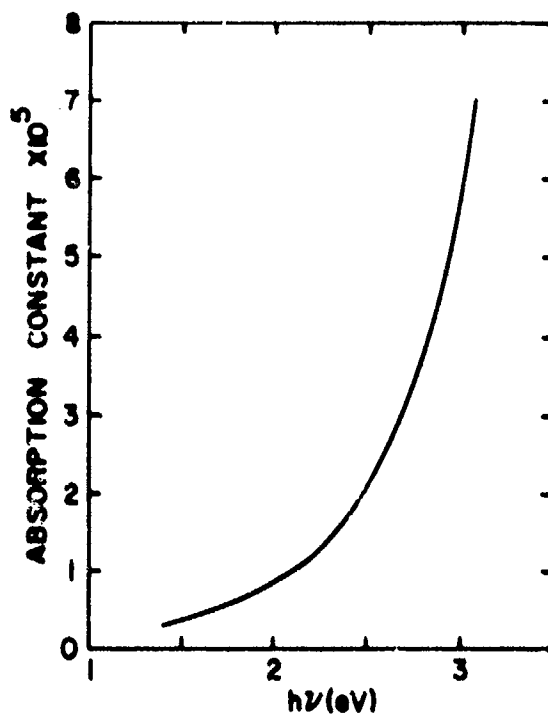


Figure 8 Light absorption of $\text{Na}_2\text{KSb}(\text{Cs})$ as a function of photon energy.⁴³

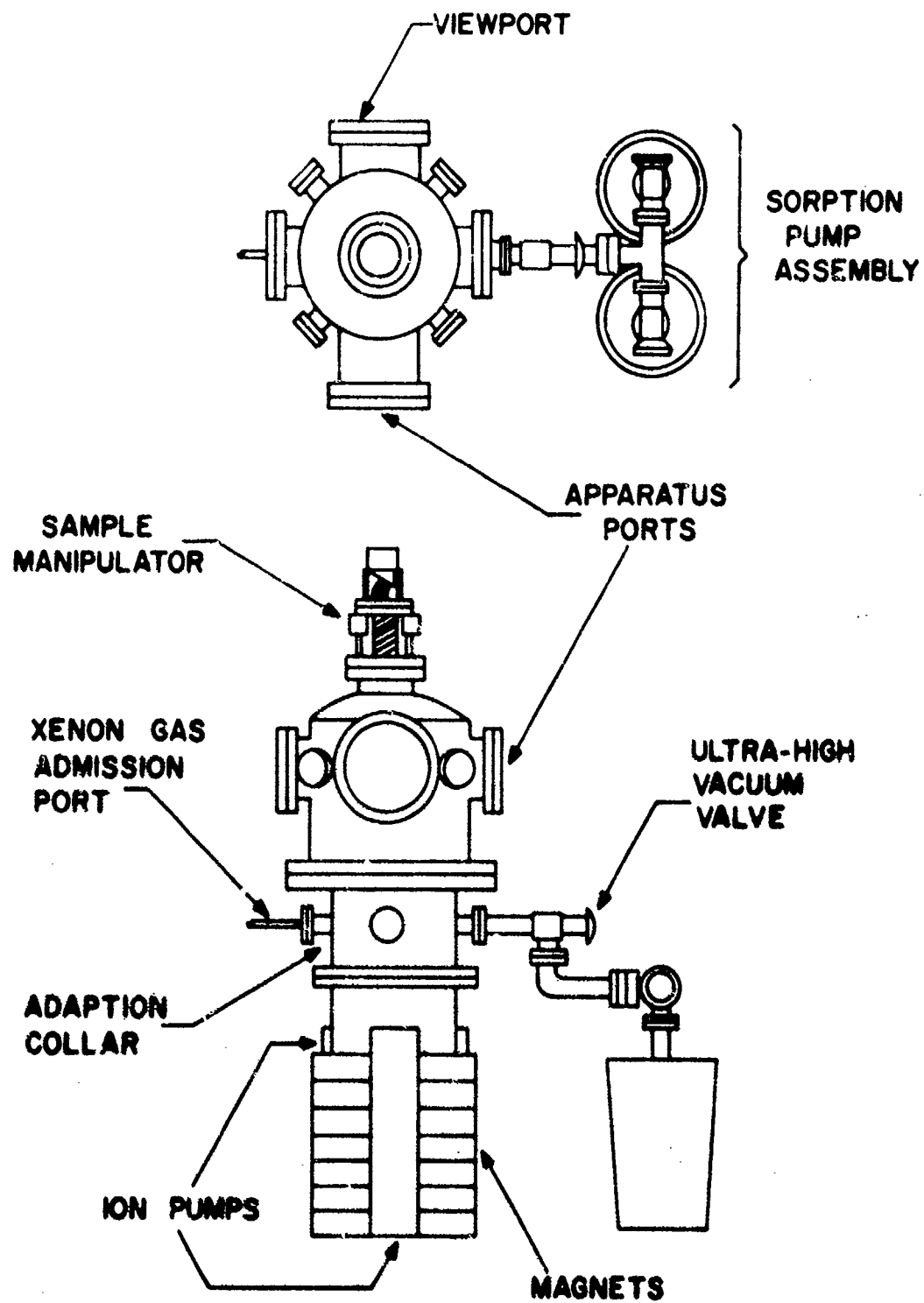


Figure 9 Overall view of vacuum system.

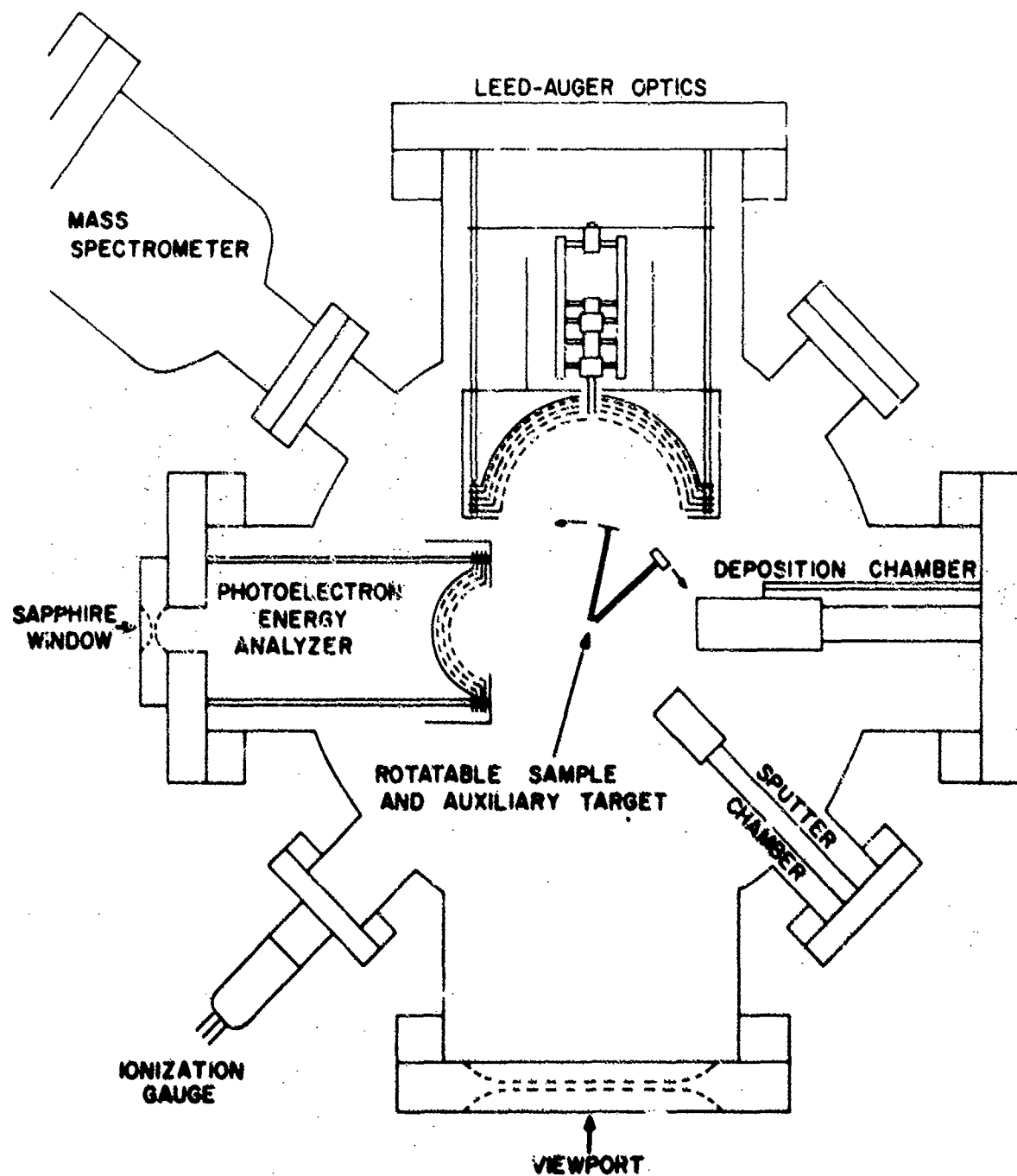


Figure 10 Top view of experimental chamber.

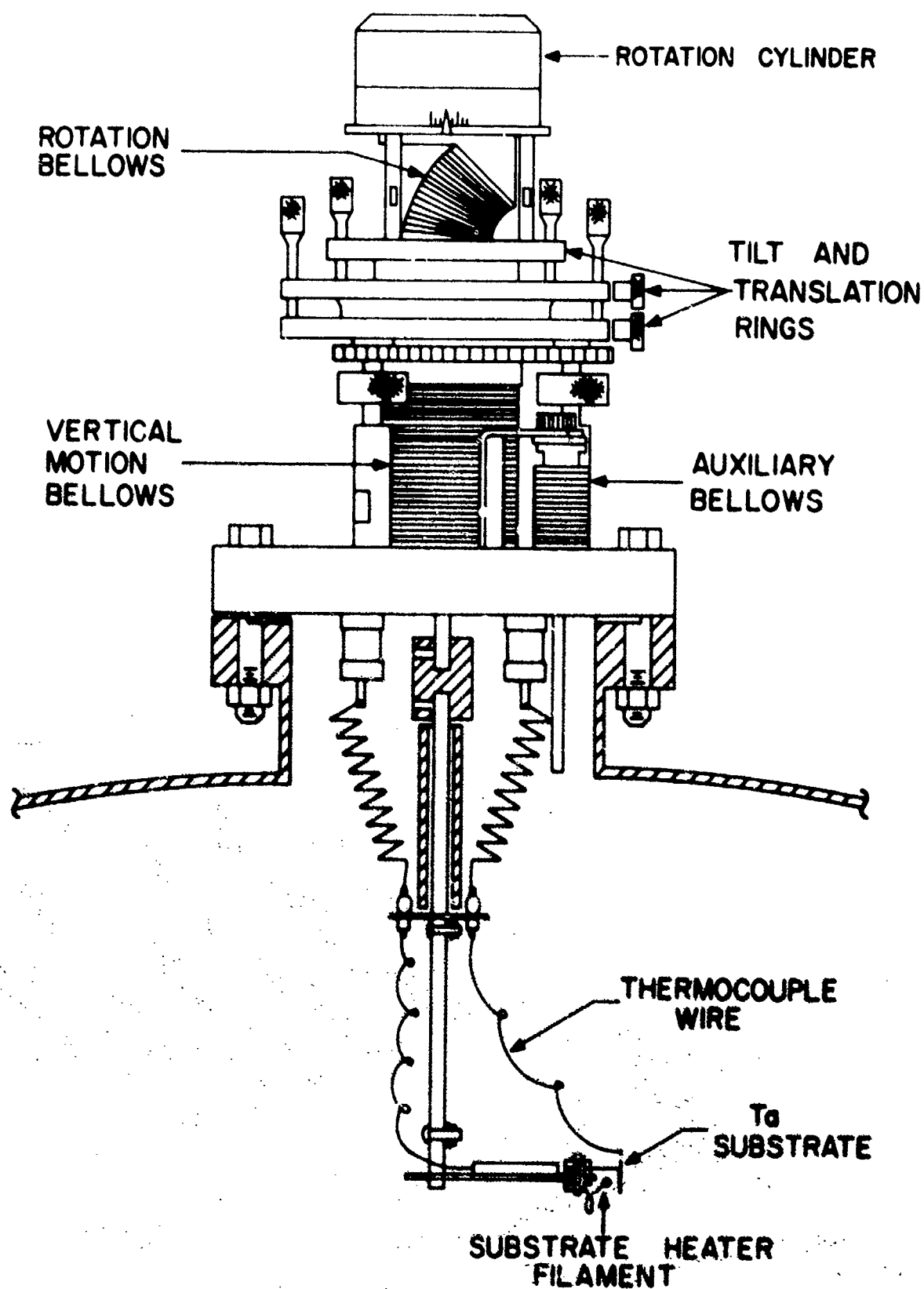


Figure 11 Sample manipulator assembly.

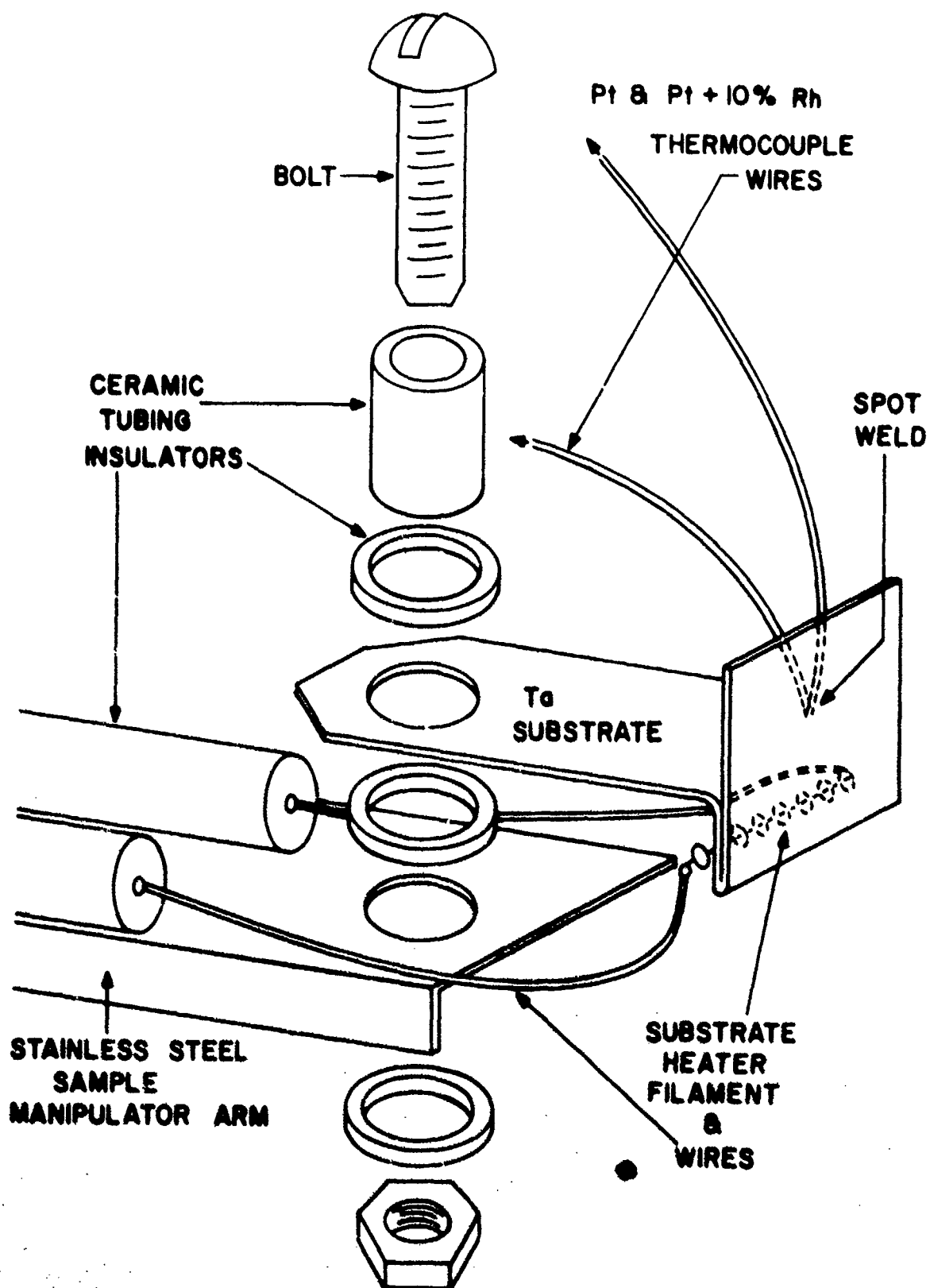


Figure 12 Substrate assembly.

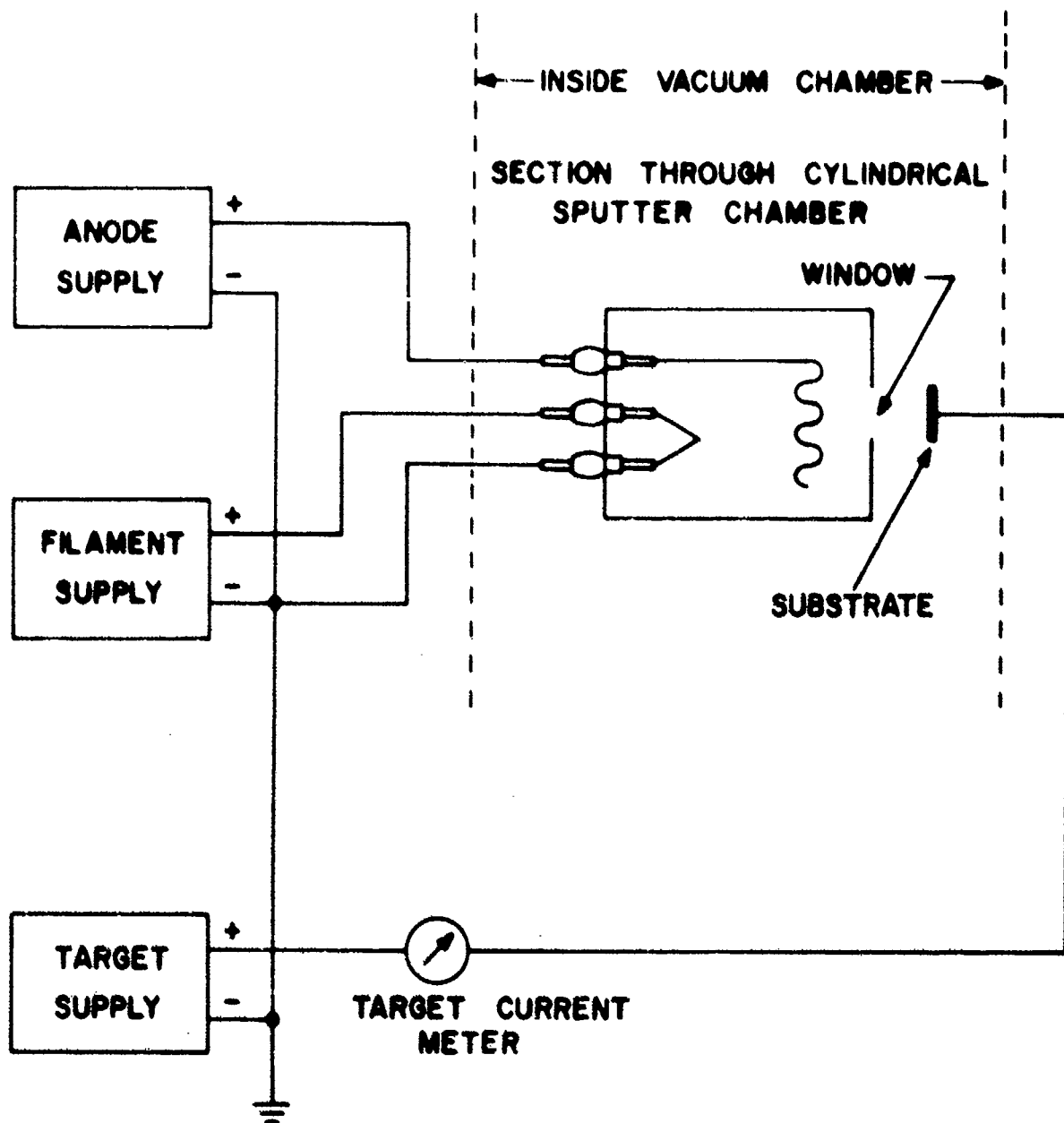
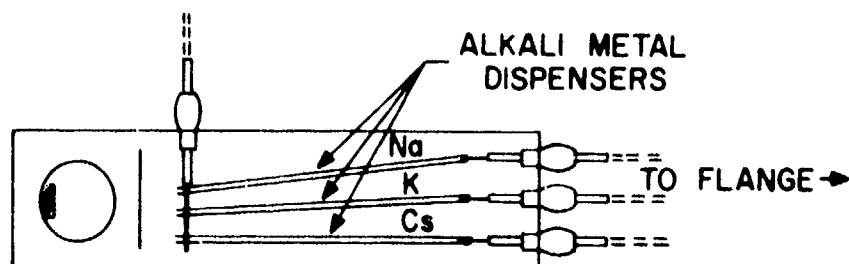
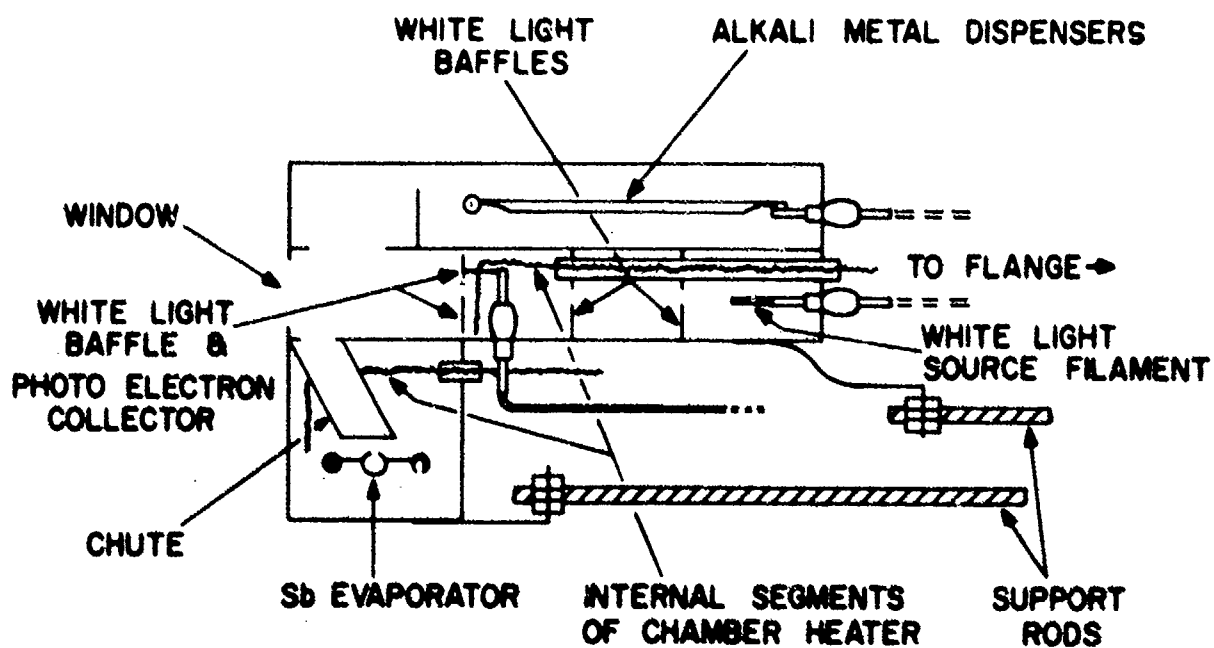


Figure 13 Circuit used for sputter cleaning of substrate.



TOP VIEW - COVER REMOVED
CHAMBER HEATER NOT SHOWN



SIDE VIEW - SECTION THROUGH CENTER
EXTERNAL HEATER NOT SHOWN

Figure 14 Deposition chamber.

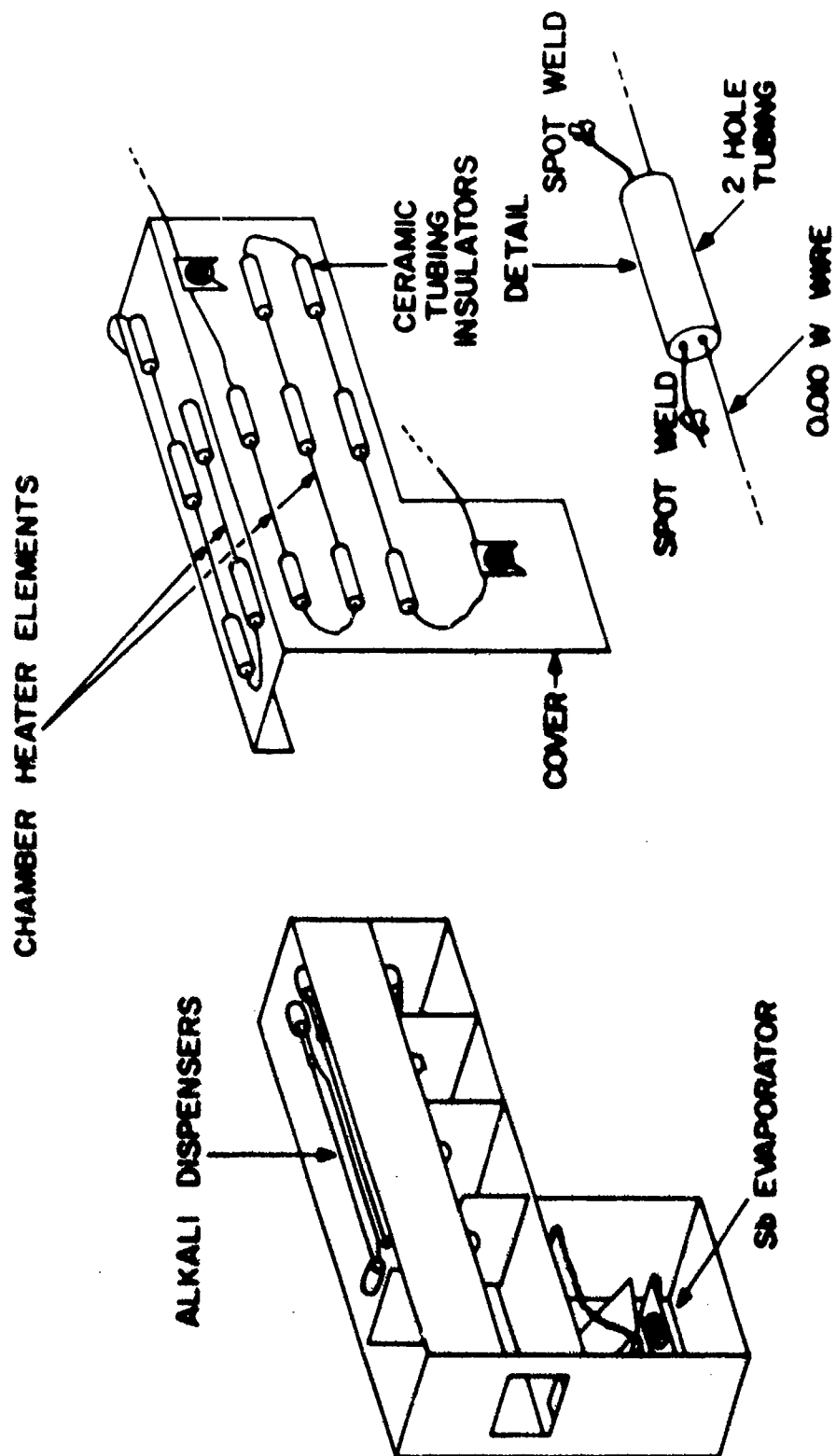


Figure 15 Deposition chamber shown with cover removed.

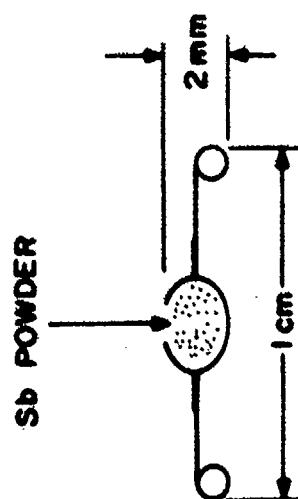
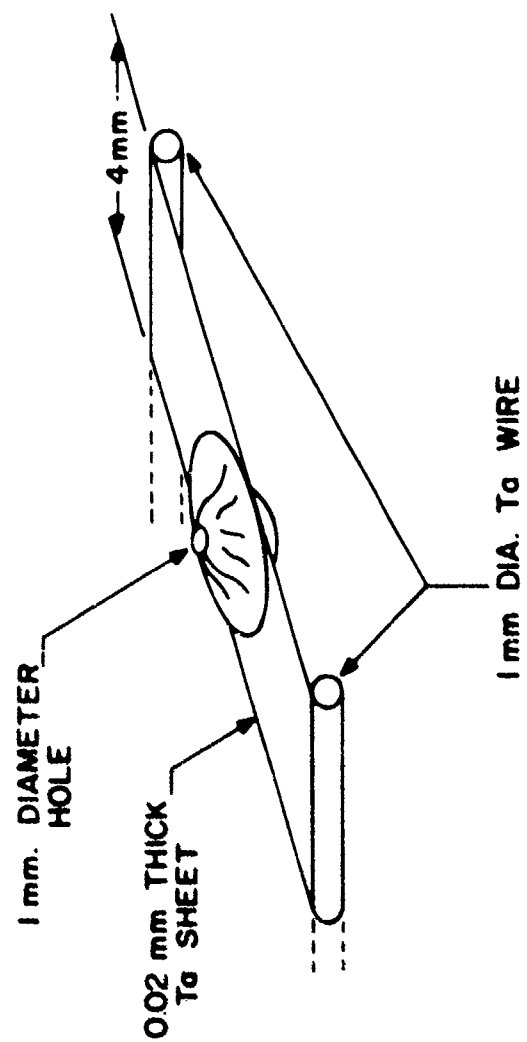


Figure 16 Construction of antimony evaporator.

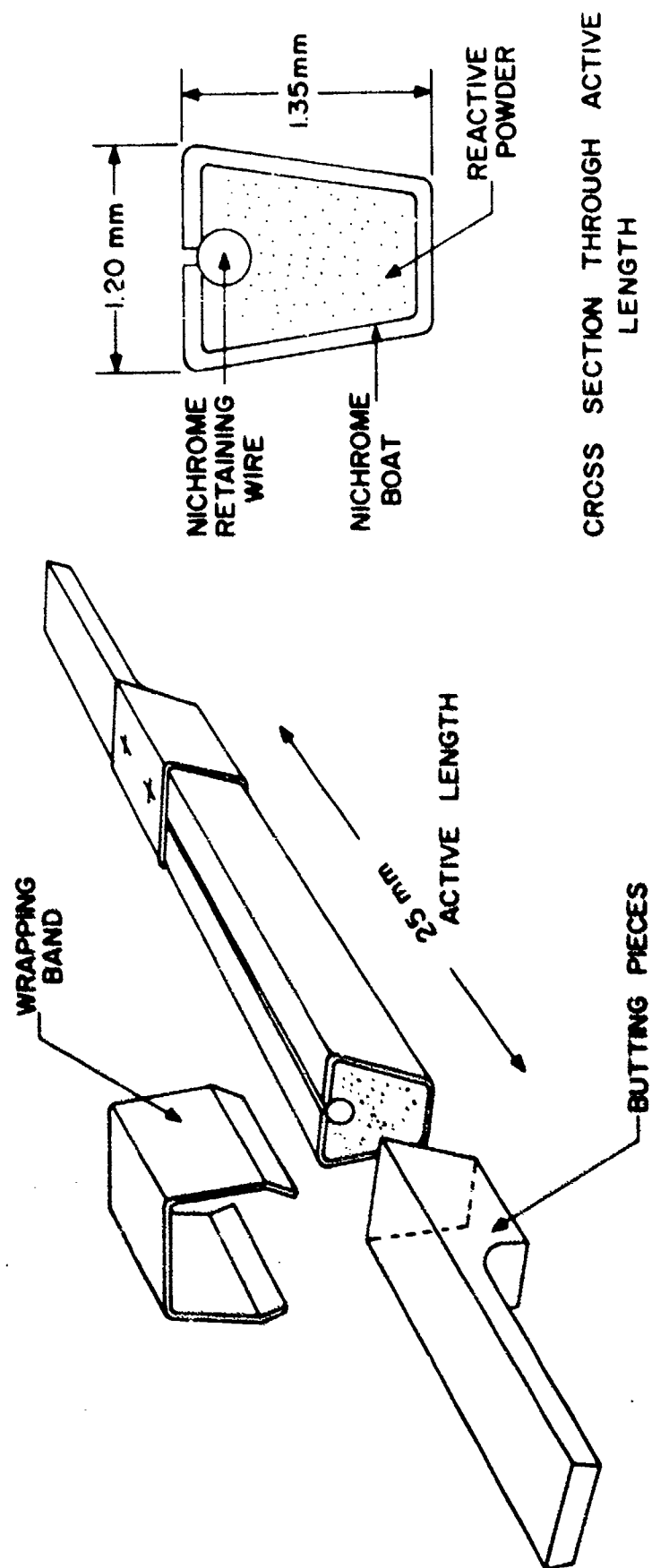


Figure 17 Construction of alkali channels.

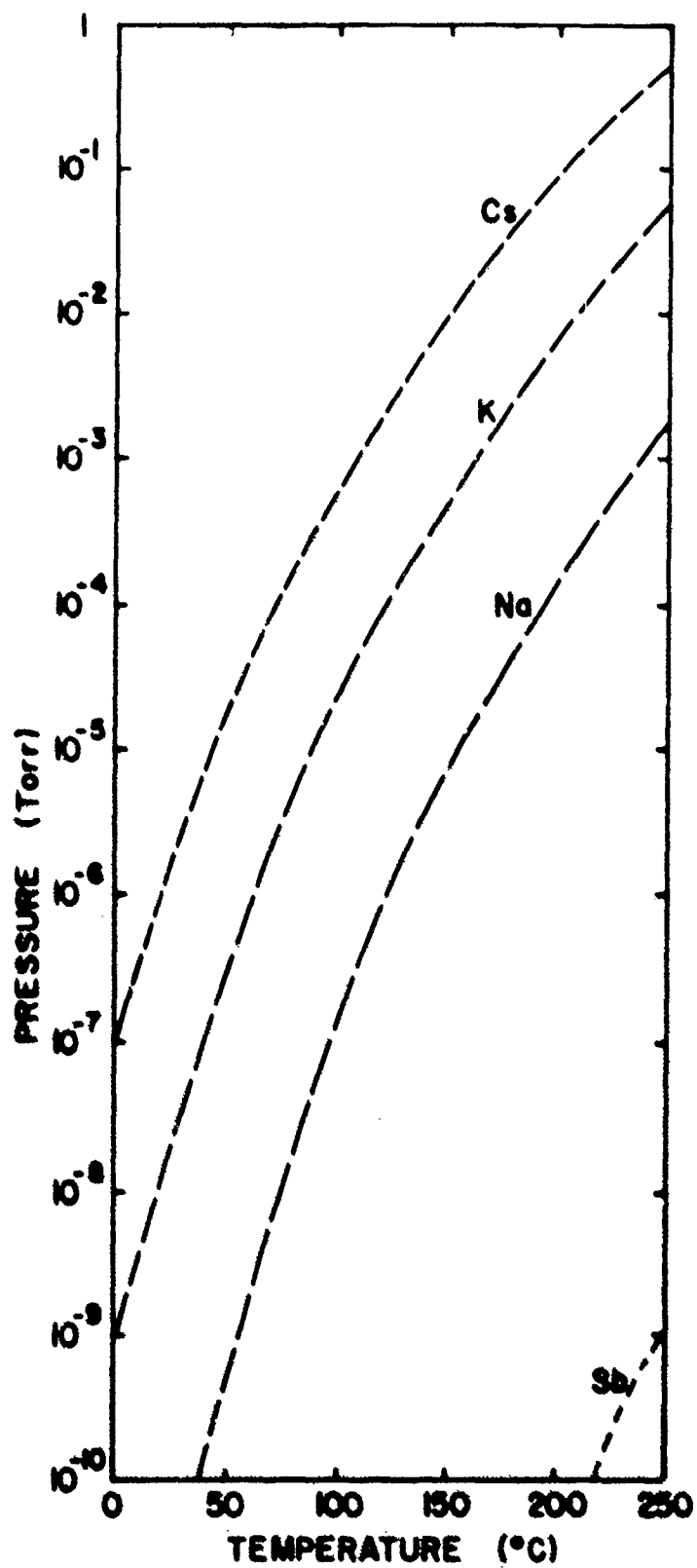


Figure 18 Vapor pressure curves of sample constituents. 45

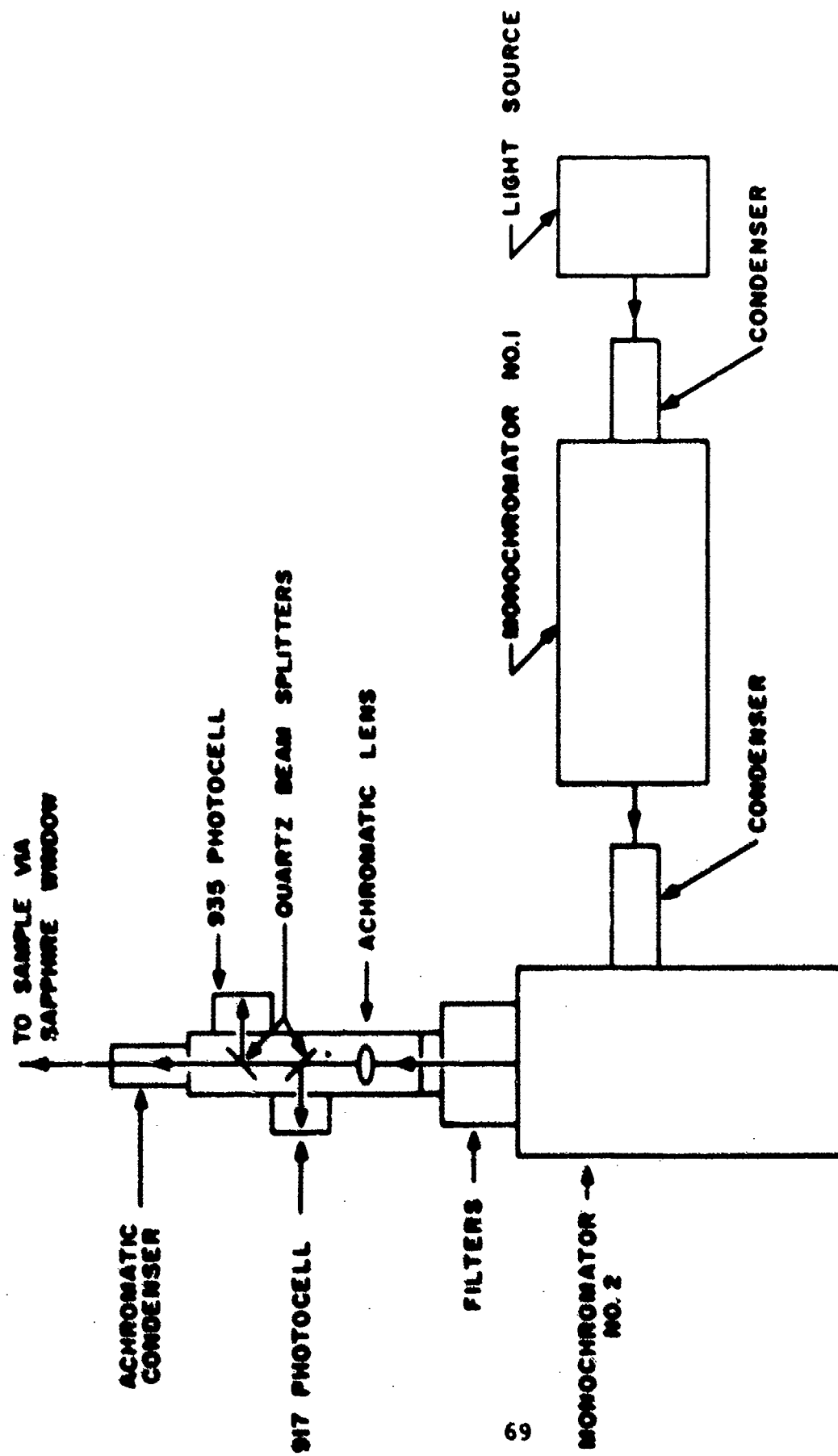


Figure 19 Light source optics for photoemission measurements.

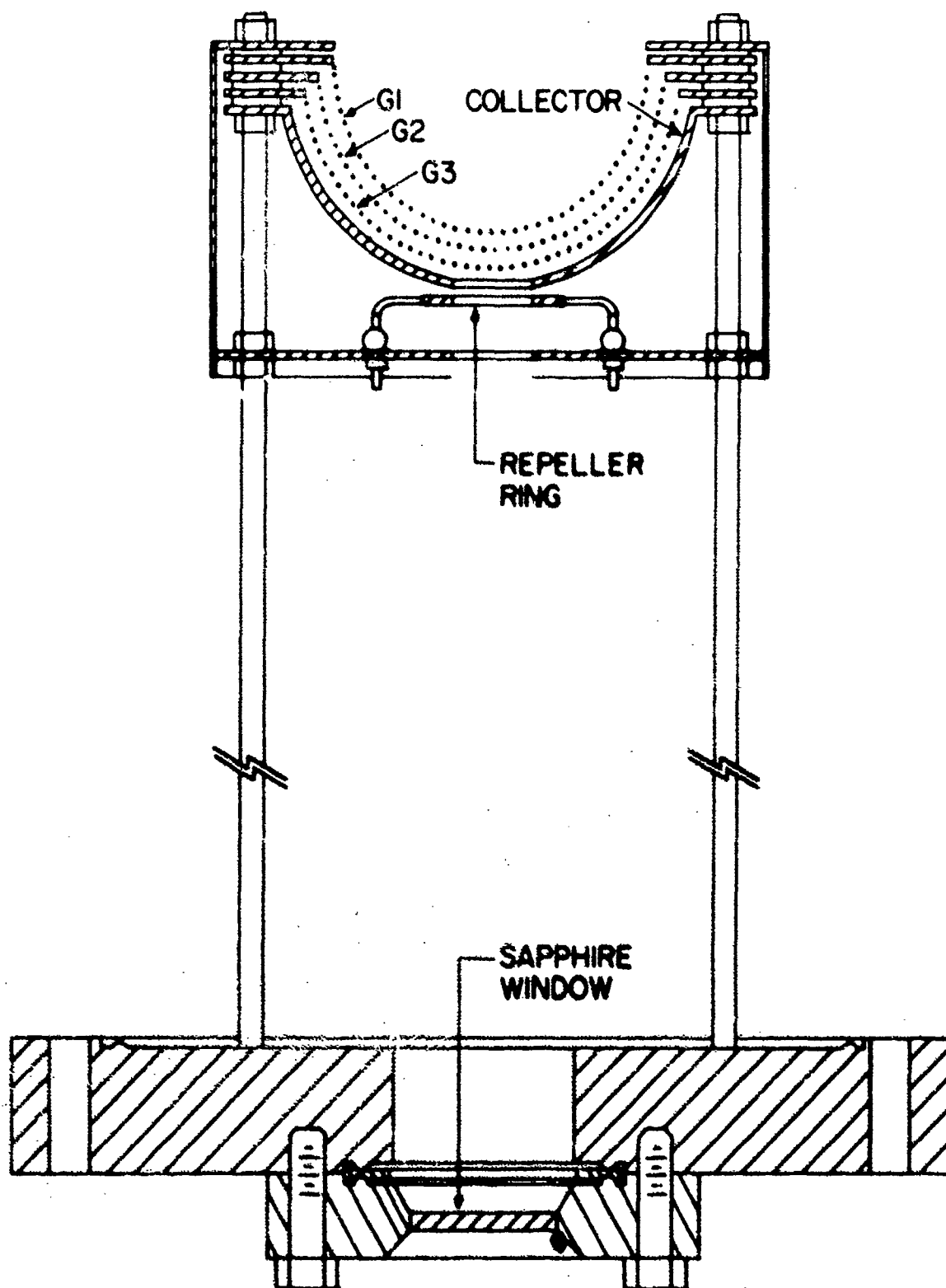


Figure 20 Hemispherical grid system for photoemission measurements.

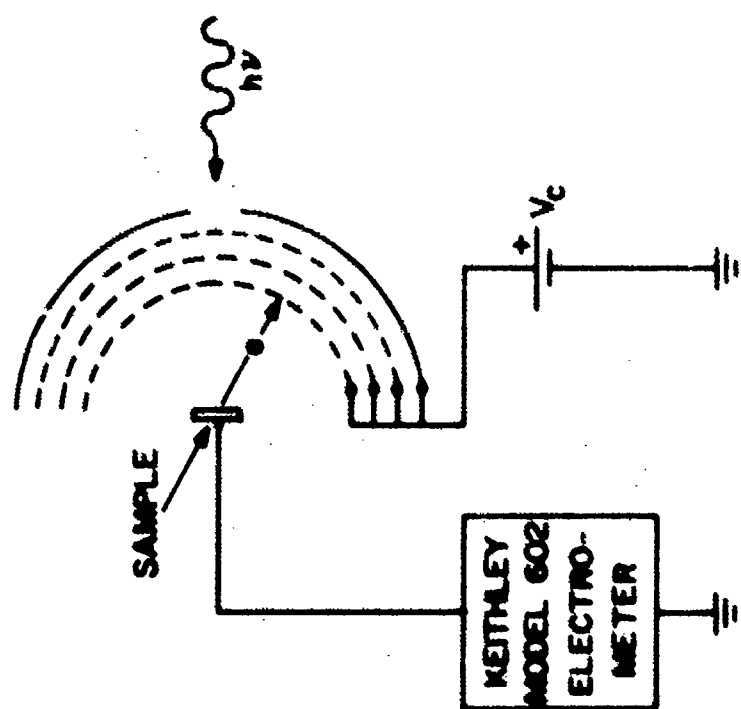


Figure 21 Circuit used for quantum yield measurements.

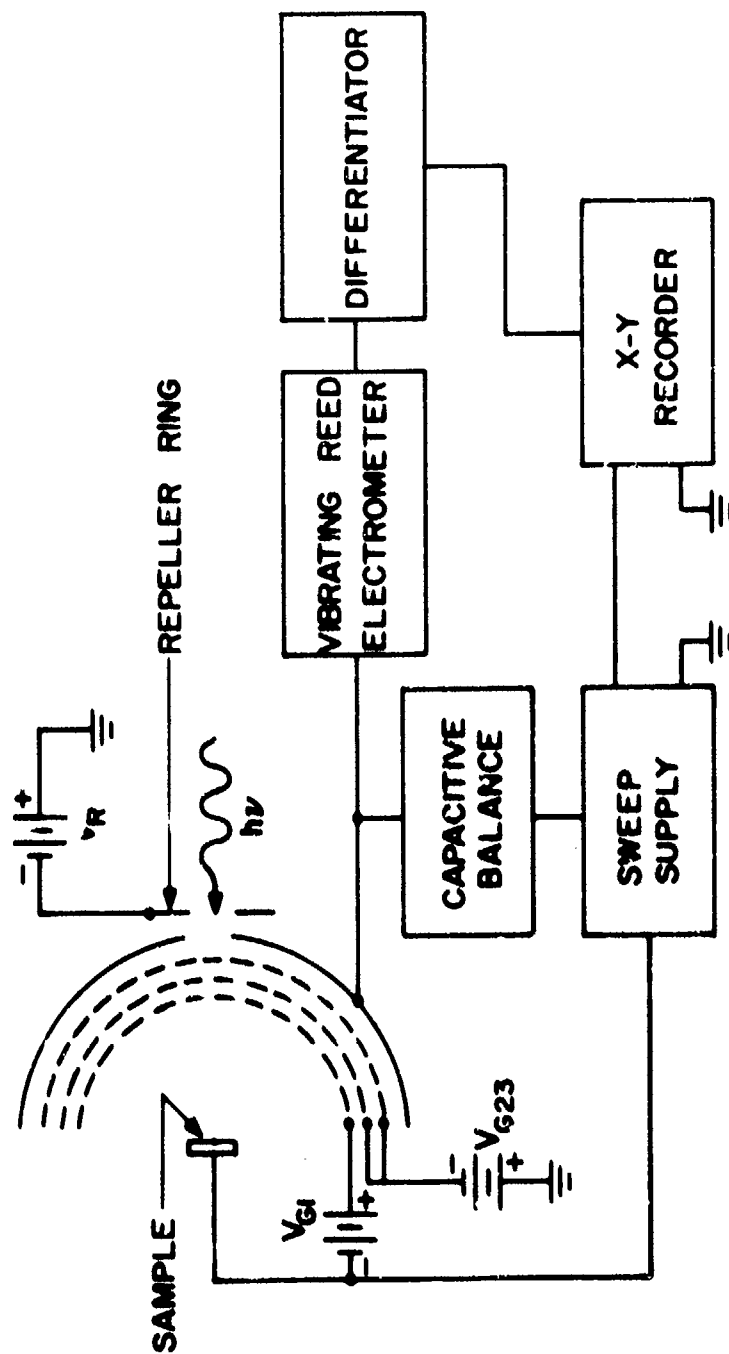


Figure 22 Circuit used for measurement of energy distributions of photoelectrons.

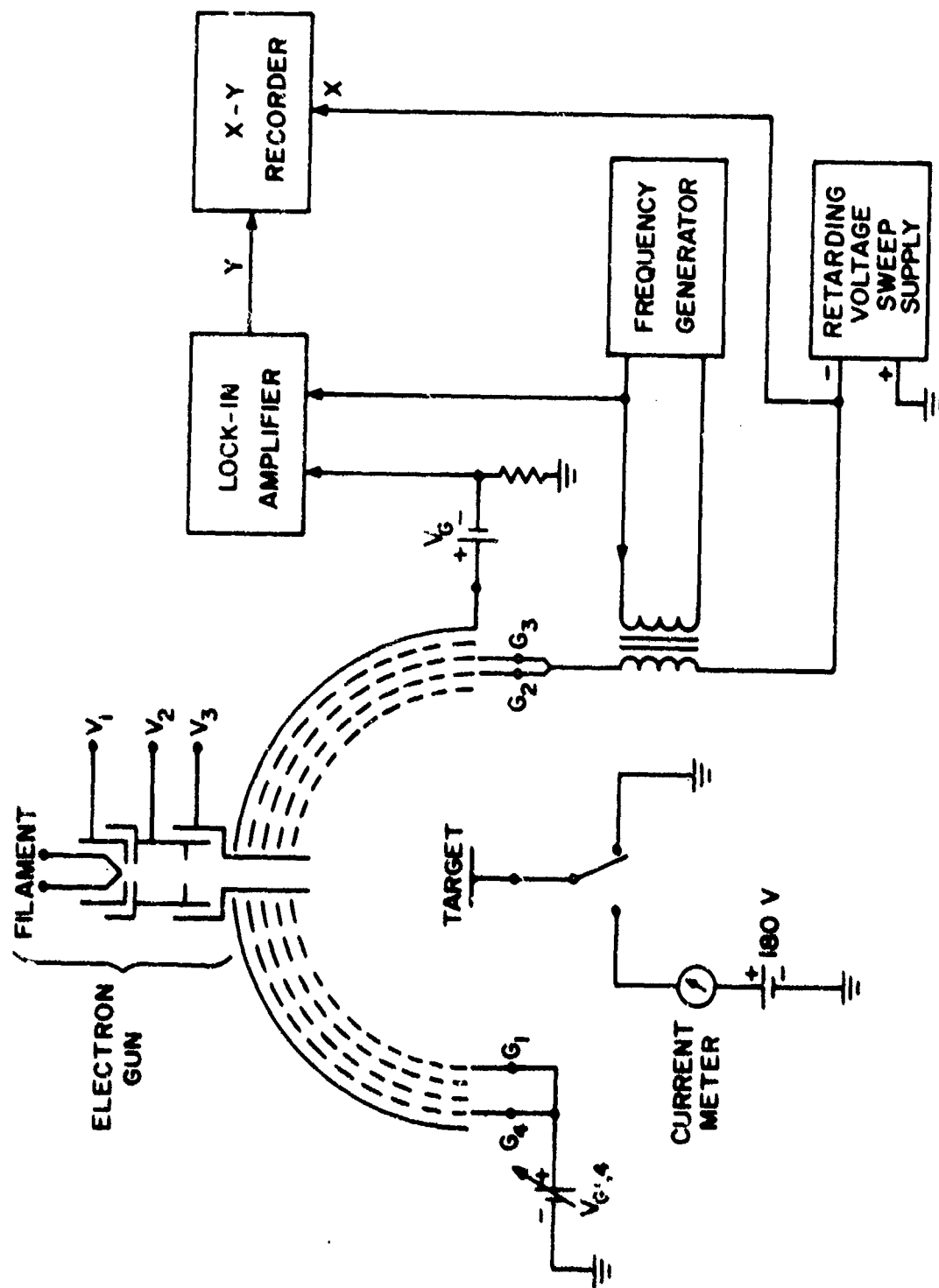


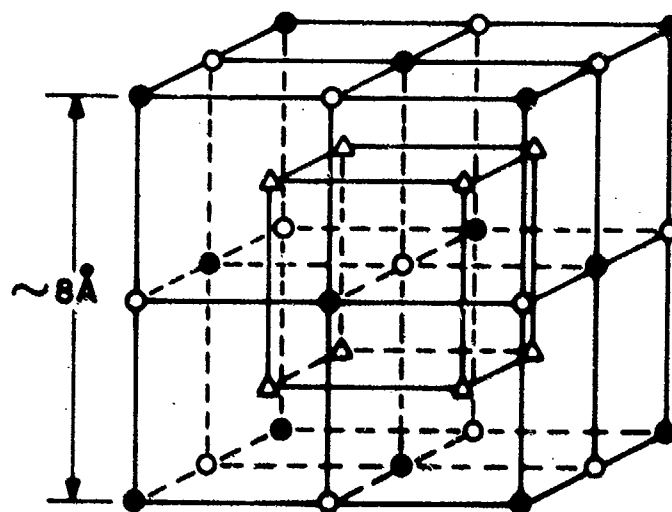
Figure 23 Circuit used for Auger electron spectroscopy measurements.

Element	Energy of AES peak (eV)	Atomic shells involved in Auger electron emission	Escape depth of Auger electrons (Å)
Sb	455-465	MNN	9
Na	990	KLL	12
K	250	LMM	7
Cs	47	NOO	5
Cs	565-575	MNN	10
Ta	160-180	MNN	5
O	515	KLL	9
C	275	KLL	7
Cl	180	LMM	5
S	150	LMM	5
N	385	KLL	8

Figure 24 Information regarding principal Auger electron energy peaks found in these studies.

UNIT CELL OF Na_2KSb

● - Sb , ○ - K , △ - Na



UNIT CELL OF Na_3Sb AND HEXAGONAL K_3Sb

● - Sb , ○ - Na OR K

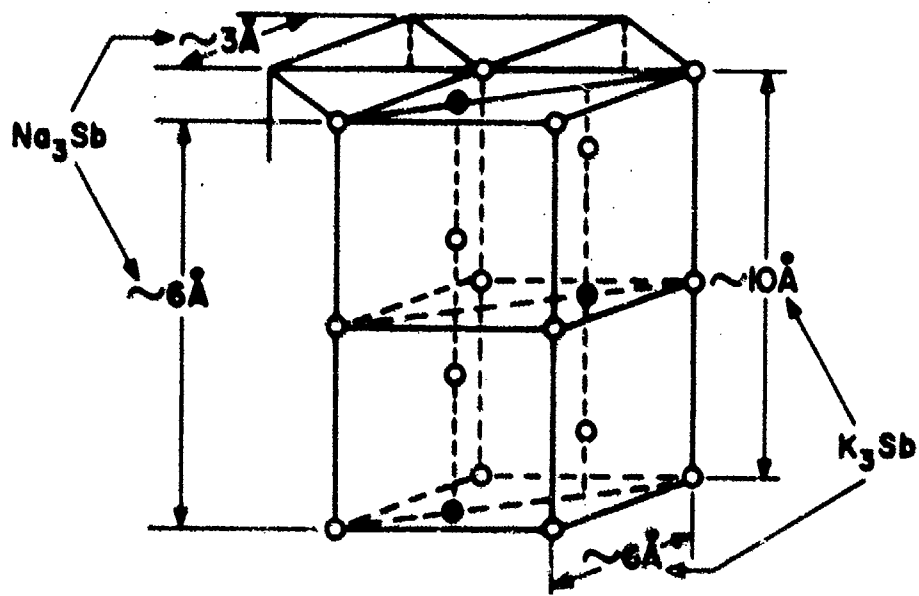


Figure 25 Crystal lattice structures for Na_3Sb , K_3Sb and Na_2KSb .

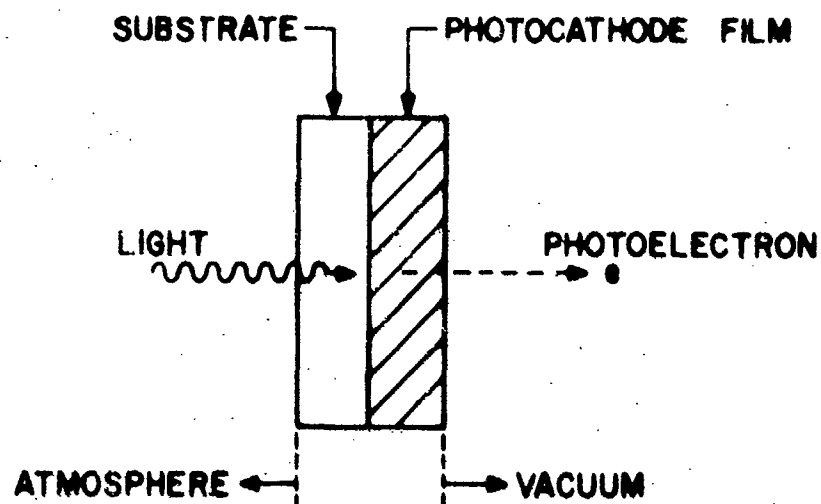


Figure 26A Transmission mode application of photocathode.

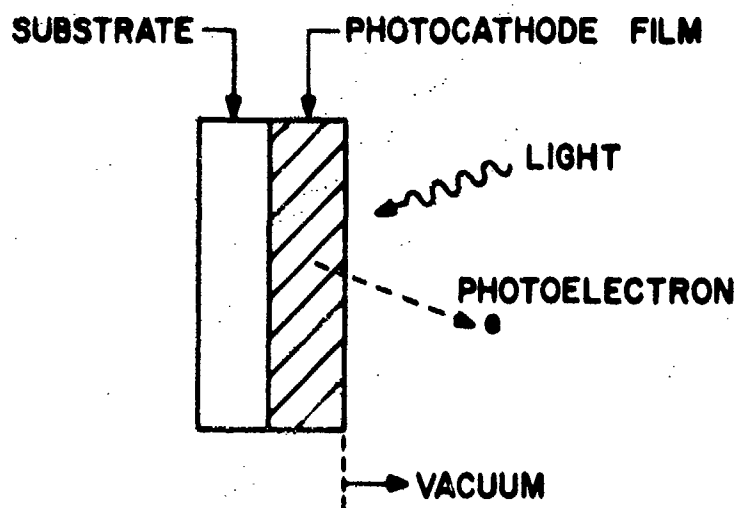


Figure 26B Reflection mode application of photocathode.

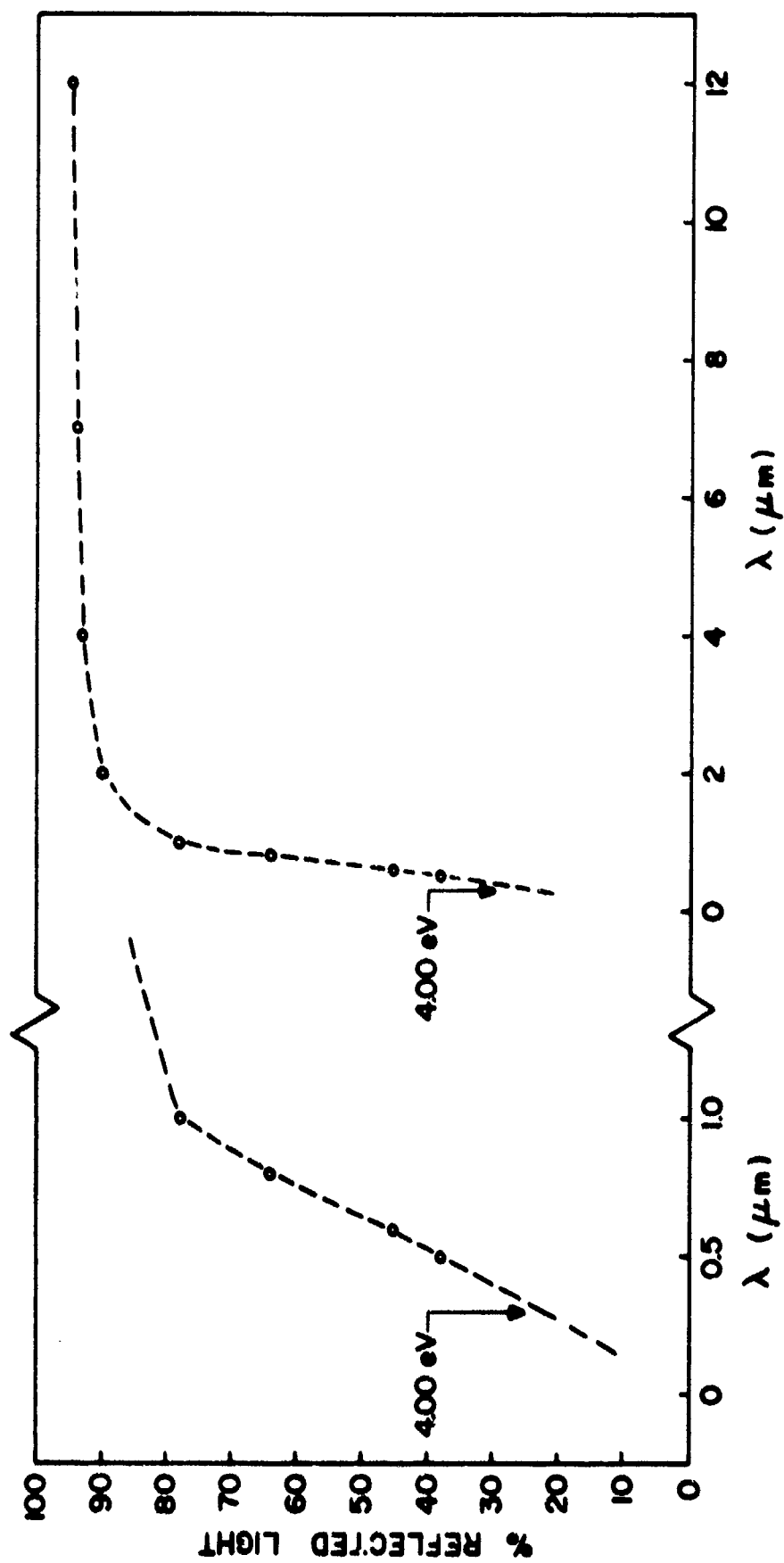


Figure 27 Reflectivity of Ta vs. wavelength of incident light. 46

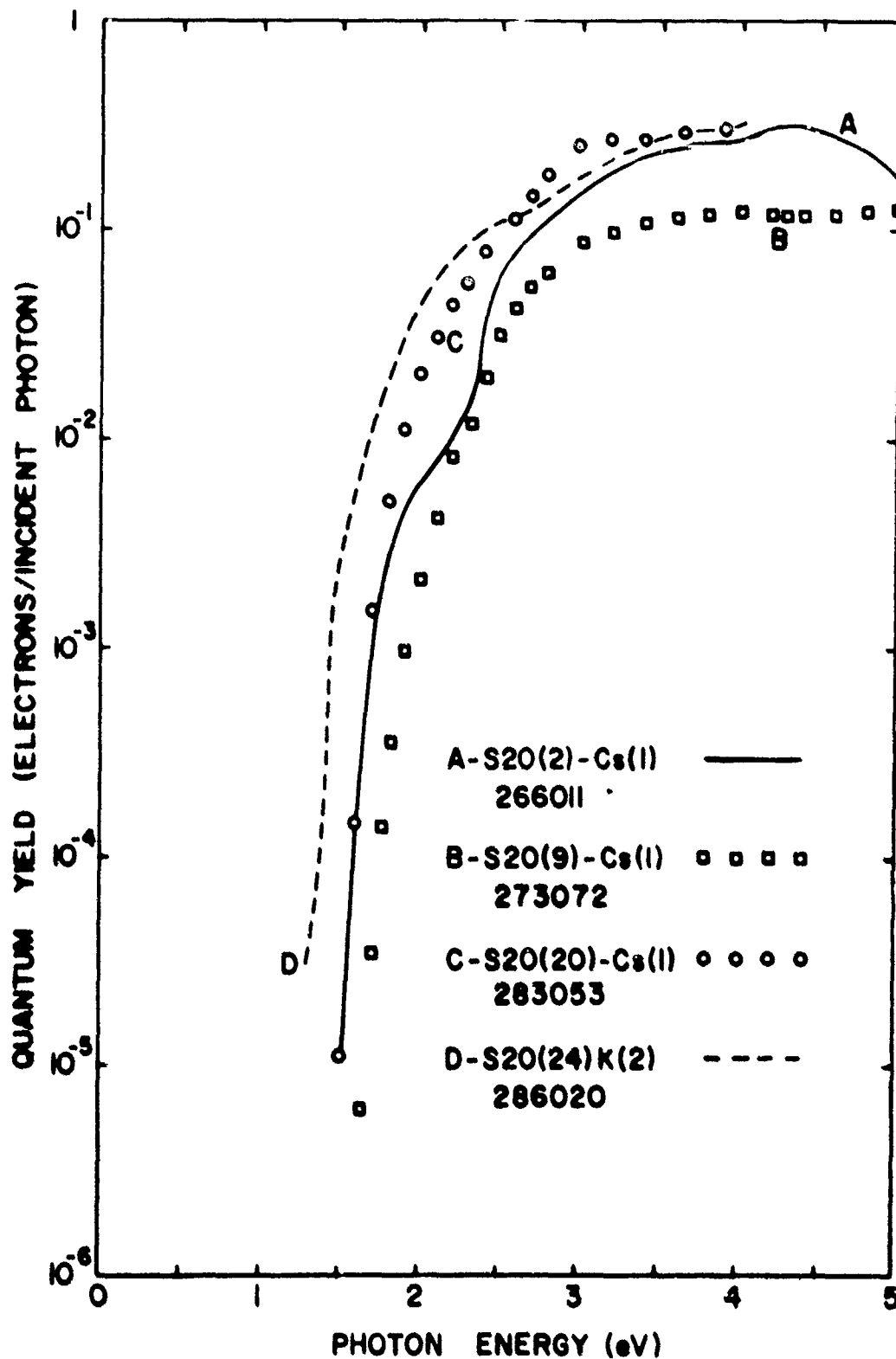


Figure 28 Spectral yield results for samples on differing substrates.

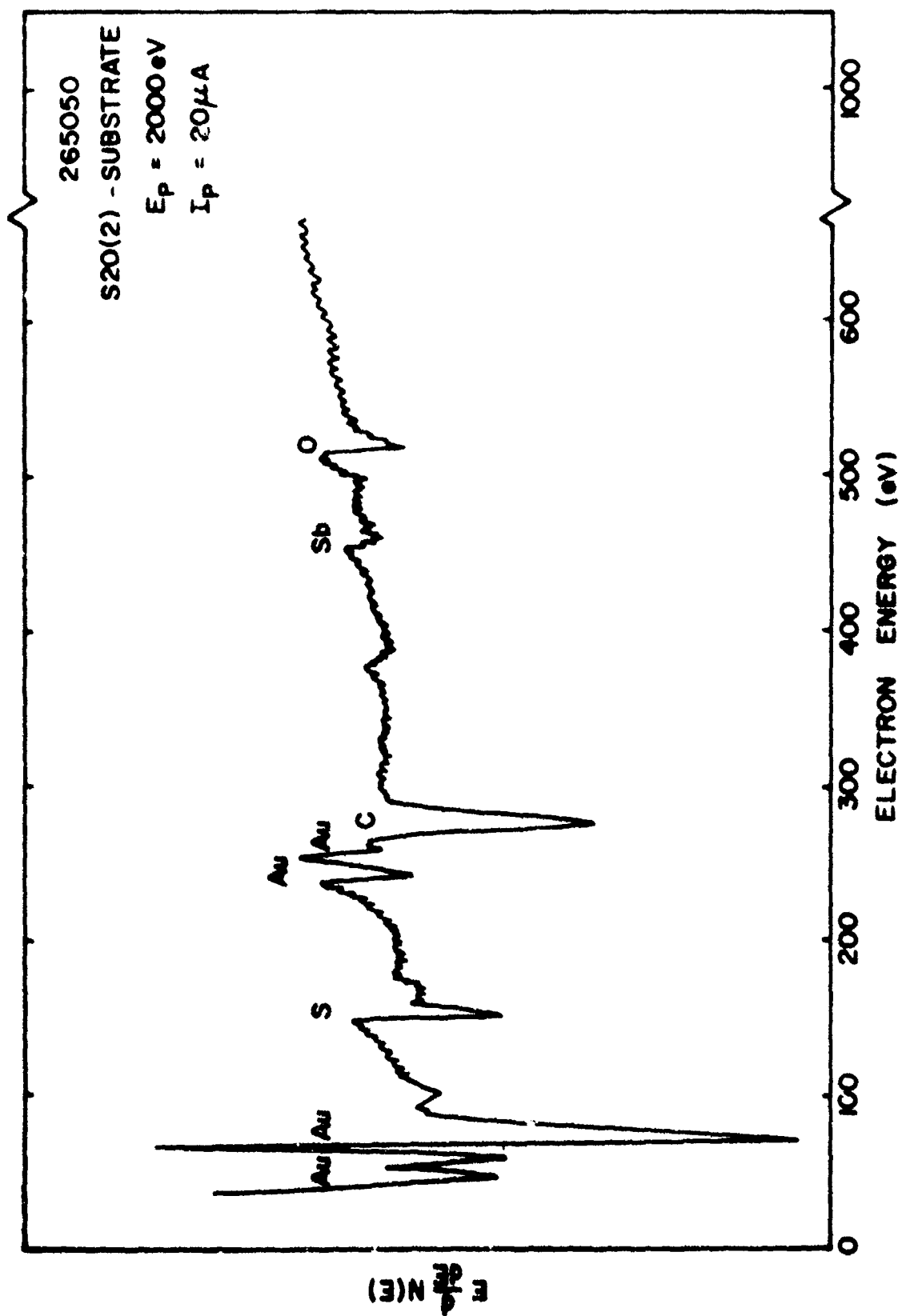


Figure 29 AES results from glass-Au substrate.

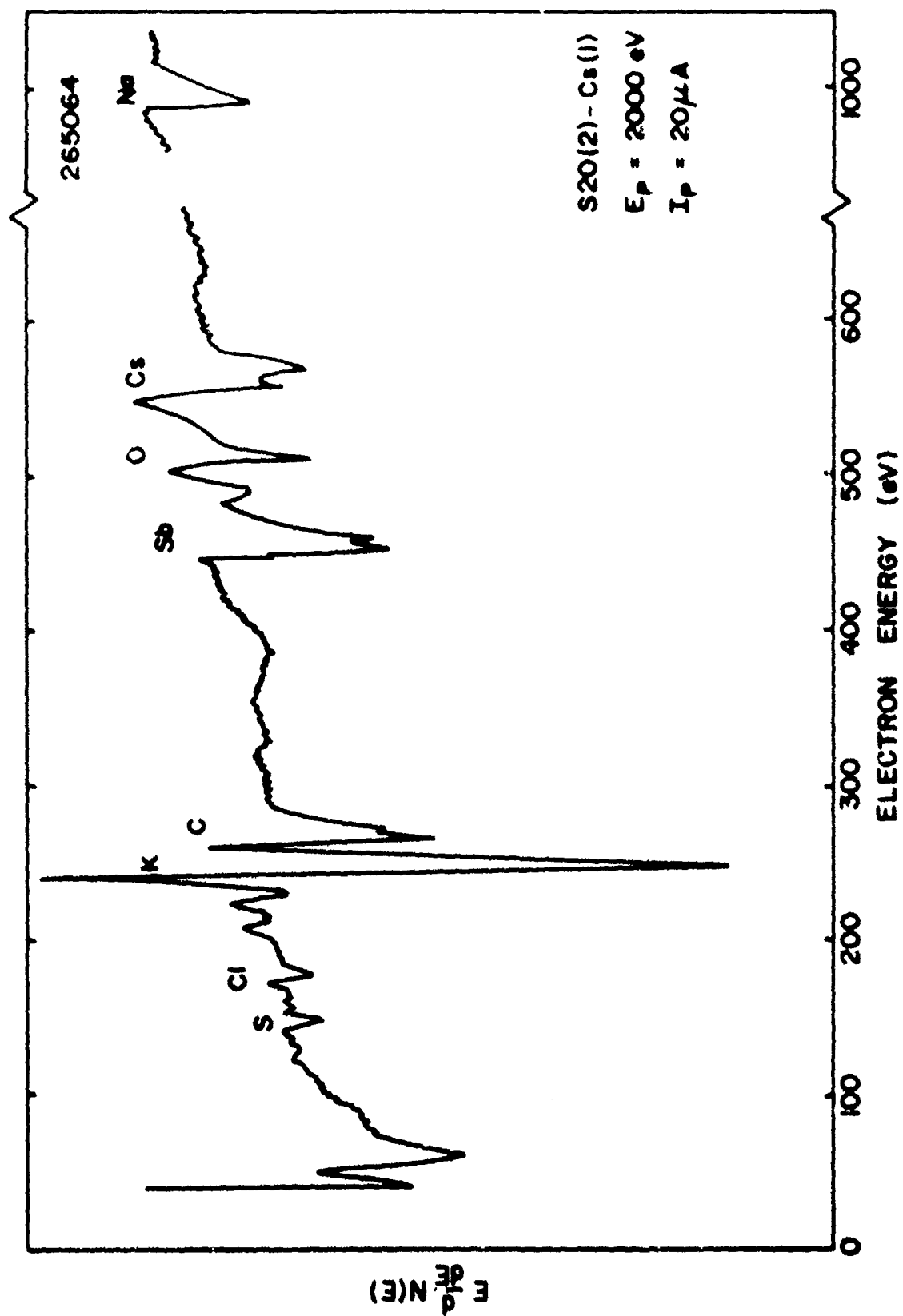


Figure 30 AES results from sample with peak spectral yield of those deposited on glass-Au substrates.

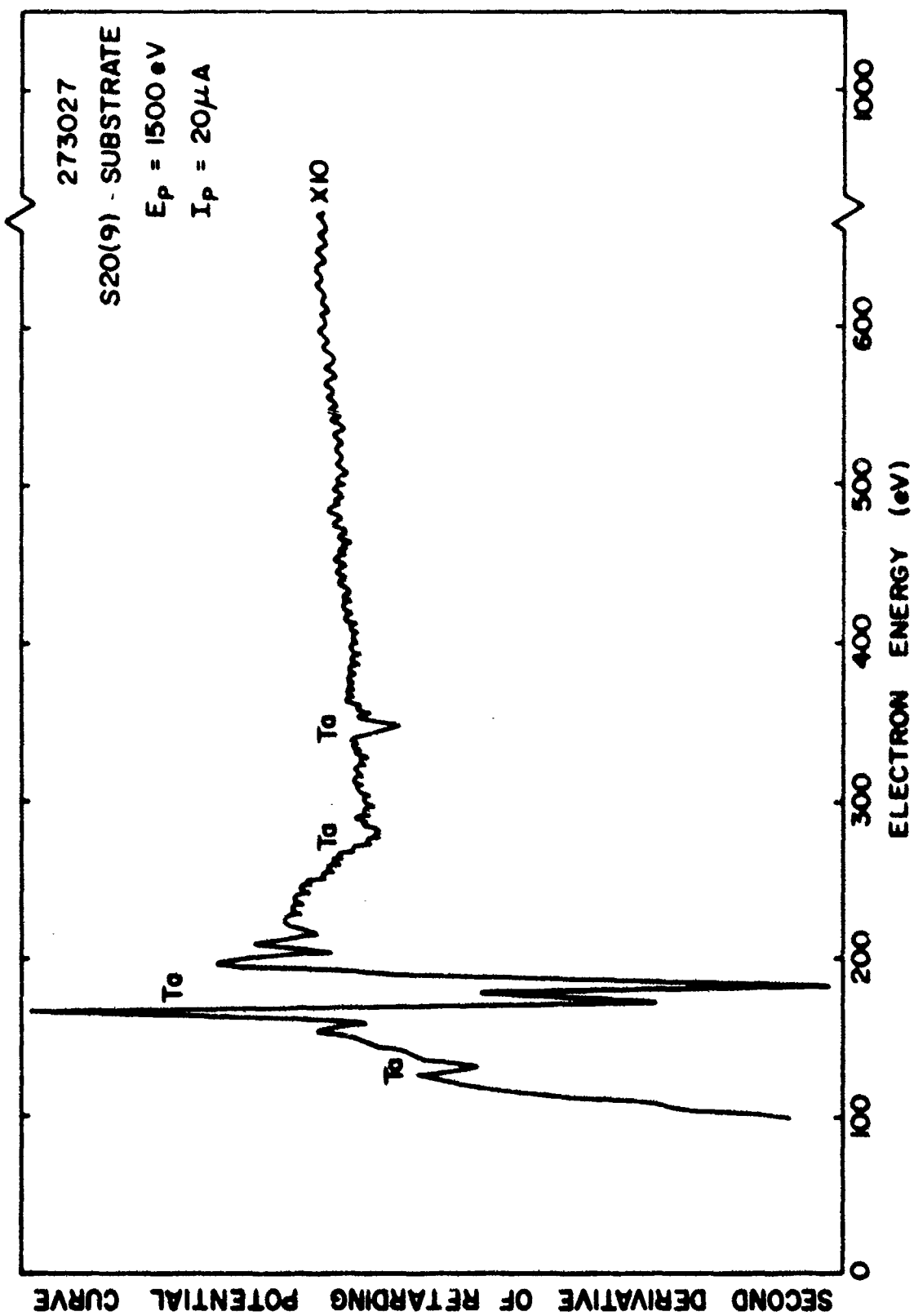


Figure 31 AES results from sputter cleaned Ta substrate.

SECOND DERIVATIVE OF RETARDING POTENTIAL CURVE

273073

S20(9) - Cs(1)

$E_p = 1500 \text{ eV}$

$I_p = 20 \mu\text{A}$

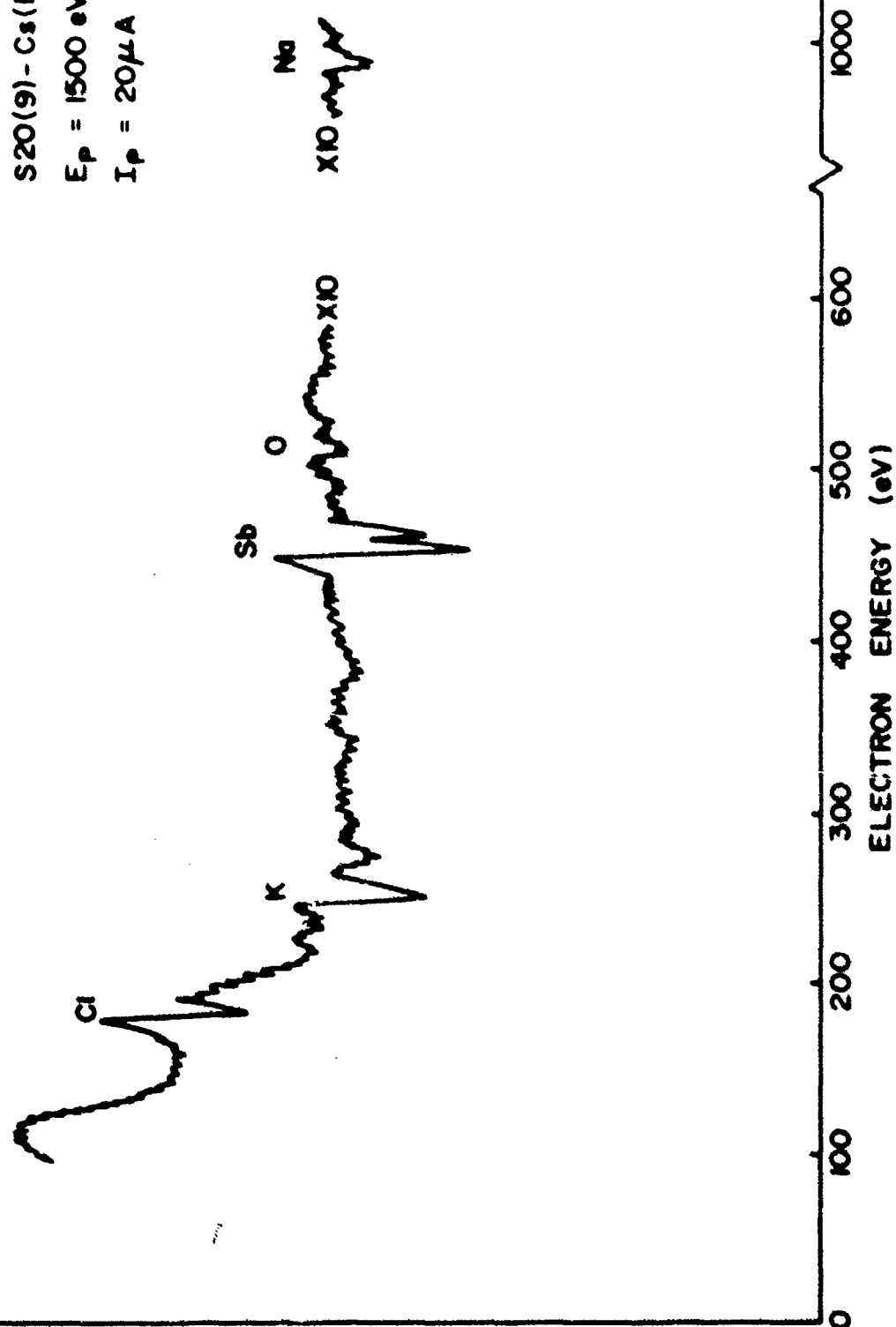


Figure 22 AES results from sample with peak spectral yield of those deposited on a clean Ta substrate.

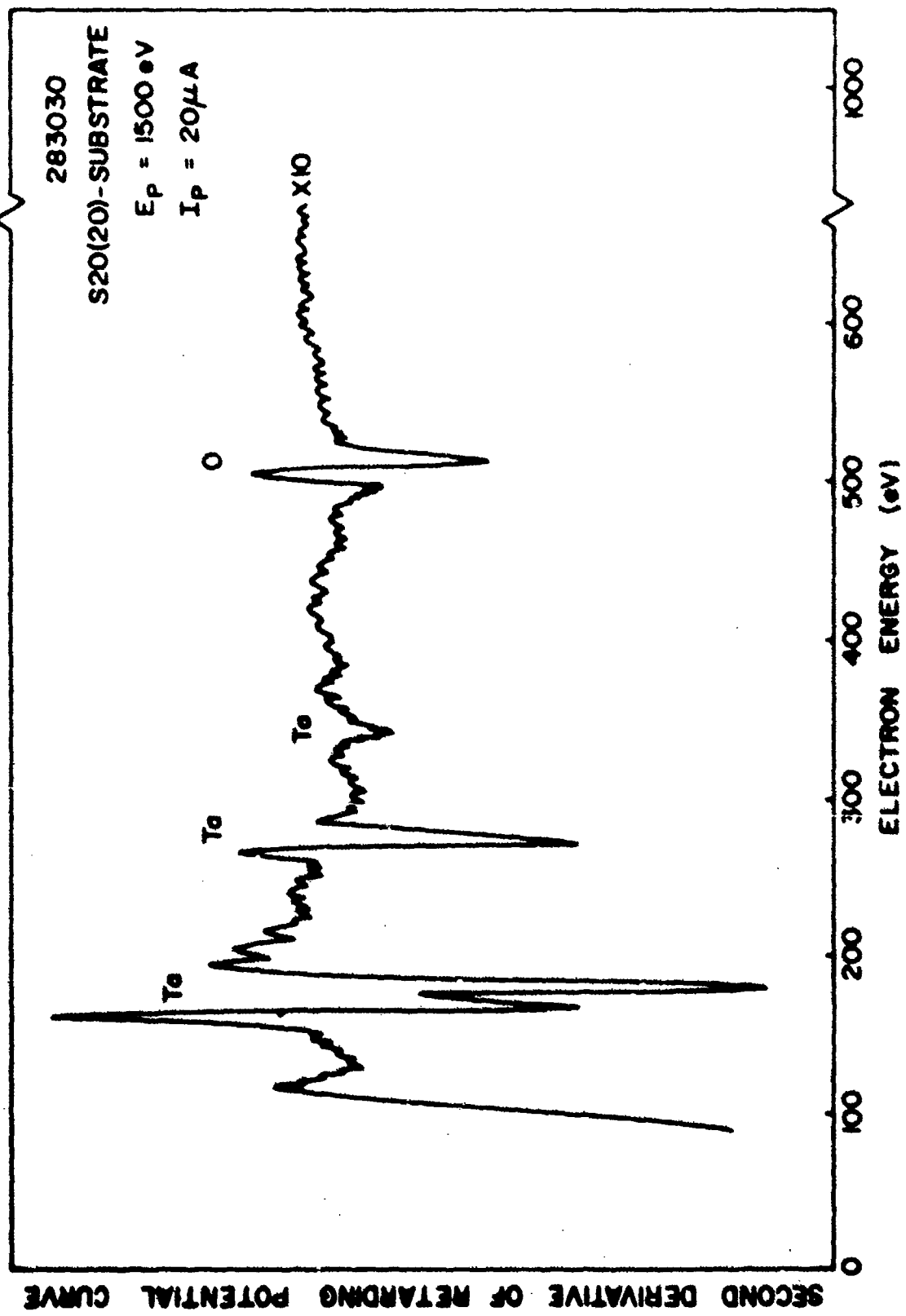


Figure 33 AES results from partially cleaned Ta substrate.

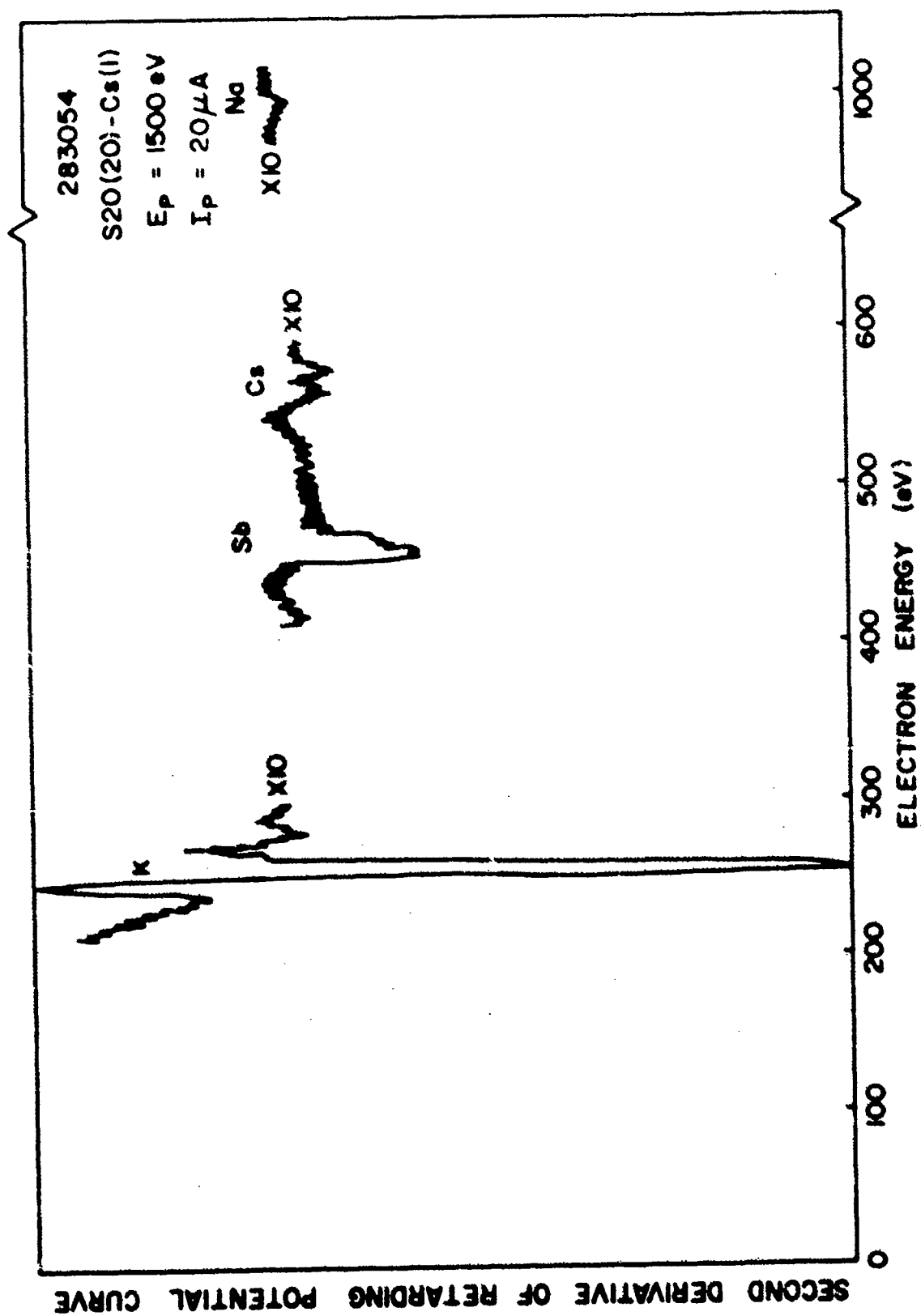


Figure 34 AES results from sample with peak yield of those deposited on a partially cleaned Ta substrate.

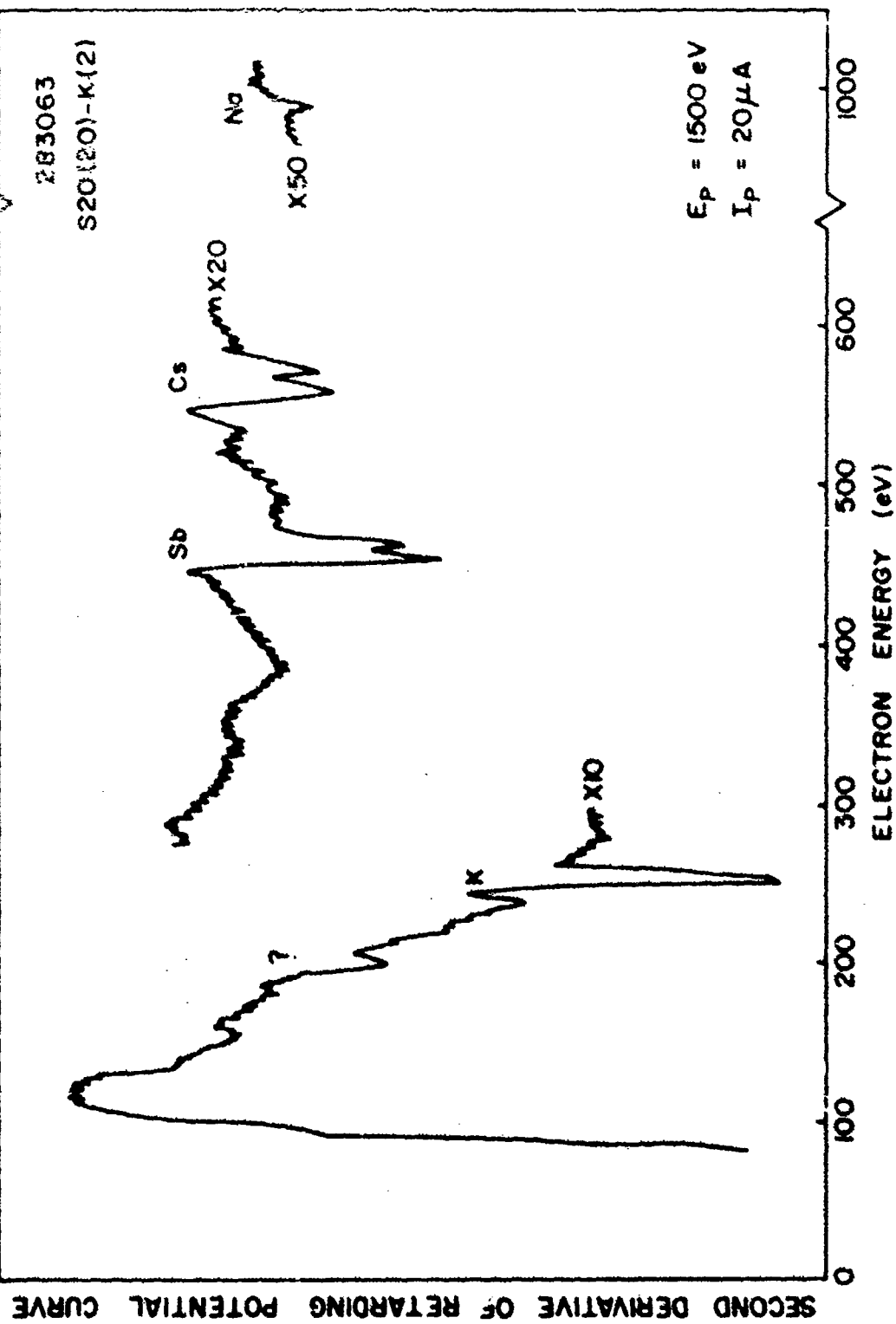


Figure 15 AES results after depositions on sample with peak spectral yield of those formed on a partially cleaned Ta substrate.

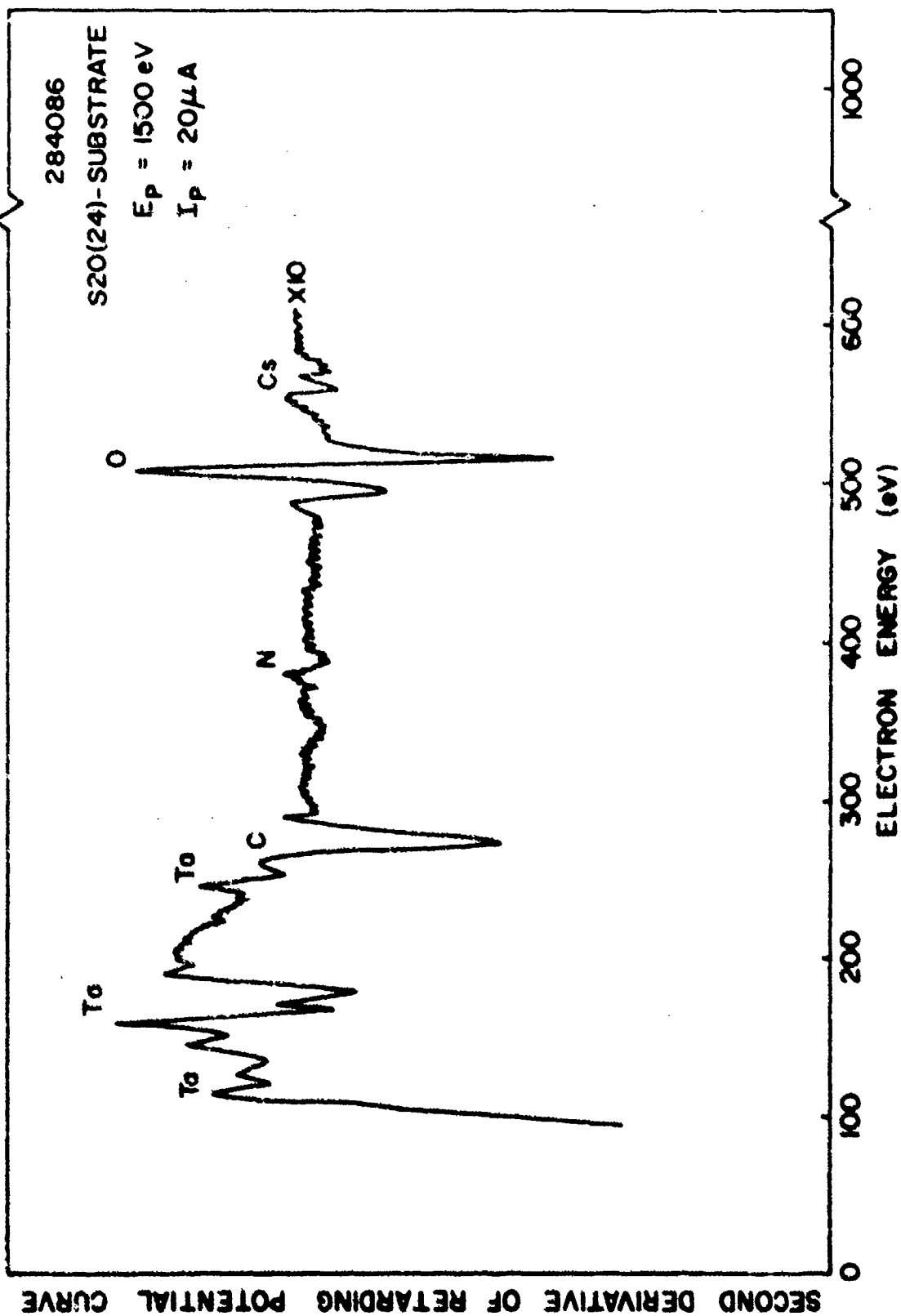


Figure 36 AES results from contaminated Ta substrate.

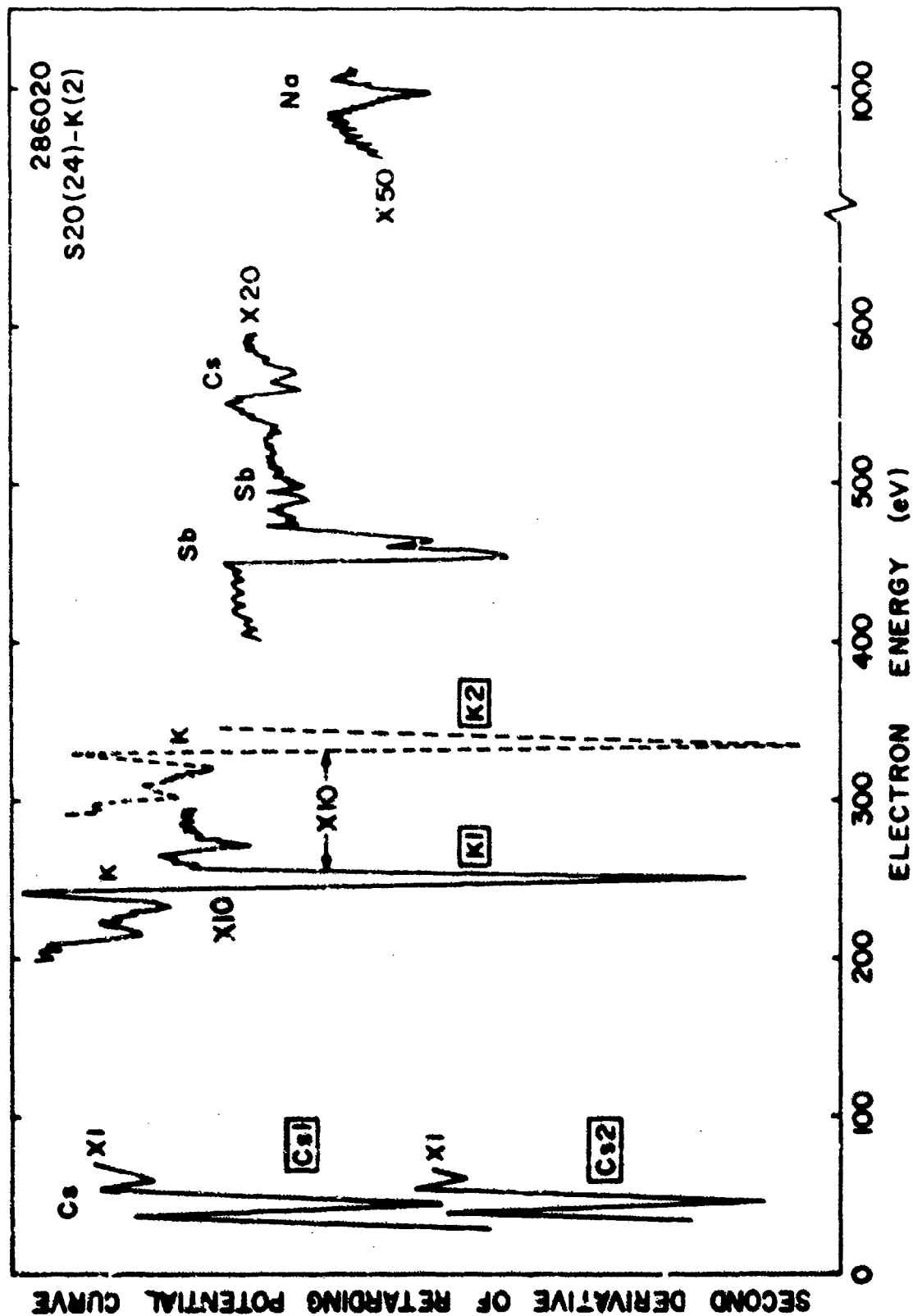


Figure 37 AES results from sample with peak yield of those deposited on a contaminated Ta substrate

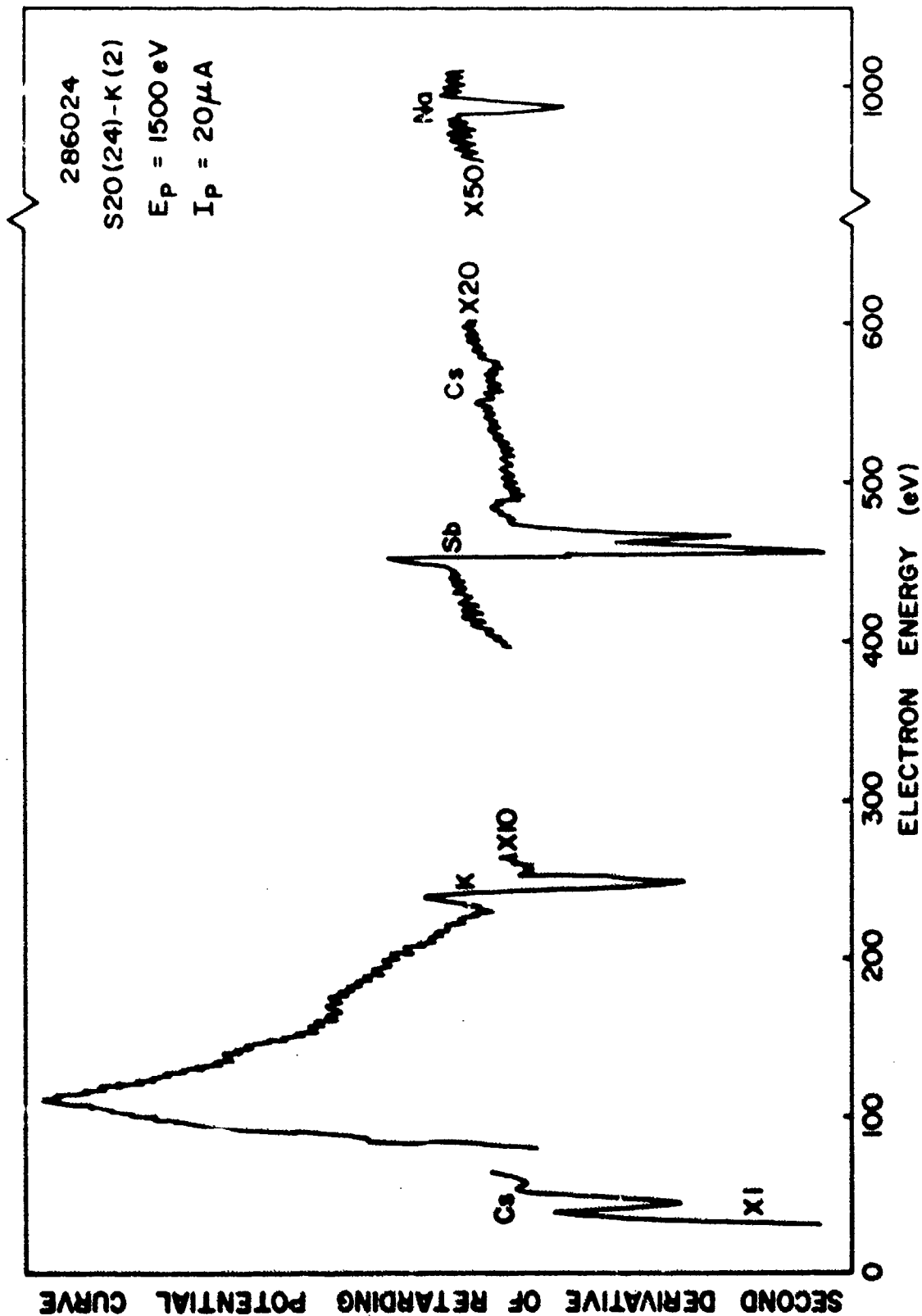


Figure 39 AES results after heating of sample with peak spectral yield of those deposited on a contaminated Ta substrate.

SECOND DERIVATIVE OF RETARDING POTENTIAL CURVE

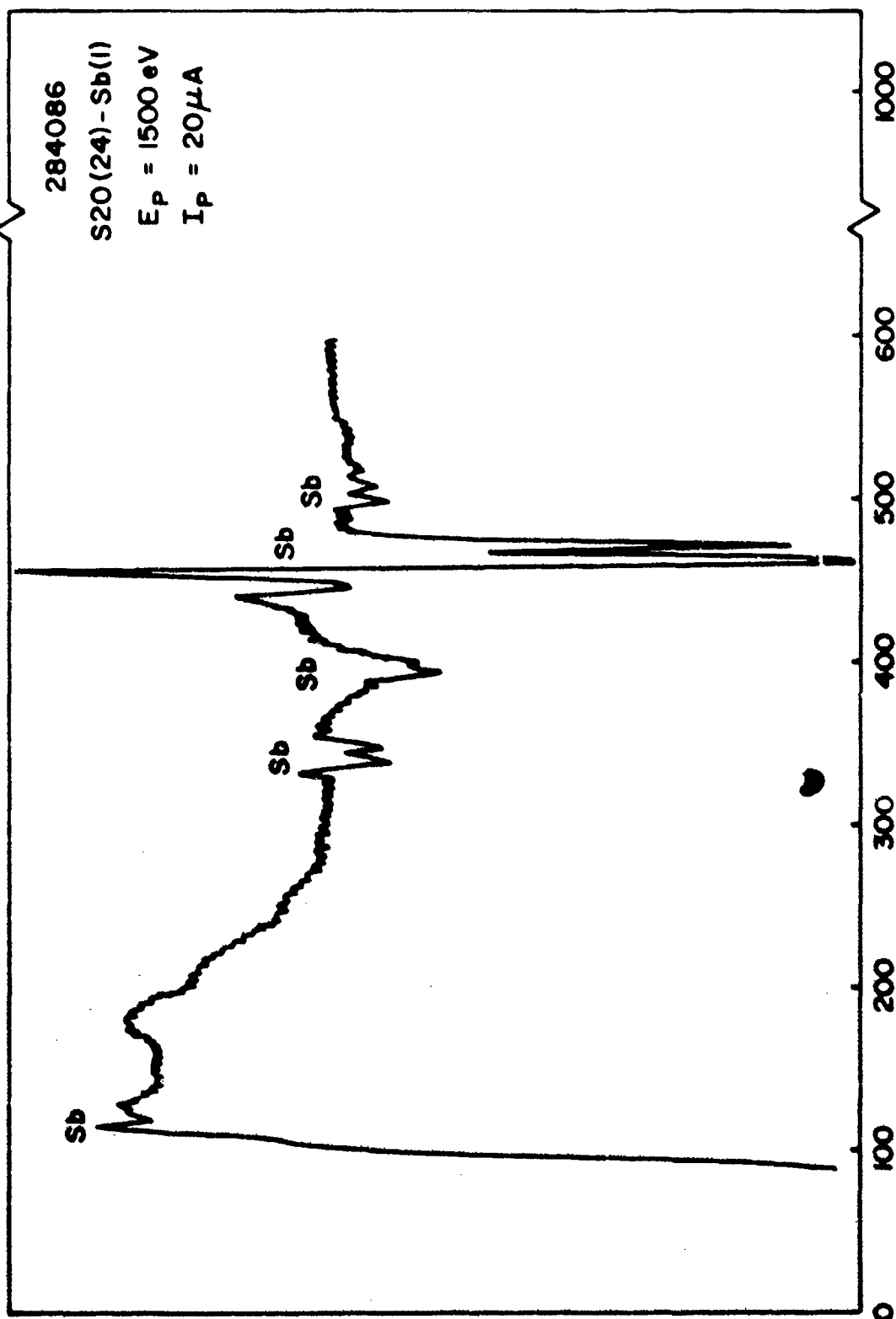


Figure 39 AES results from S20(24)-Sb(1).

Figure 10 AES results from S20 (20) -Sb(1).

SECOND DERIVATIVE OF RETARDING POTENTIAL CURVE

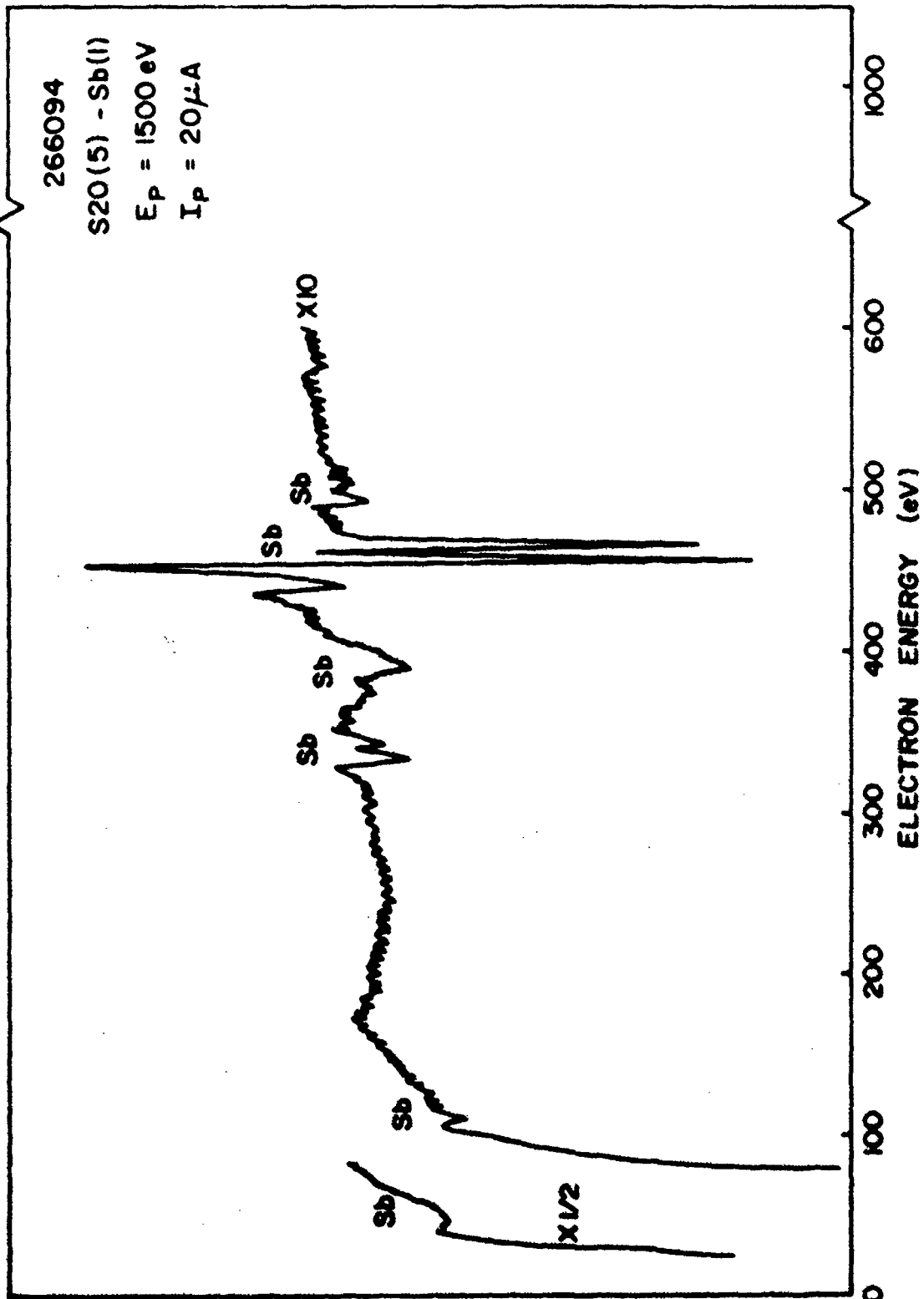


Figure 41 AES results from S20(5)-Sb(1).

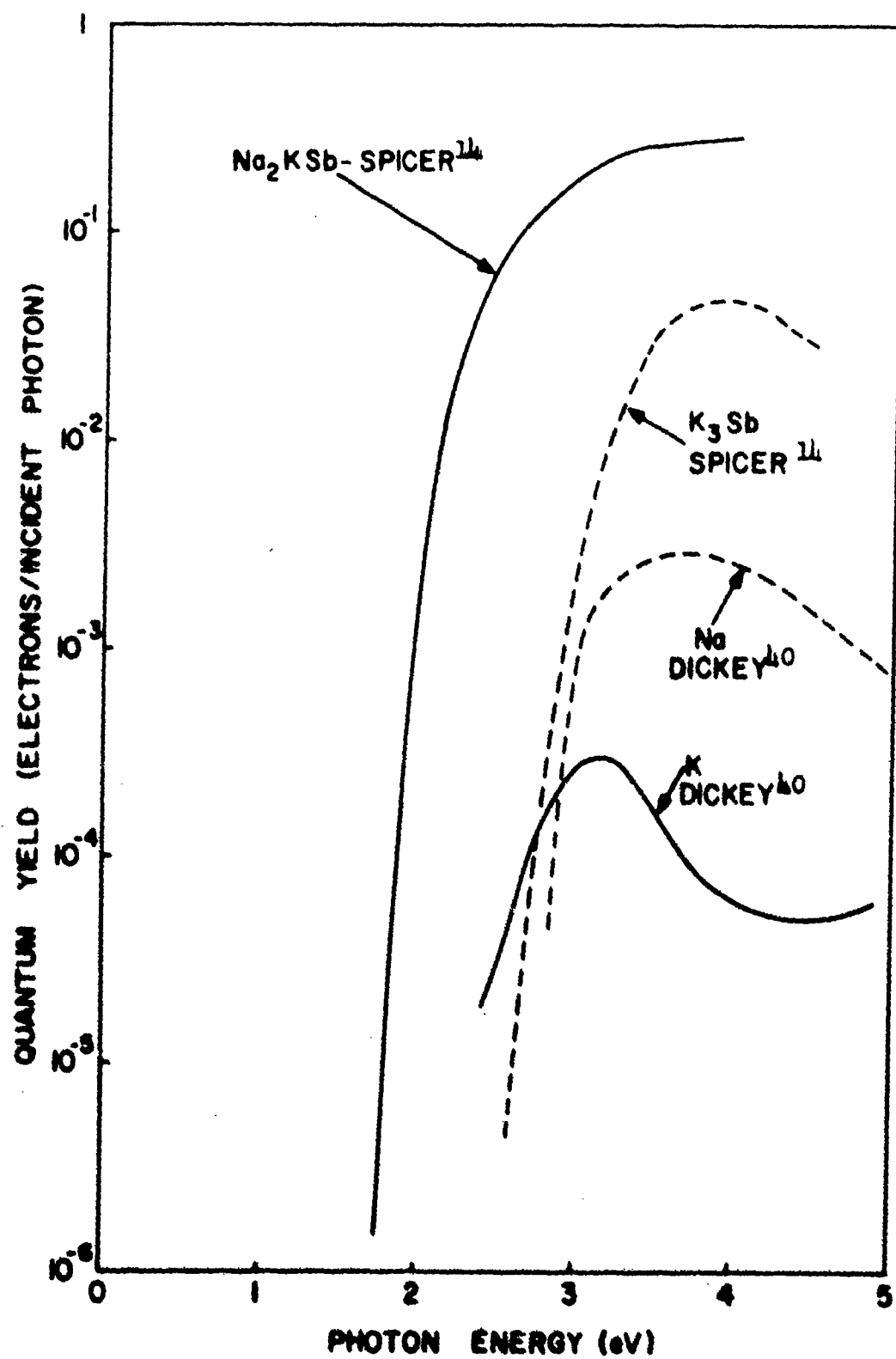


Figure 42 Spectral yield curves for K, Na, K_3Sb and Na_2KSb .

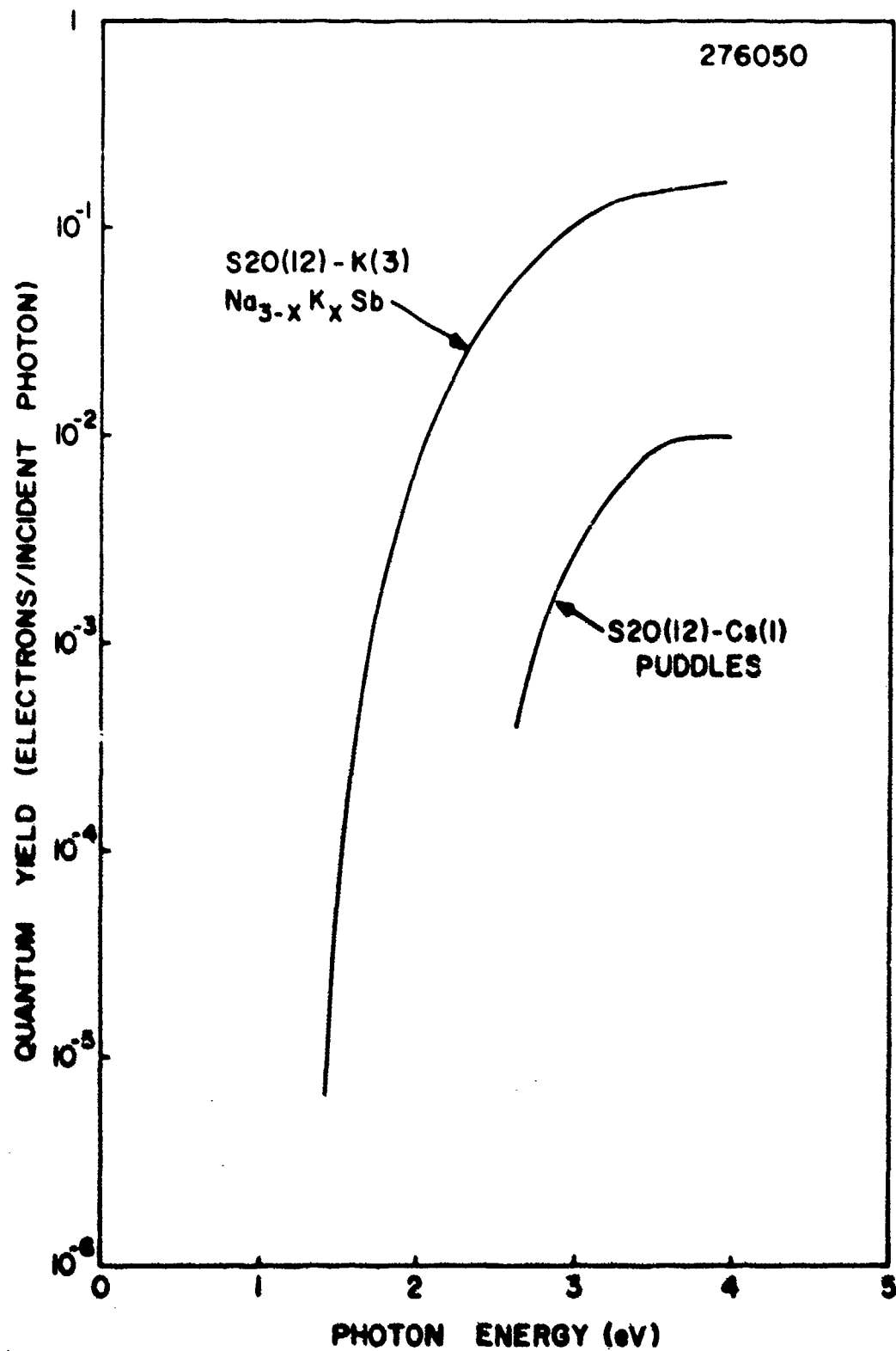


Figure 43 Change in spectral yield with excessive Cs deposition.

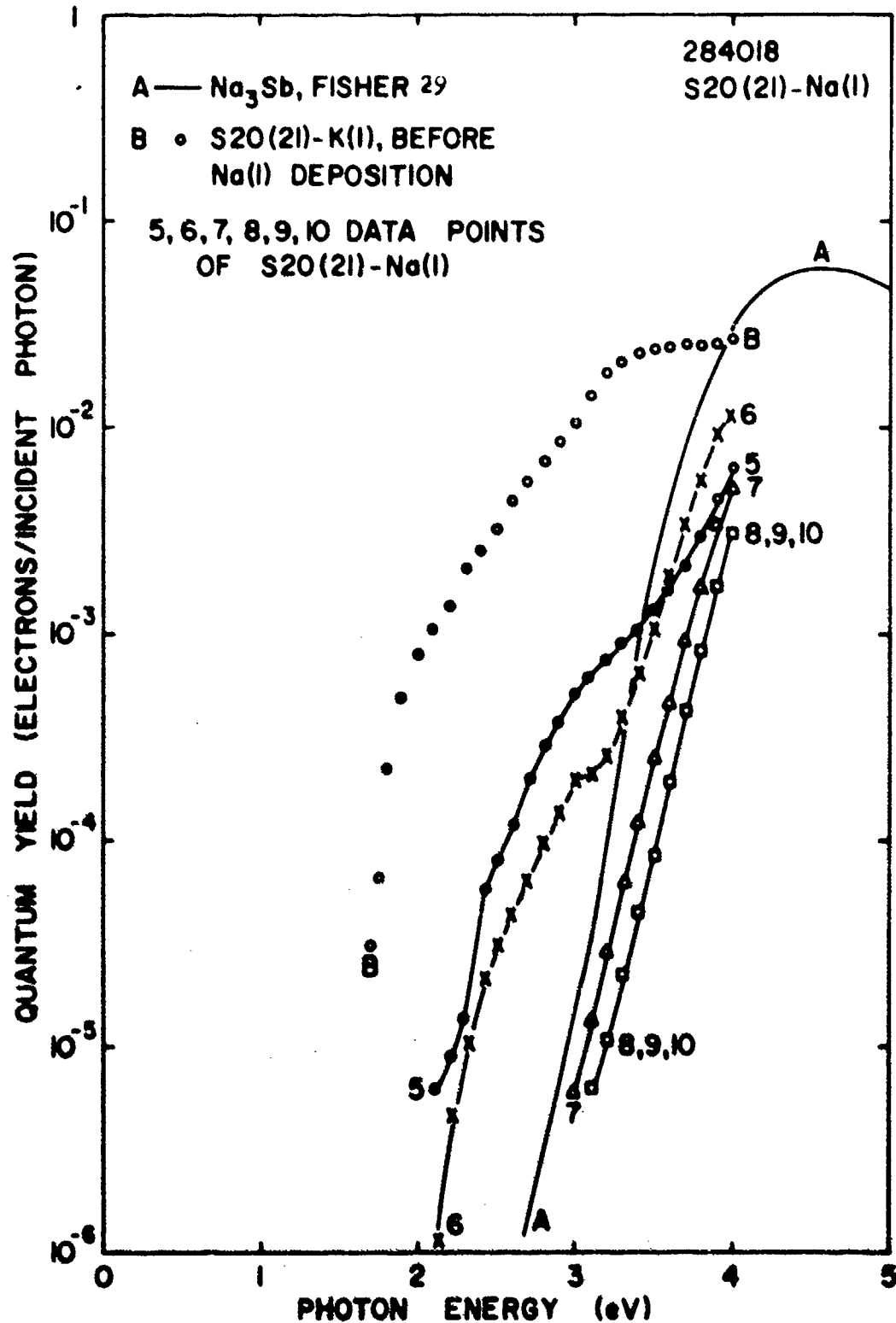


Figure 44 Changes in spectral yield of S20(21) due to Na(I) deposition and subsequent heating.

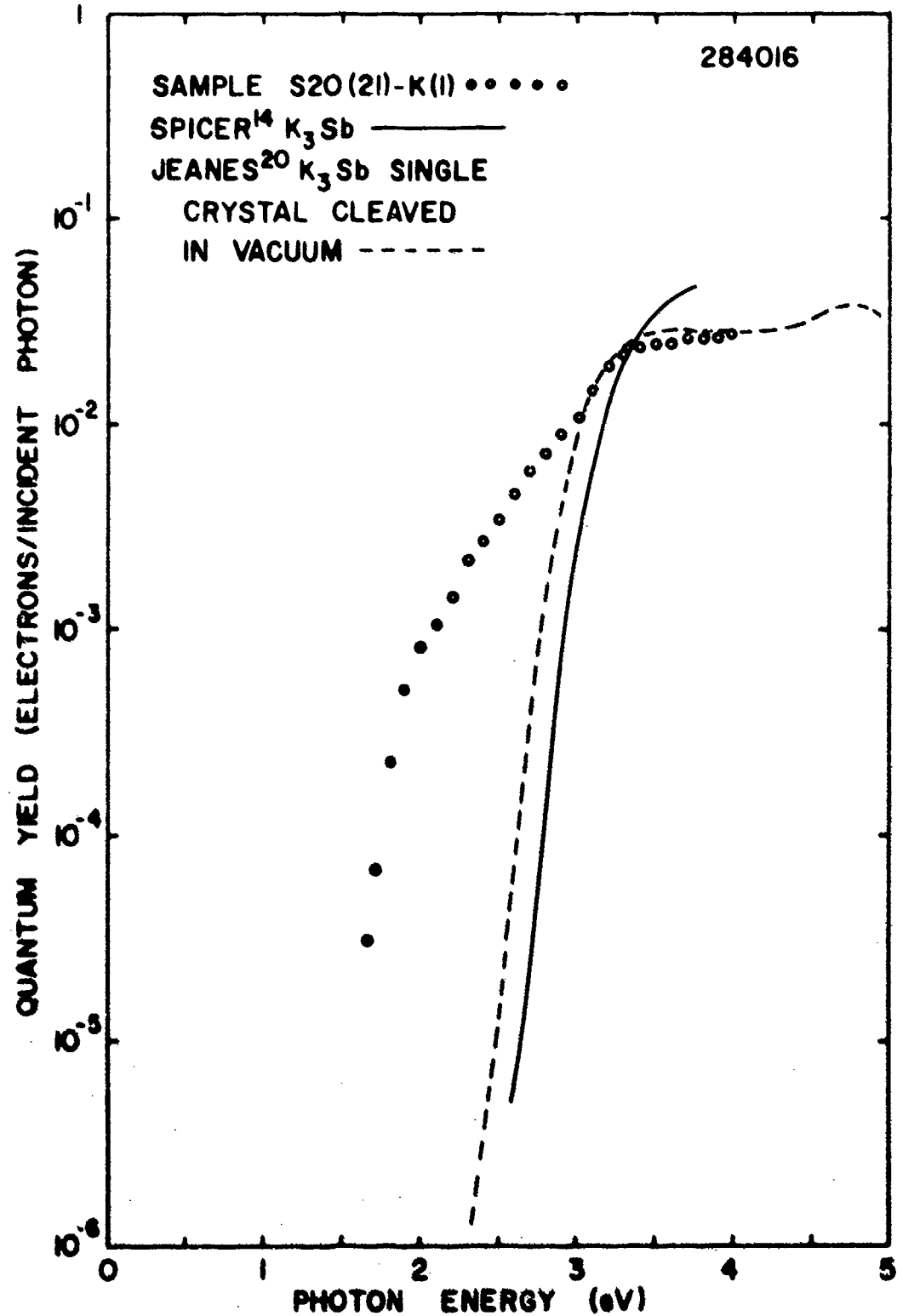


Figure 45 Spectral yield results of S20(21)-K(1) and those of K₃Sb reported by Spicer and Jeanes.

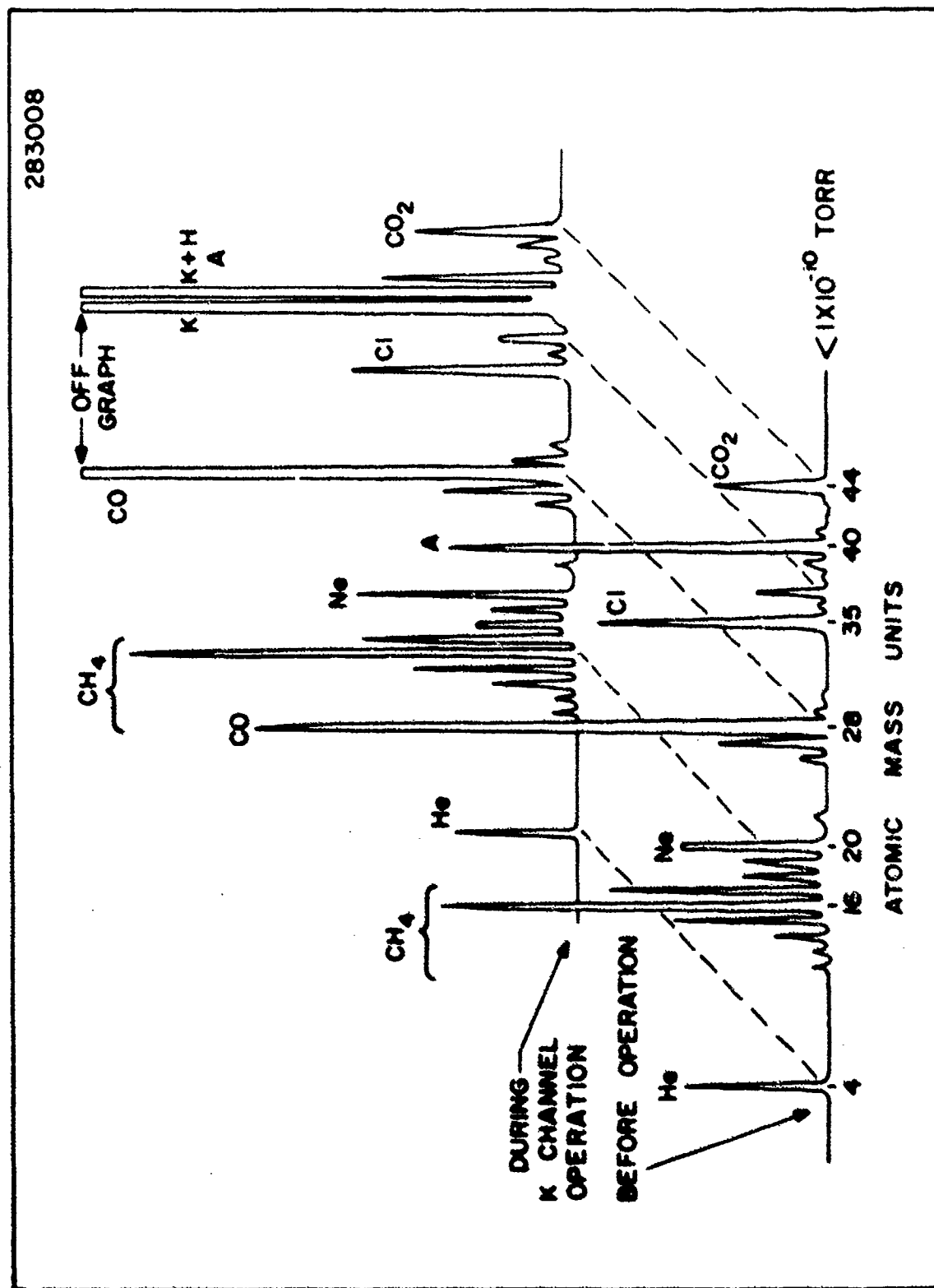


Figure 46 Residual gas analyzer data from K channel operation.

273004
S20(8)-Na(I)

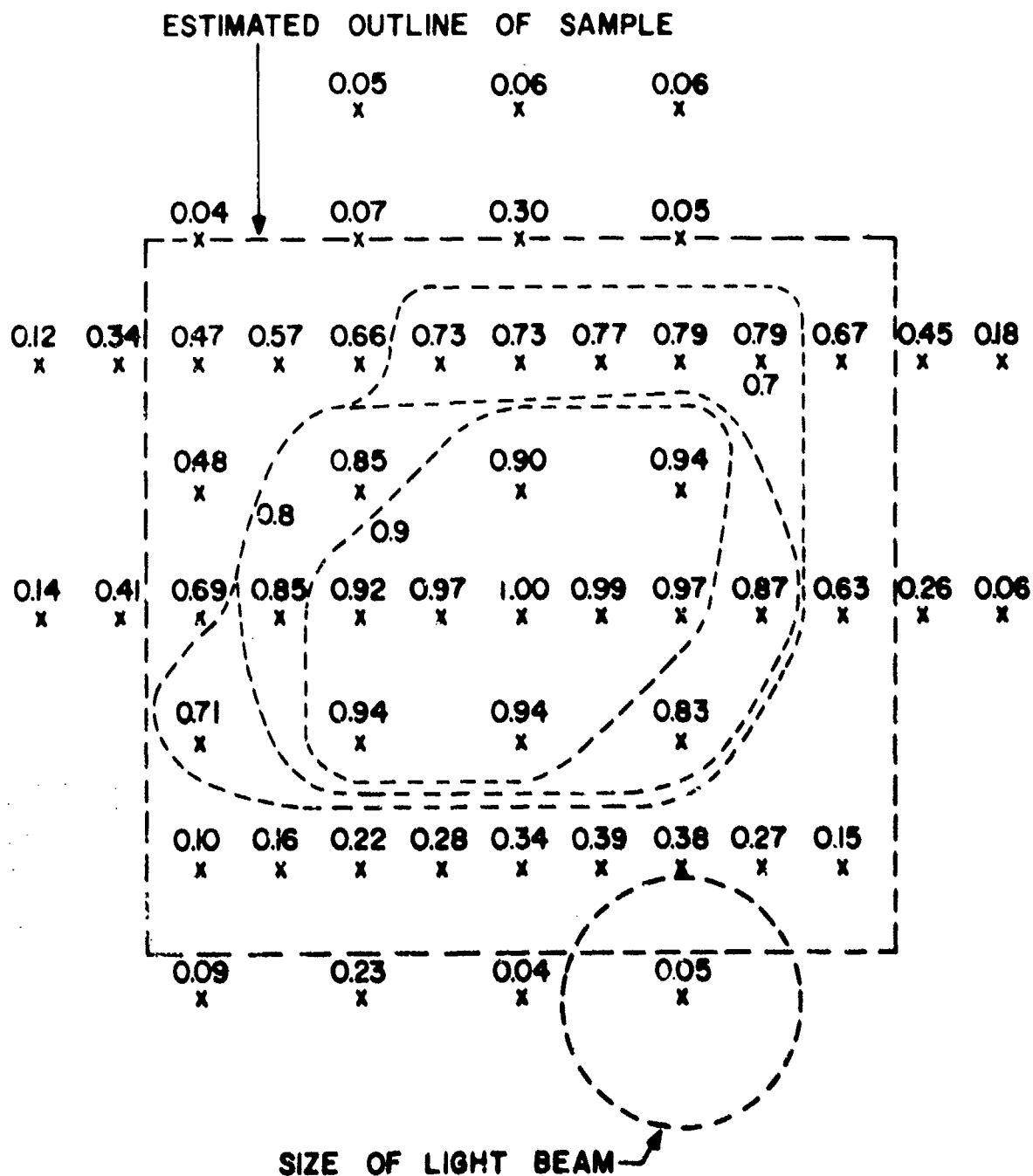


Figure 48 Map of relative quantum yield of S20(8)-Na(I).

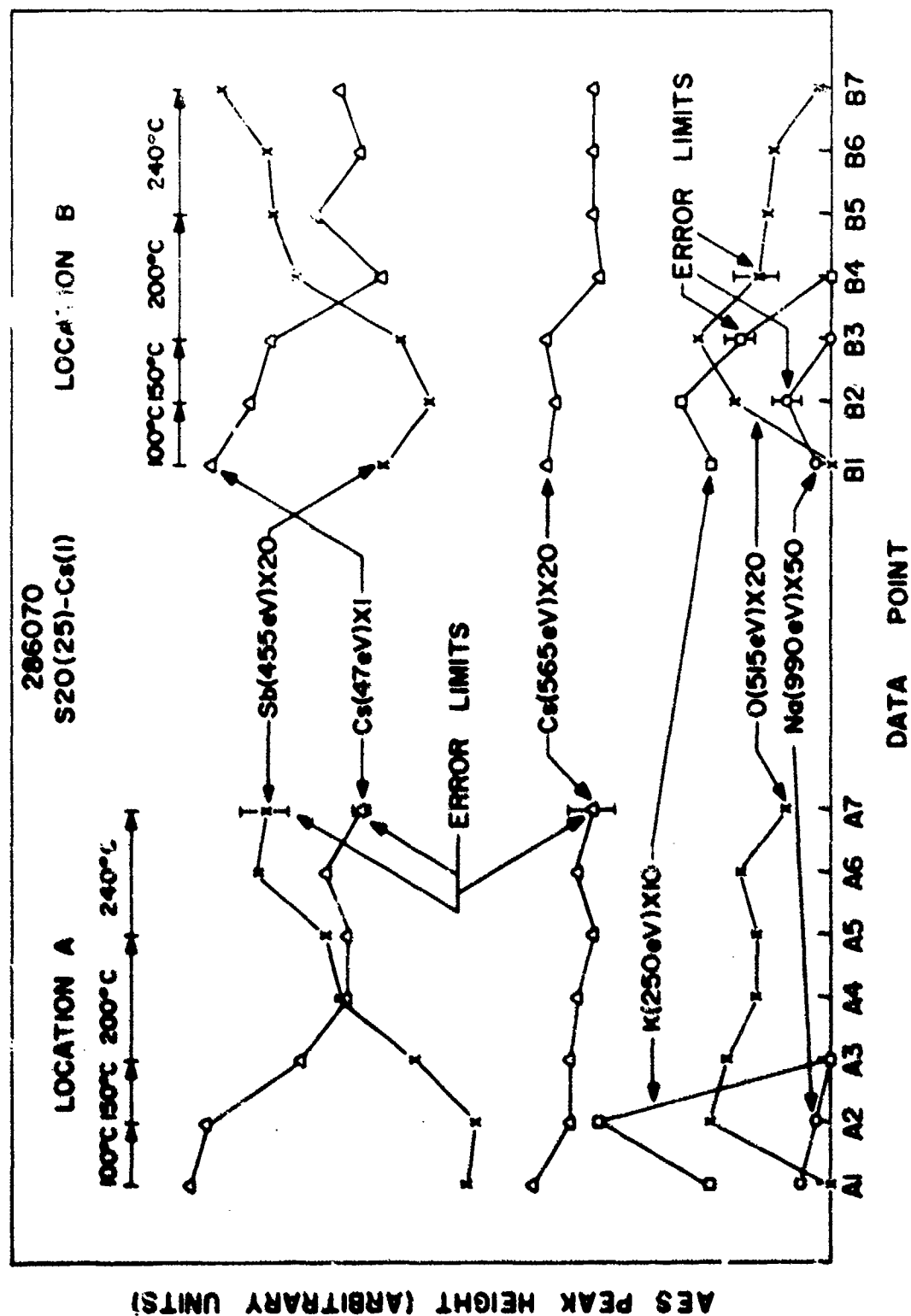


Figure 49 Summation of AES peak height changes from two locations on S20(25)-Cs(1).

Data Point	Event Preceding Data Point		
A1	Cs DEPOSITION		
A2	Heating	100°C	(19:50) (Hrs:Min)
A3	Heating	150°C	(20:40)
A4	Heating	200°C	(23:30)
A5	Heating	200°C	(17:40)
A6	Heating	240°C	(17:55)
A7	Heating	240°C	(19:25)
B1	Cs DESPOSITION		
B2	Heating	100°C	(19:50)
B3	Heating	150°C	(20:40)
B4	Heating	200°C	(23:30)
B5	Heating	200°C	(17:40)
B6	Heating	240°C	(17:55)
B7	Heating	240°C	(19:35)

Figure 50 Schedule of heating temperatures and duration of heating periods for S20(25)-Cs(1).

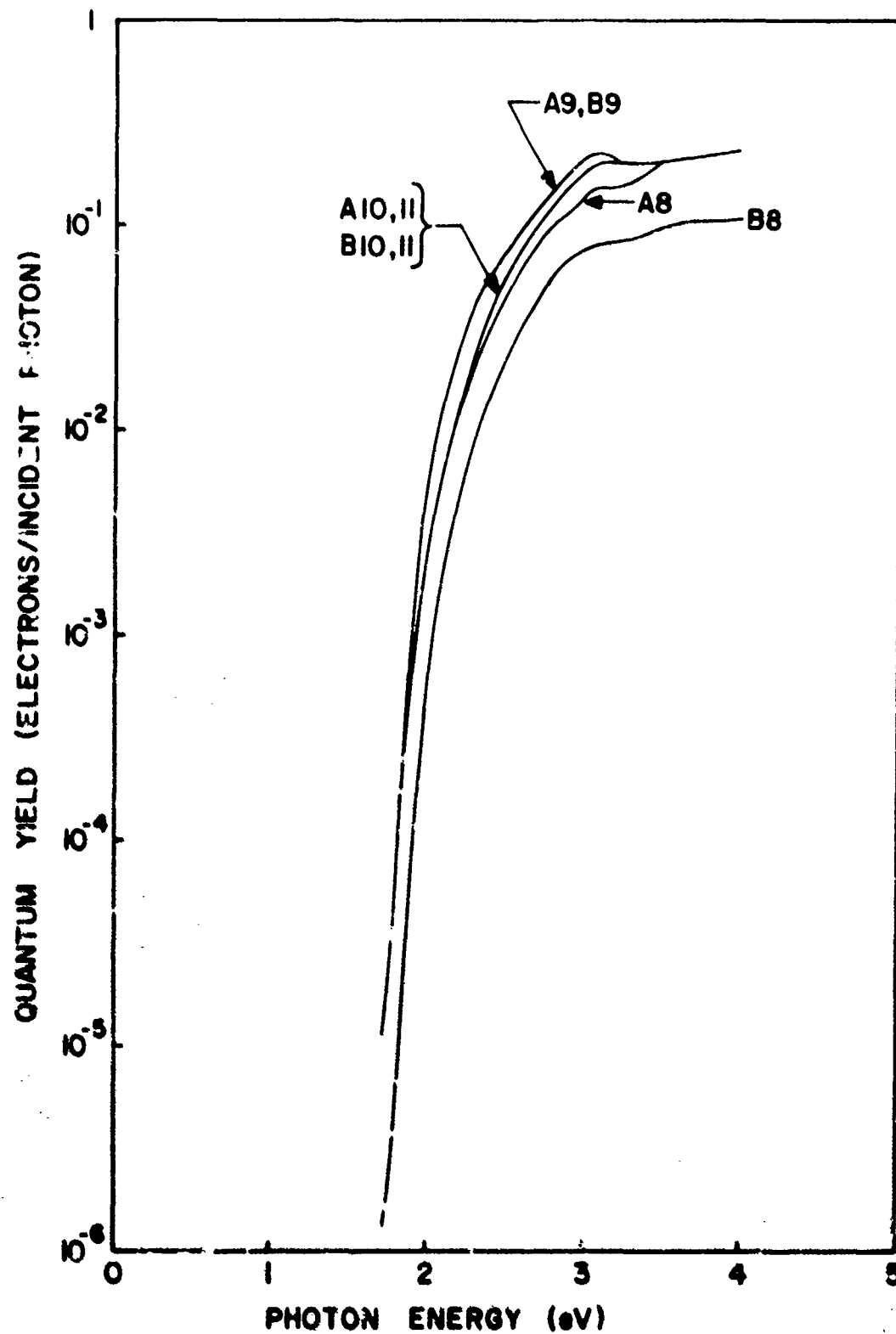


Figure 51 Spectral yield results from two locations on S20(25)-Cs(1).

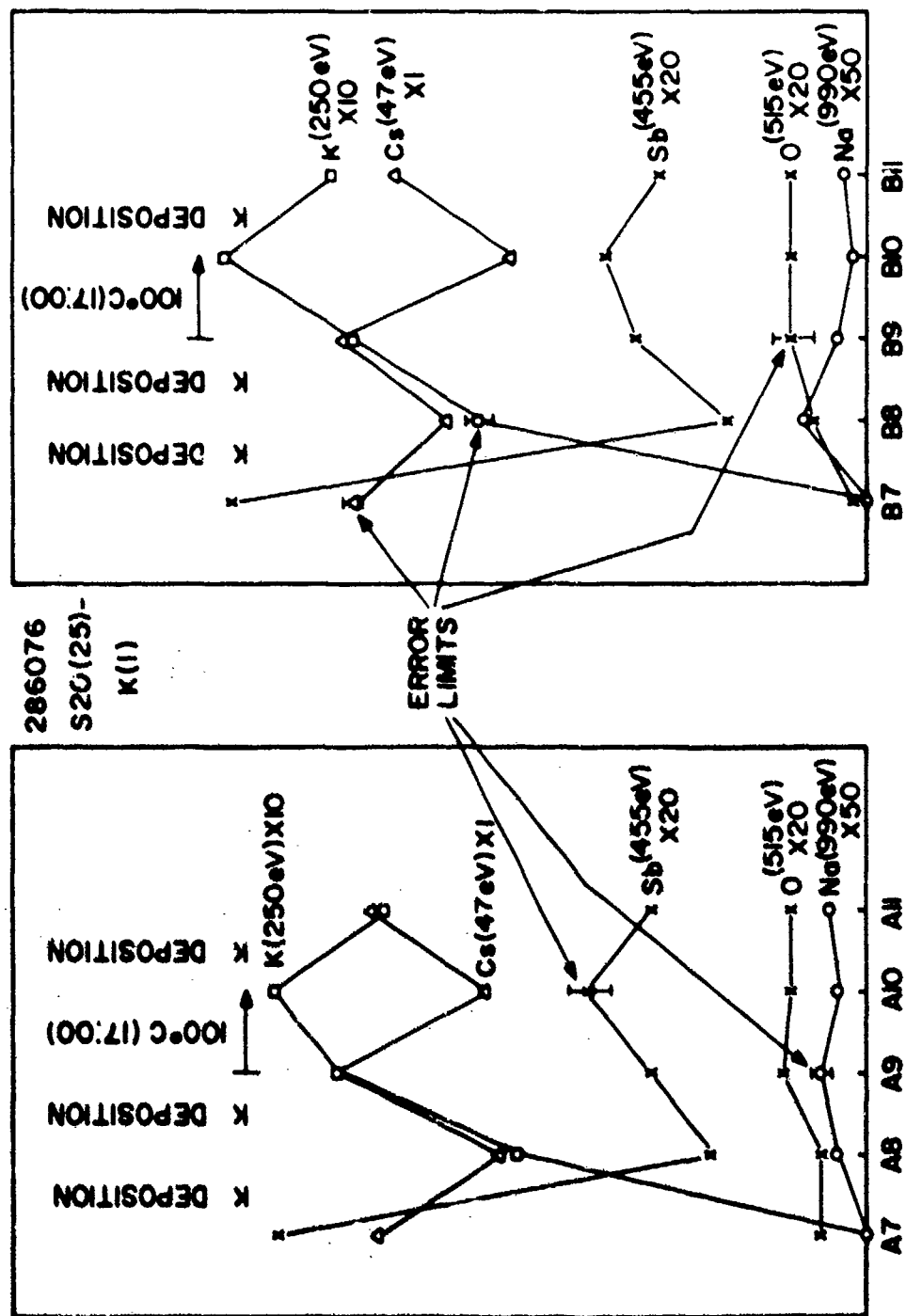


Figure 52 Summation of AES peak height changes from two locations on S20(25)-K(1).

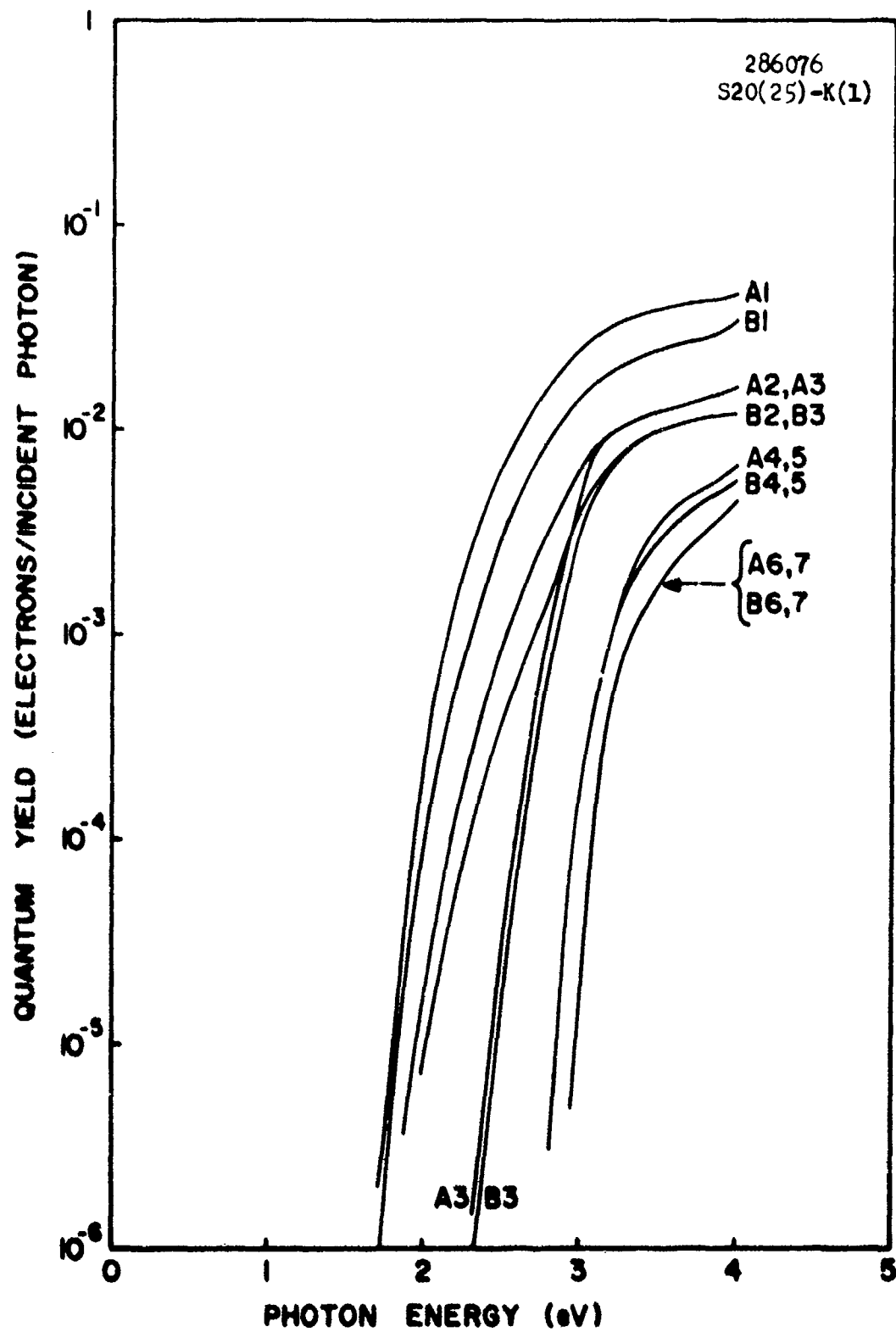


Figure 53 Spectral yield results from two locations
on S20(25) - K(1)

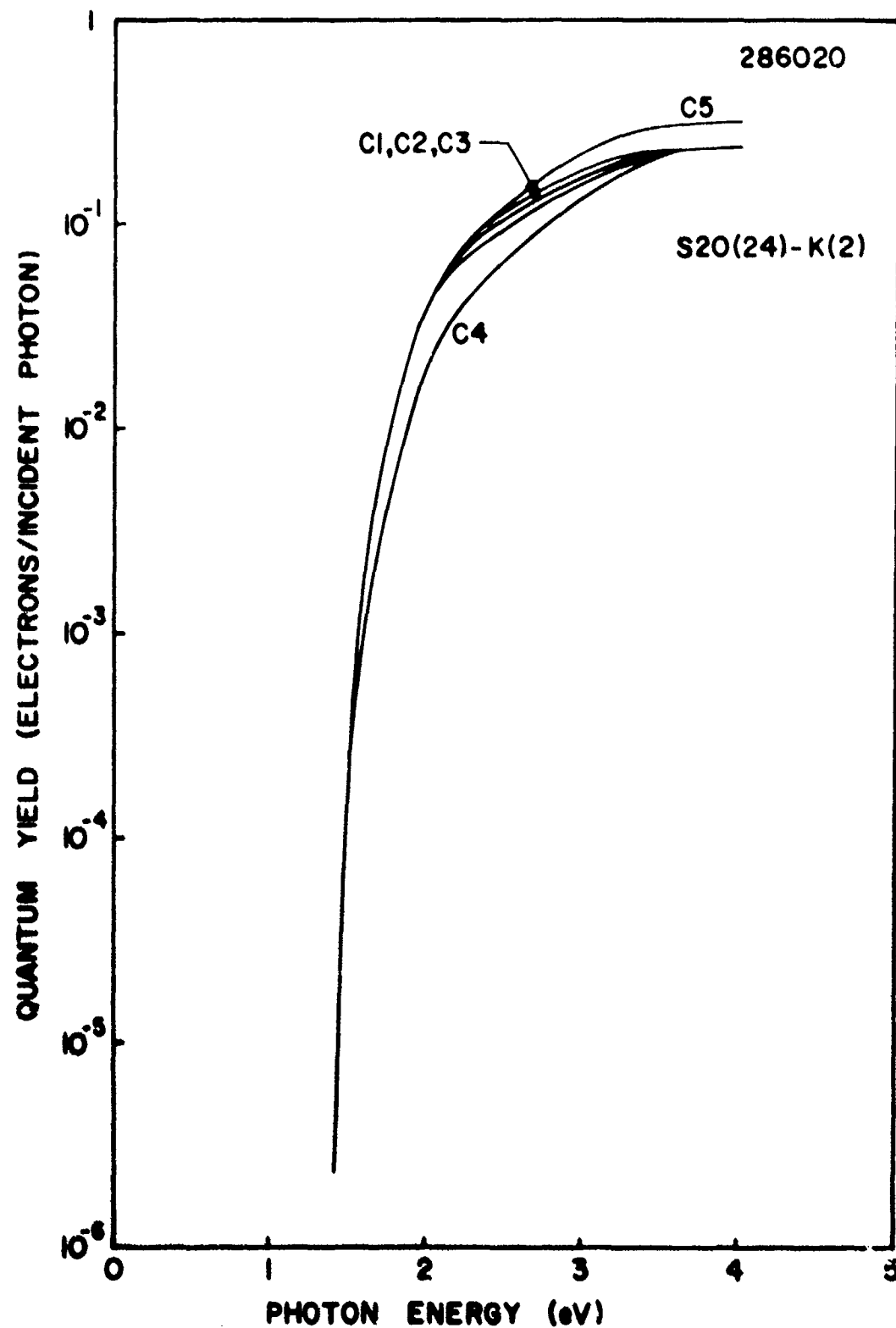


Figure 54 Spectral yield results from five locations on S20(24)-K(2).

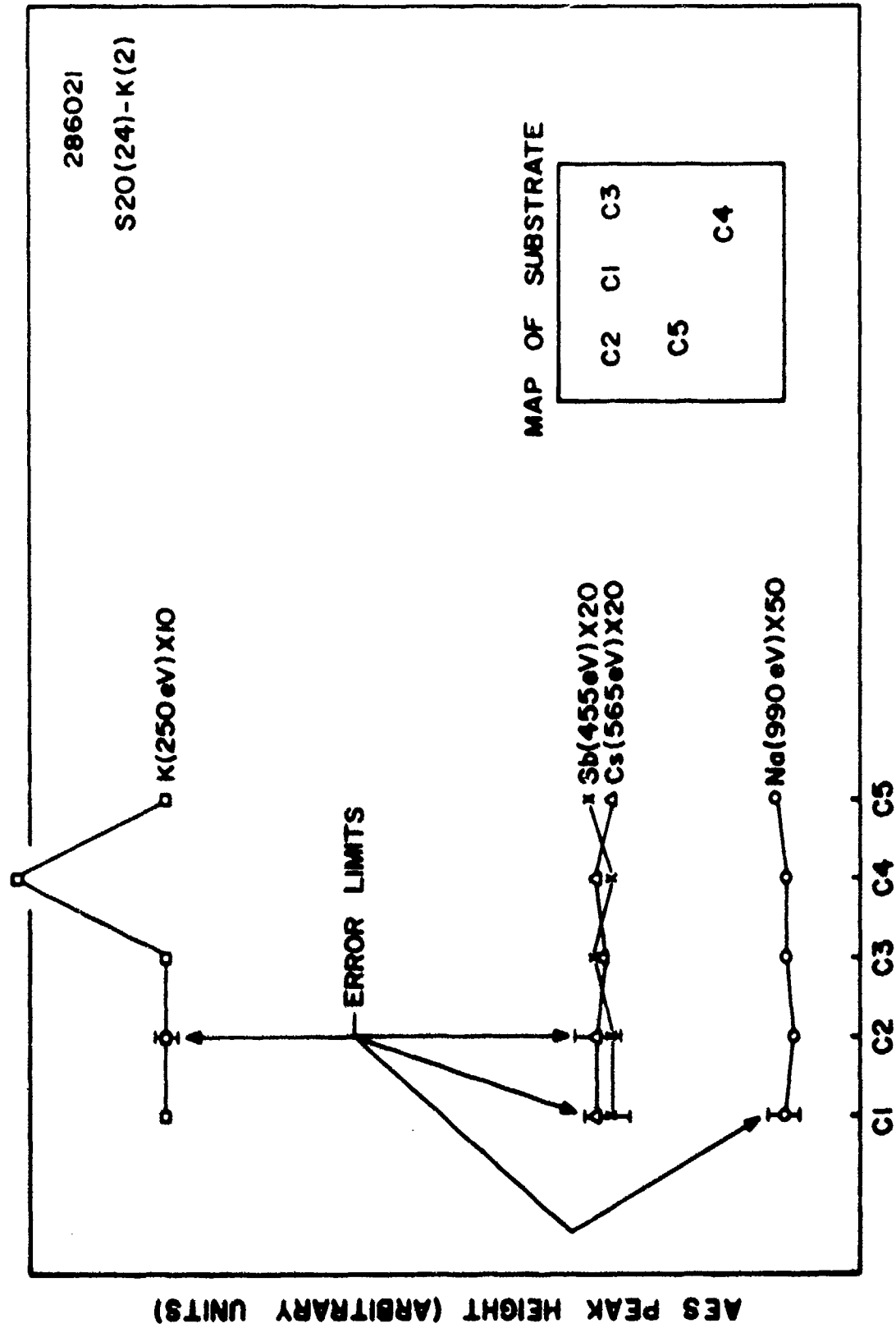


Figure 55 Summation of AES results from 5 locations on S20(24)-K(2).

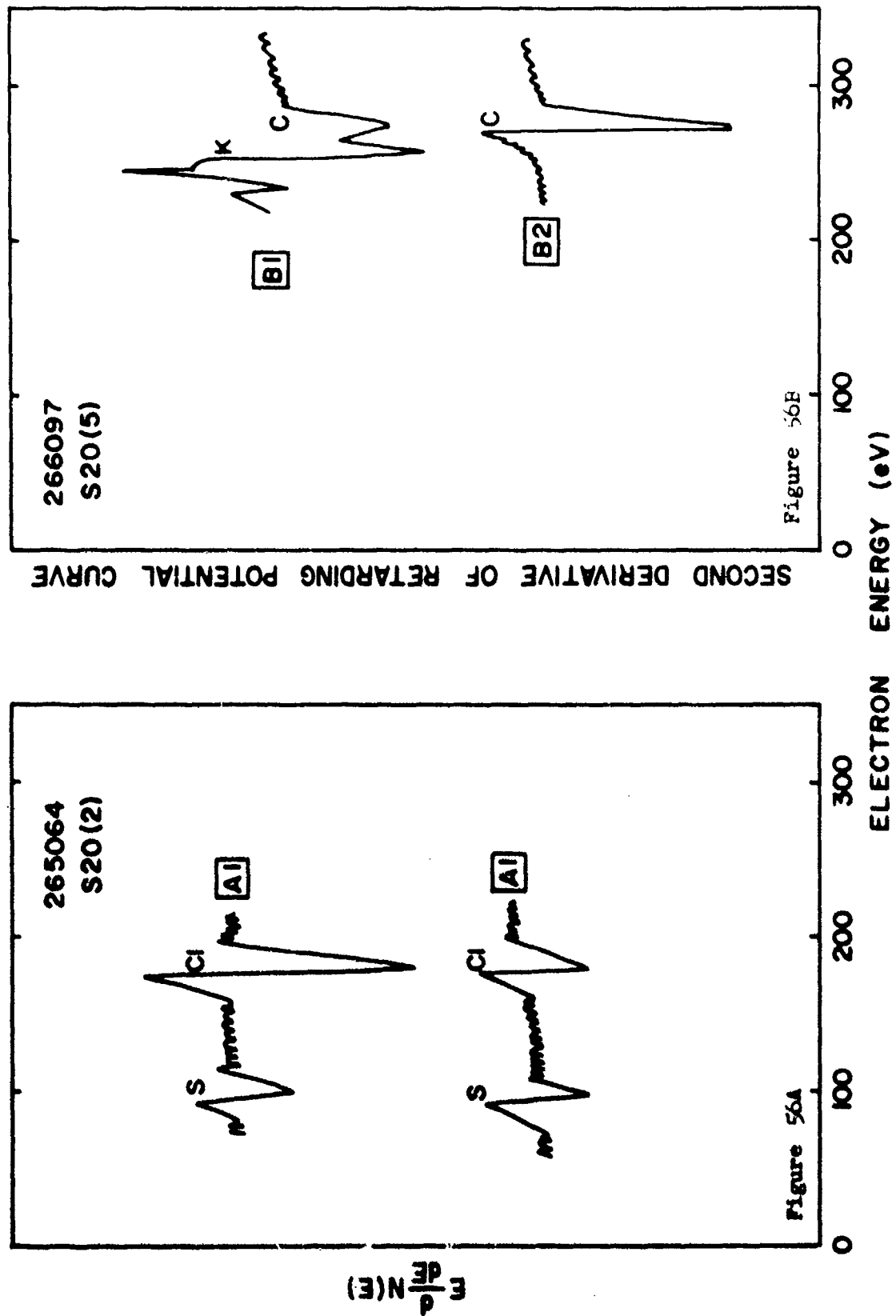


Figure 56 Changes in AES peaks due to electron bombardment.

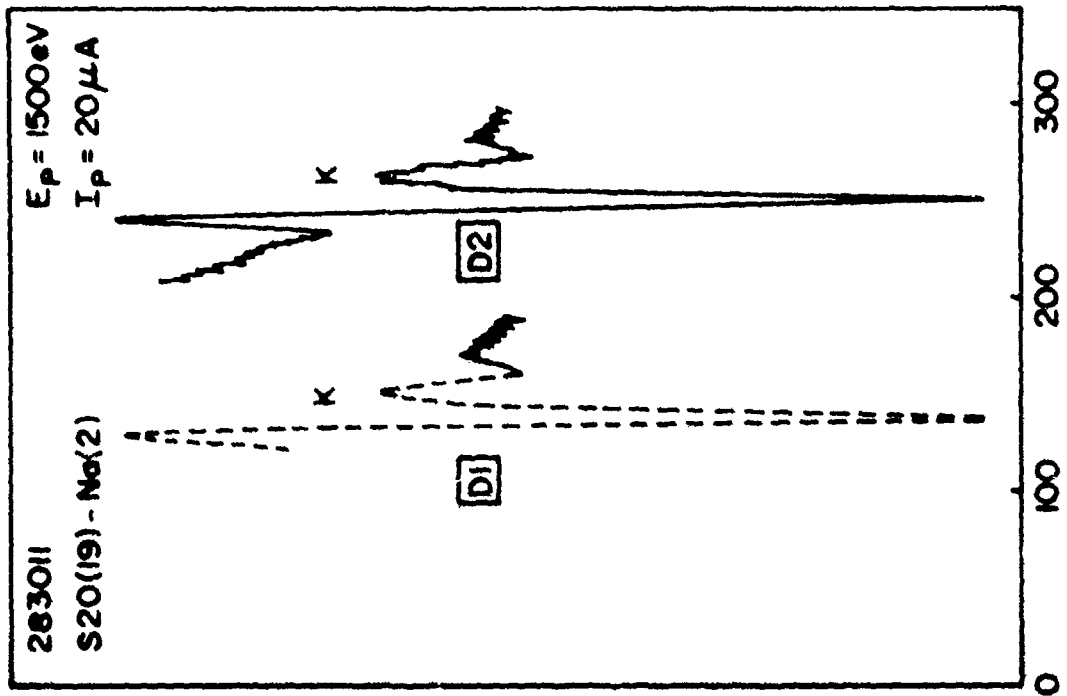


Figure 57A Change in K AES peak under electron bombardment.

SECOND DERIVATIVE OF RETARDING POTENTIAL CURVE

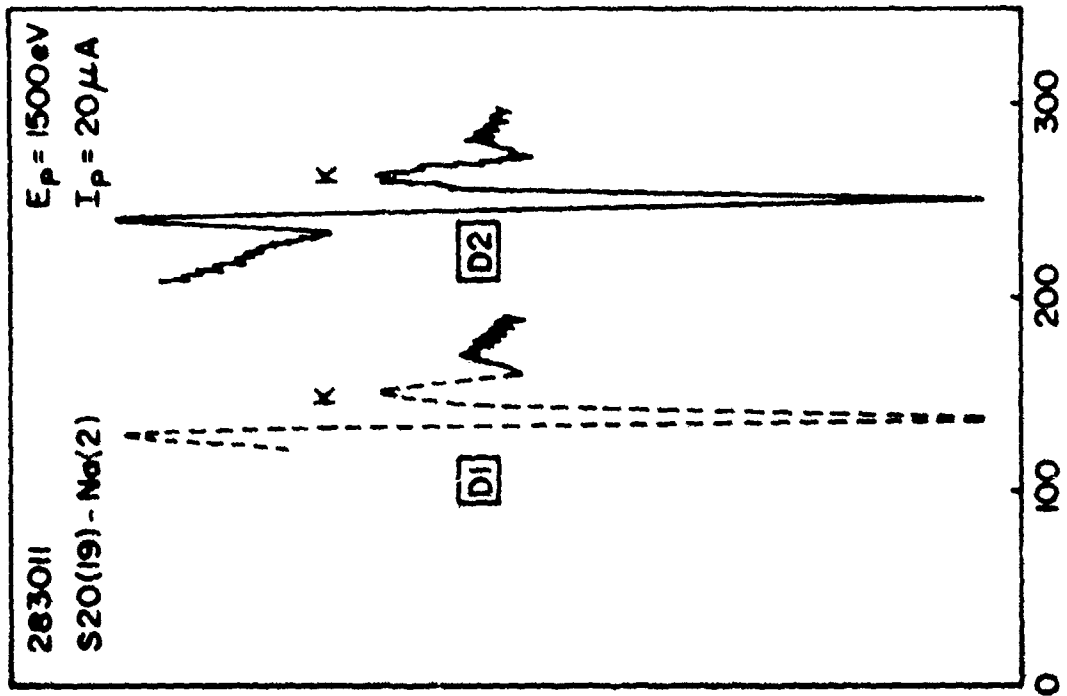


Figure 57B Stability of K AES peak under electron bombardment.

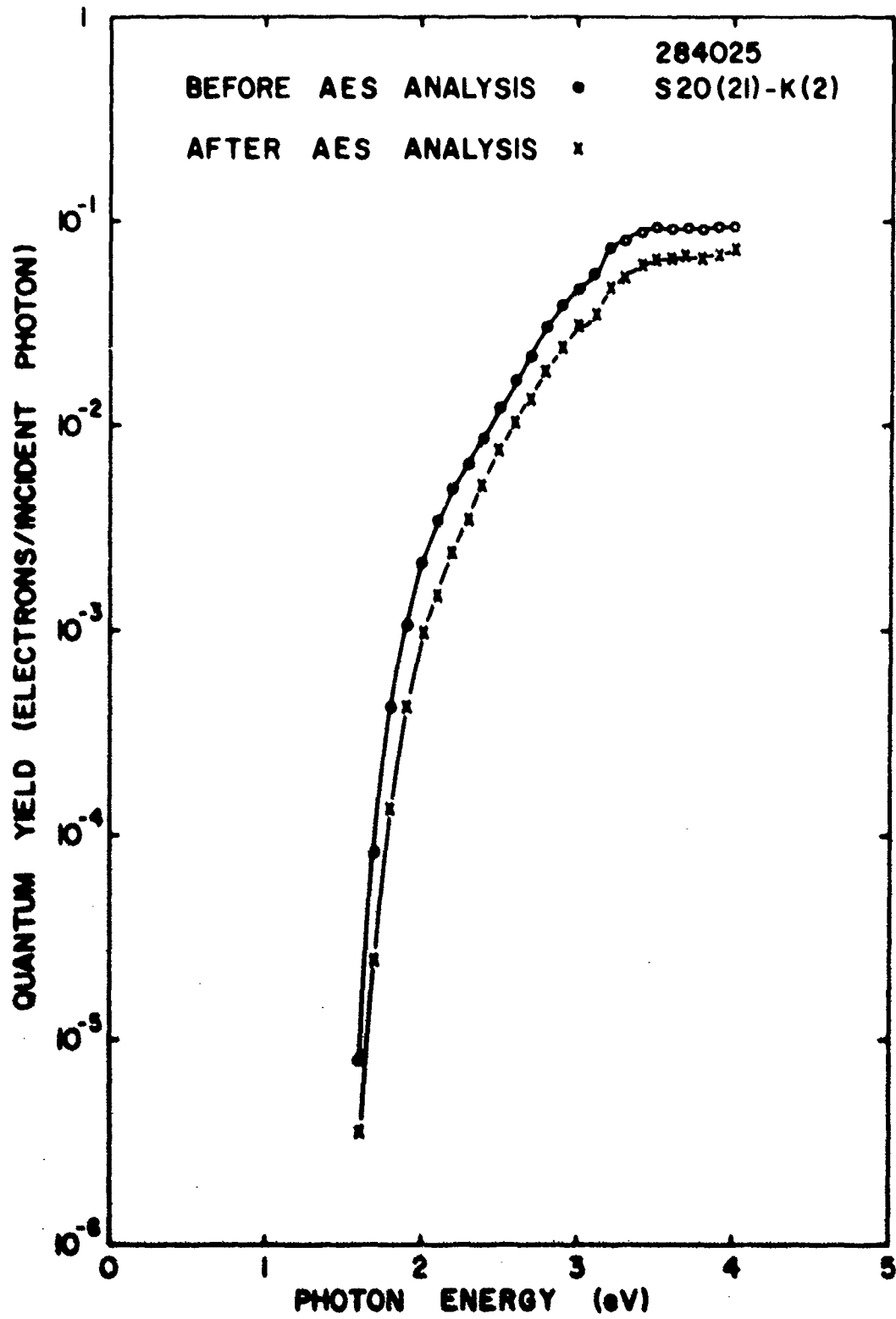


Figure 58 Spectral yield changes due to electron bombardment of S20(21)-K(2).

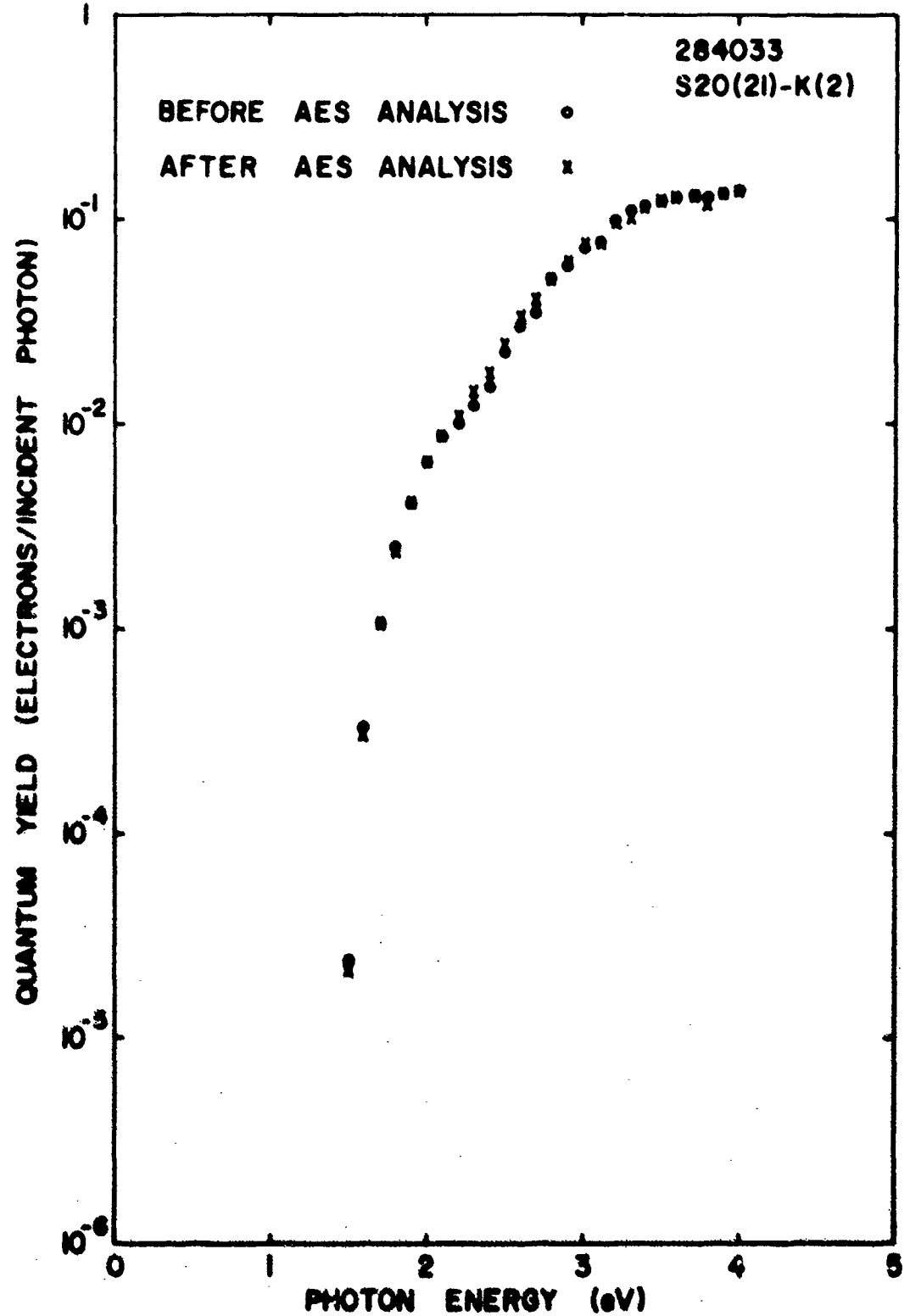


Figure 59 Stability of spectral yield of S20(21)-K(2) under electron bombardment.

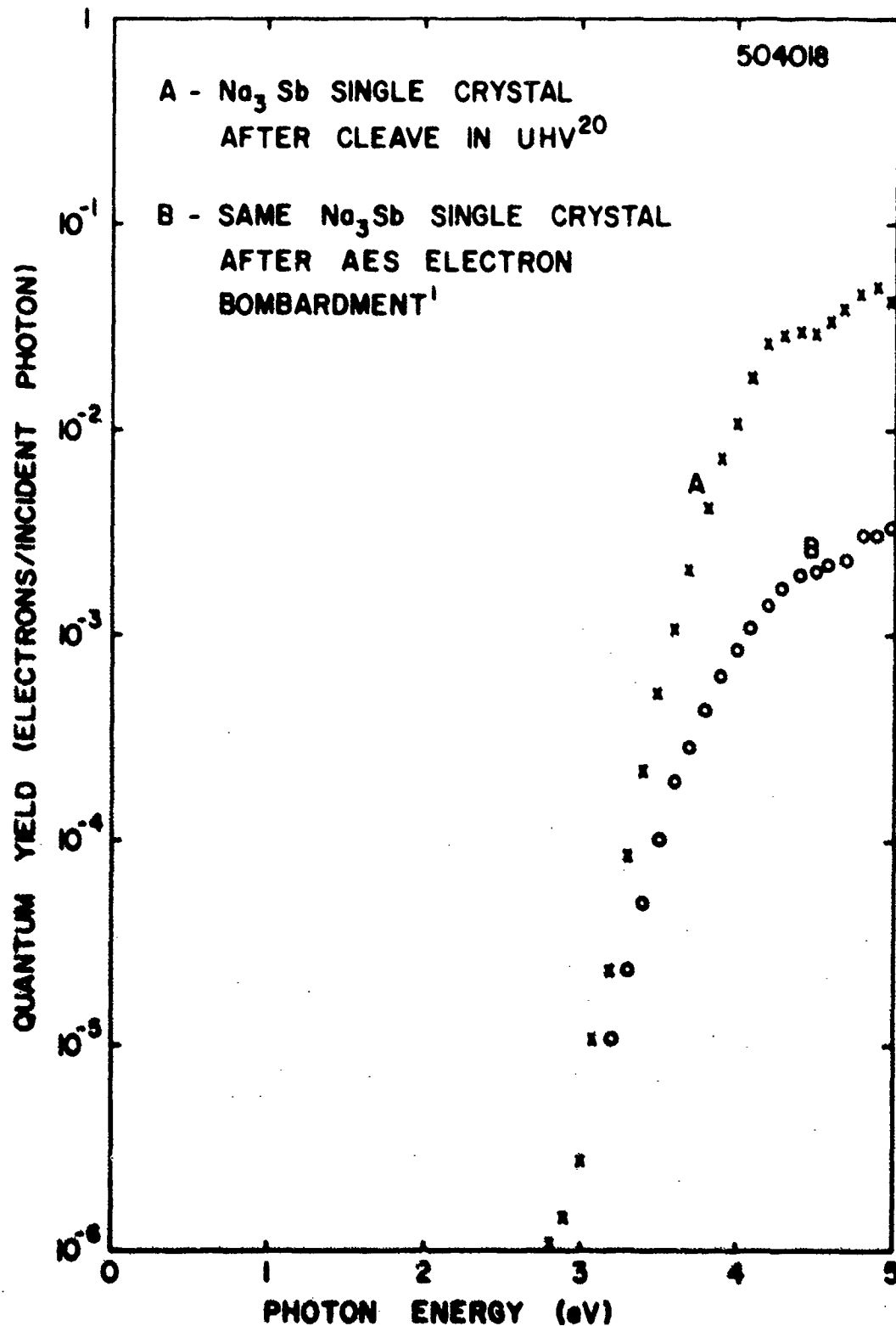
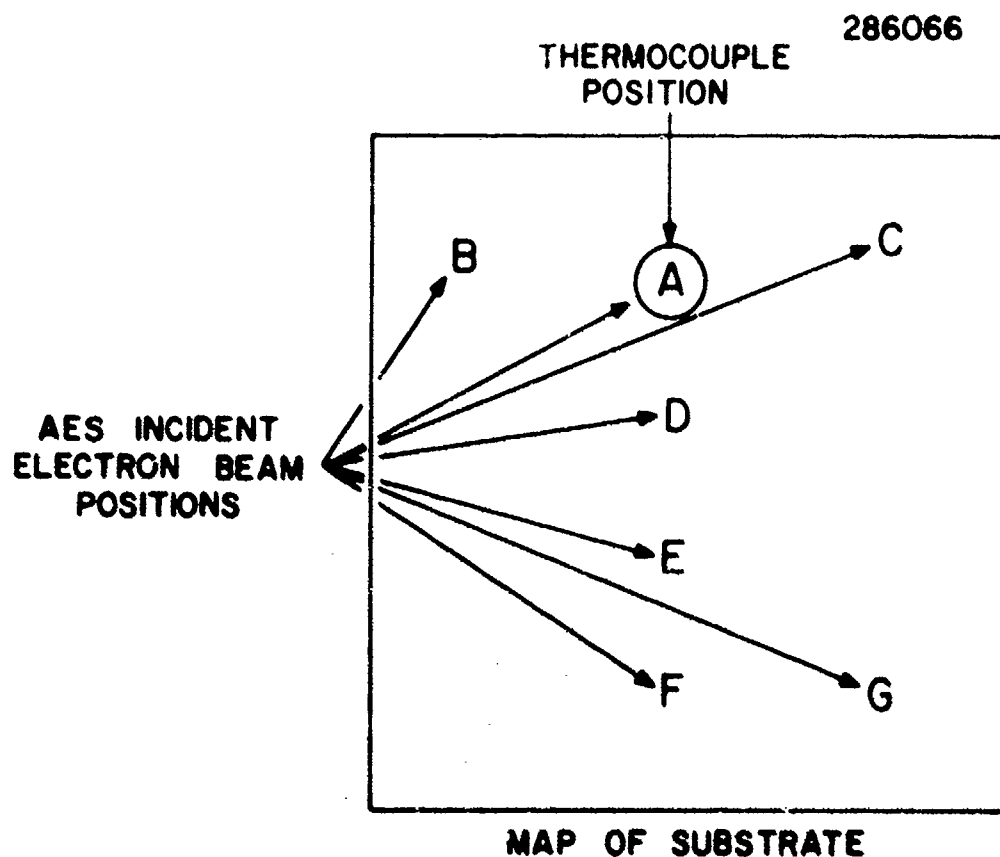


Figure 60 Spectral yield results from single crystal Na_3Sb before and after electron bombardment.



ELECTRON BEAM POSITION	THERMOCOUPLE TEMPERATURE RISE °C
A	15-16
B	15
C	15-16
D	15-16
E	14-15
F	14
G	14

Figure 61 Map of substrate showing position of electron beam for AES analysis.

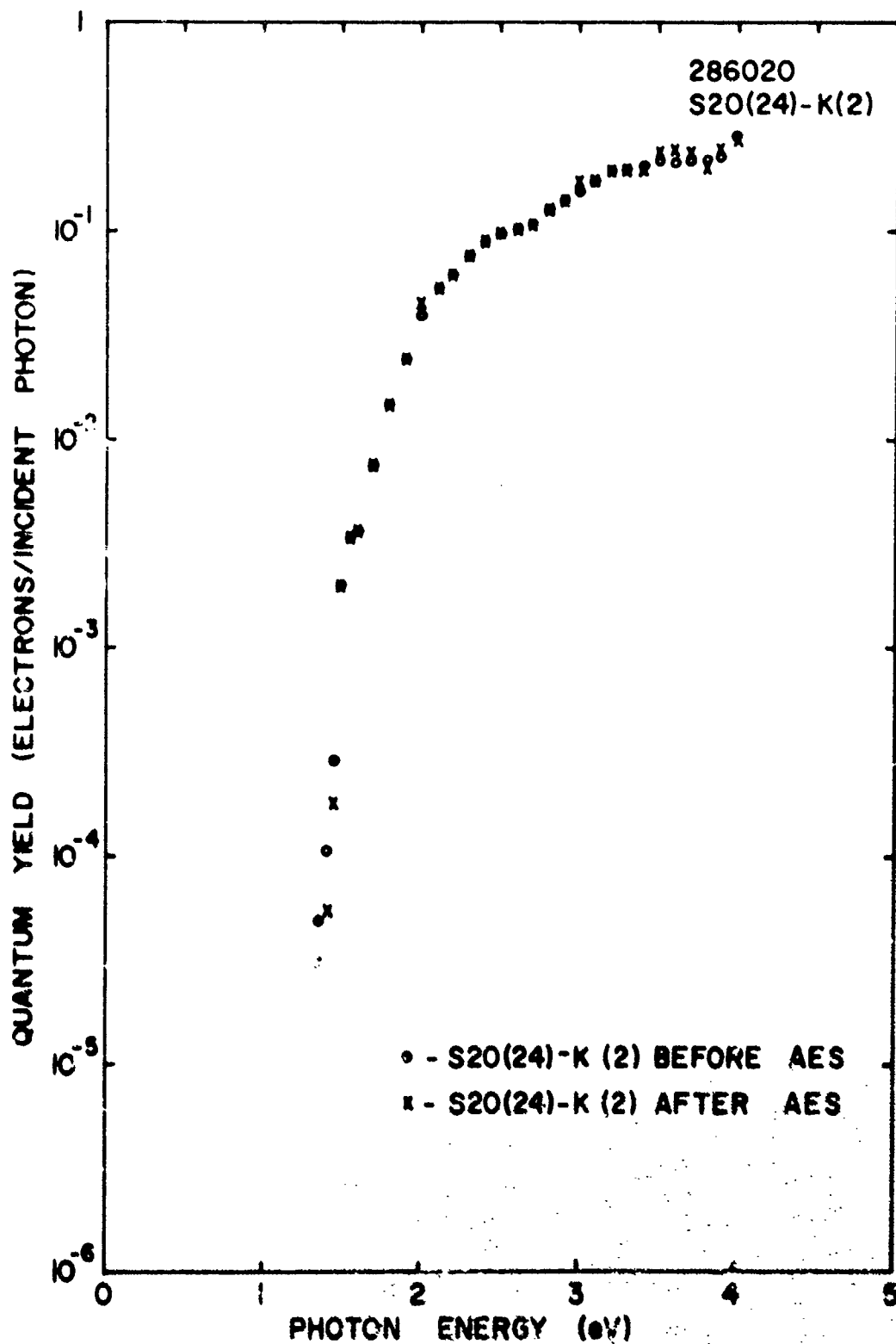


Figure 62. Stability of spectral yield of S20(24)-K(2) under electron bombardment.

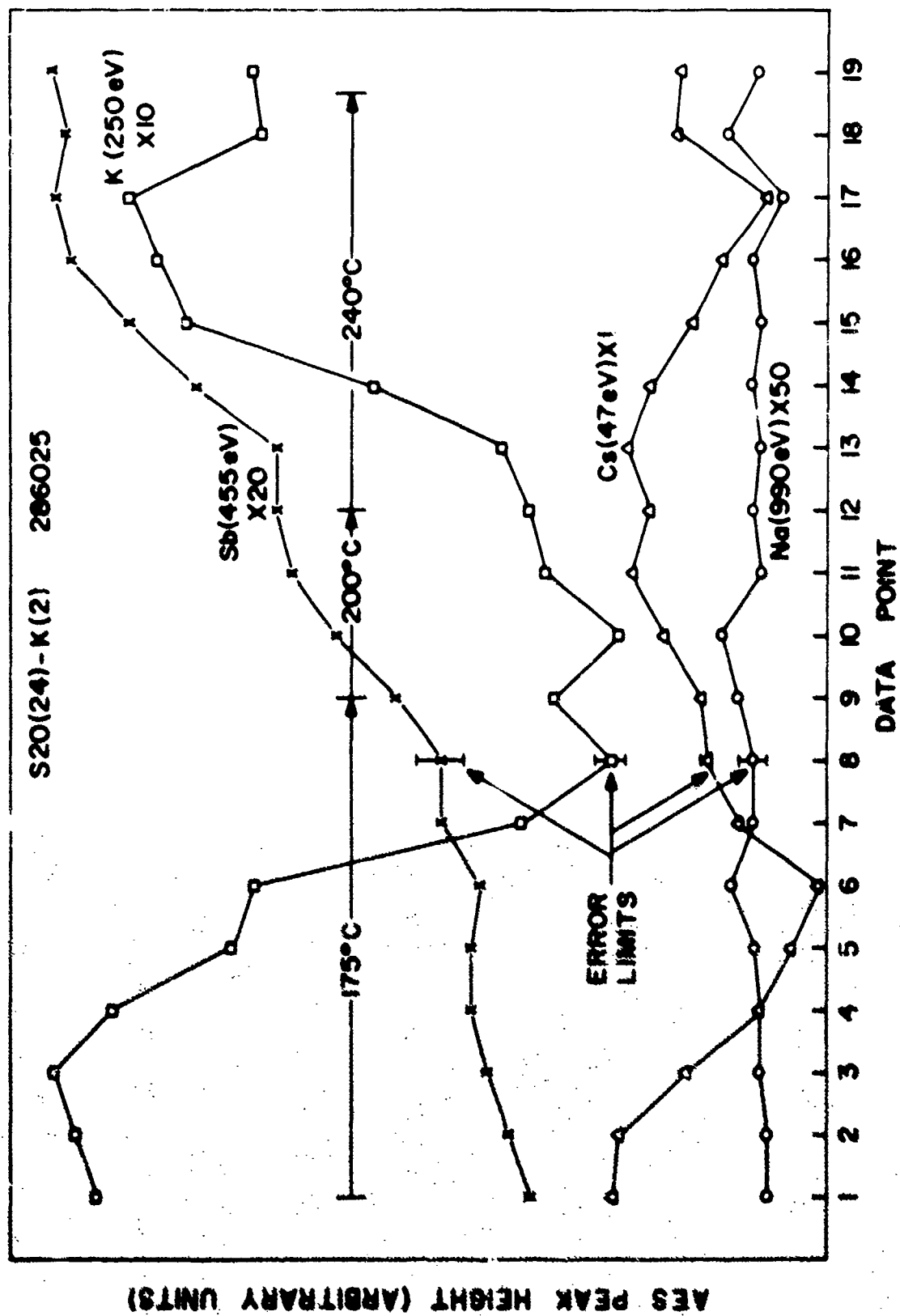
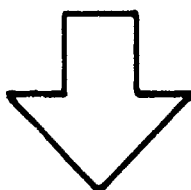


Figure 63 Summation of AES peak height changes due to heating S20(24)-K(2).

Data Point	Event Preceding Data Point
1	K(2) Deposition
2	Heating 175°C (0:10) (Hrs:Min)
3	Heating 175°C (1:00)
4	Heating 175°C (1:00)
5	Heating 175°C (1:00)
6	Heating 175°C (1:15)
7	Heating 175°C (2:25)
8	Heating 175°C (2:40)
9	Heating 175°C (1:00)
10	Heating 200°C (1:00)
11	Heating 200°C (2:55)
12	Heating 200°C (1:30)
13	Heating 240°C (0:15)
14	Heating 240°C (1:00)
15	Heating 240°C (1:00)
16	Heating 240°C (2:30)
17	Heating 240°C (1:40)
18	Heating 240°C (3:00)
19	Heating 240°C (10:05)

Figure 64 Schedule of heating temperatures and duration of heating periods for S20(24)-K(2).

$K(2) + Cs$
$Sb(3)$
$Na(1)$
$Sb(2)$
$K(1) + Cs$
Sb



$K_3 Sb + Cs$
$Na_3 Sb$
$K_3 Sb + Cs$

Figure 65A Pictorial representation of S20(24) deposition schedule through K(2) deposition.

Figure 65B Pictorial representation of assumed layering of S20(24)-K(2) before heating.

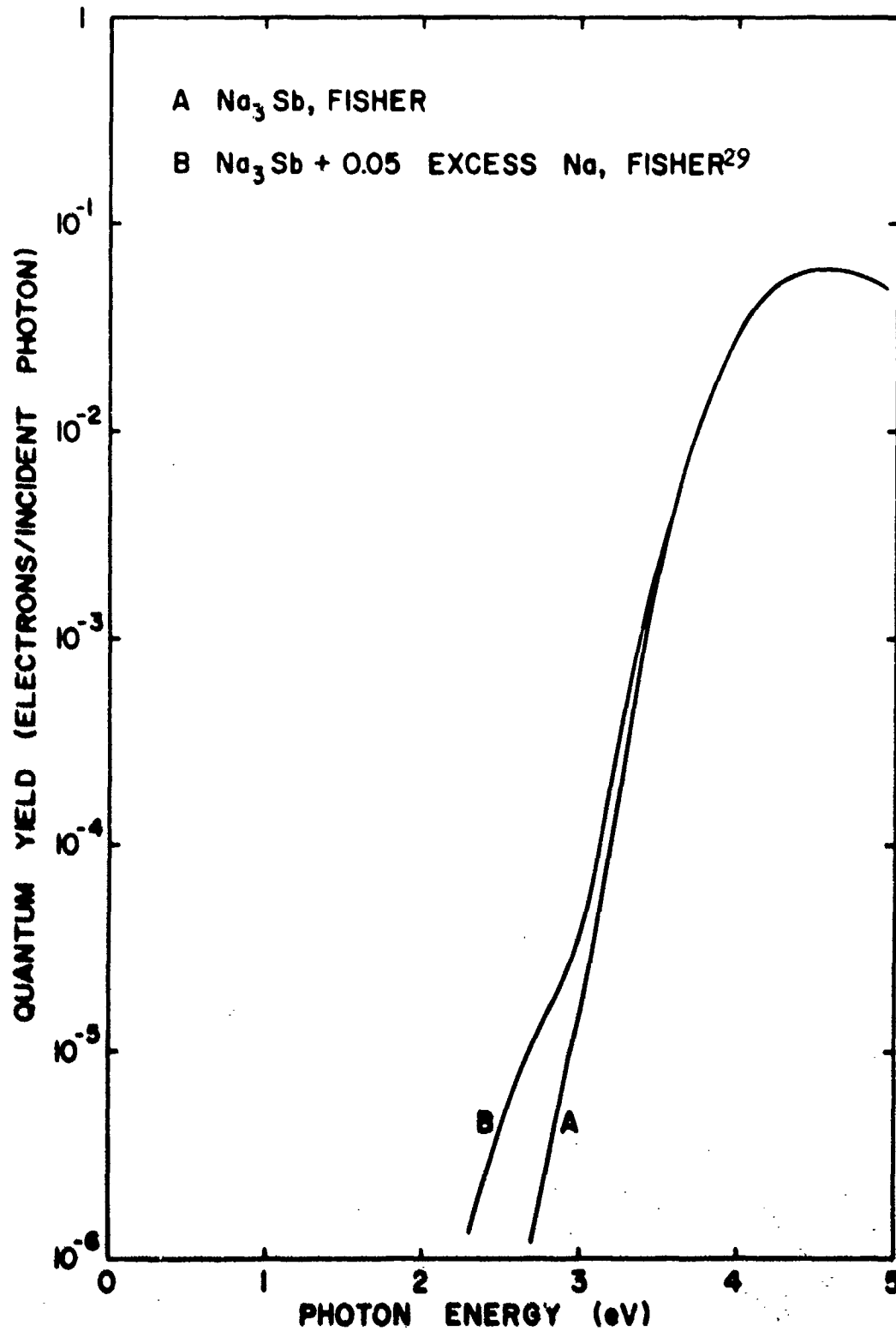


Figure 66 Spectral yield of Na_3Sb .

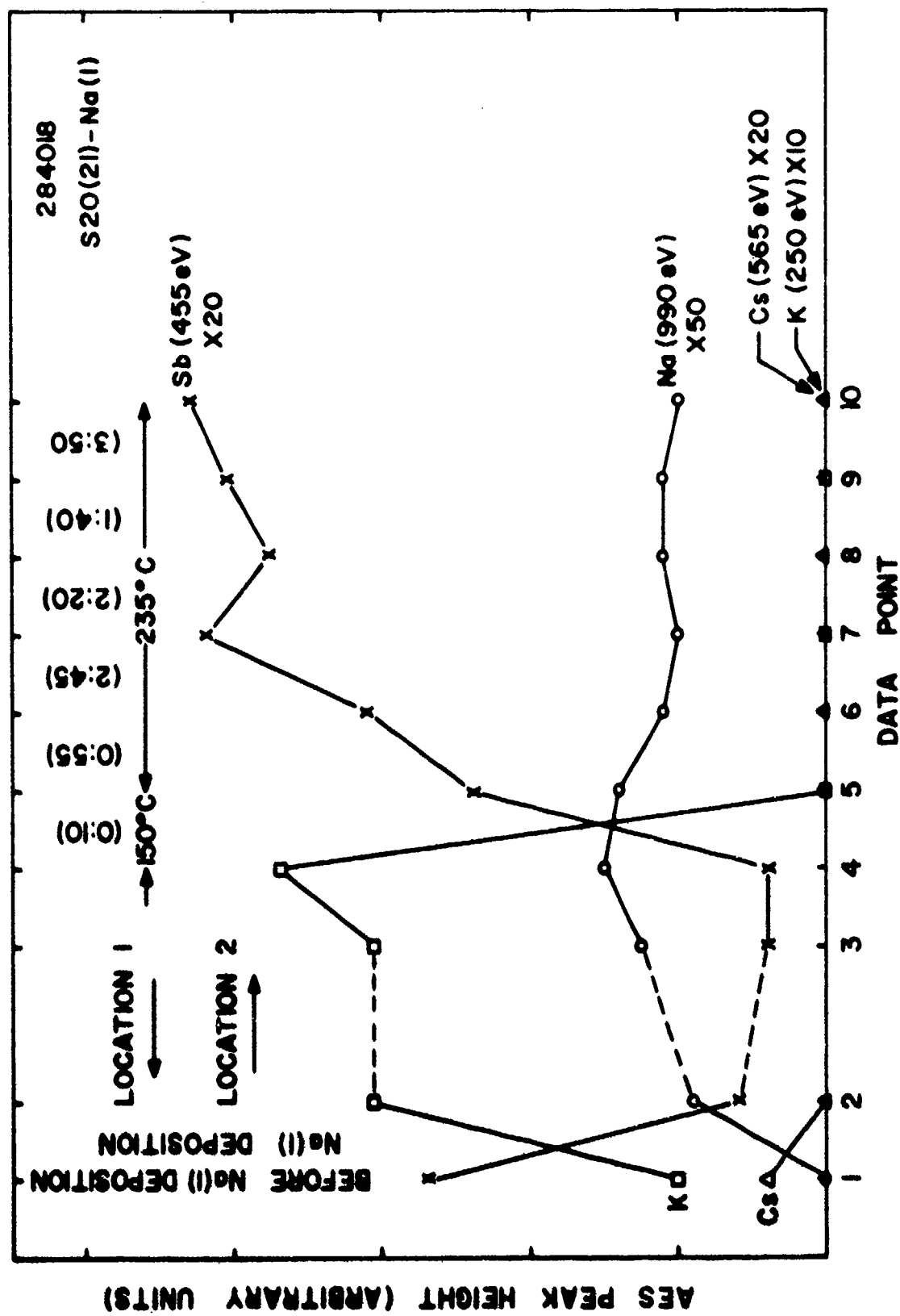


Figure 67 Summation of AES peak height changes due to Na(I) deposition on and subsequent heating of S20(21)

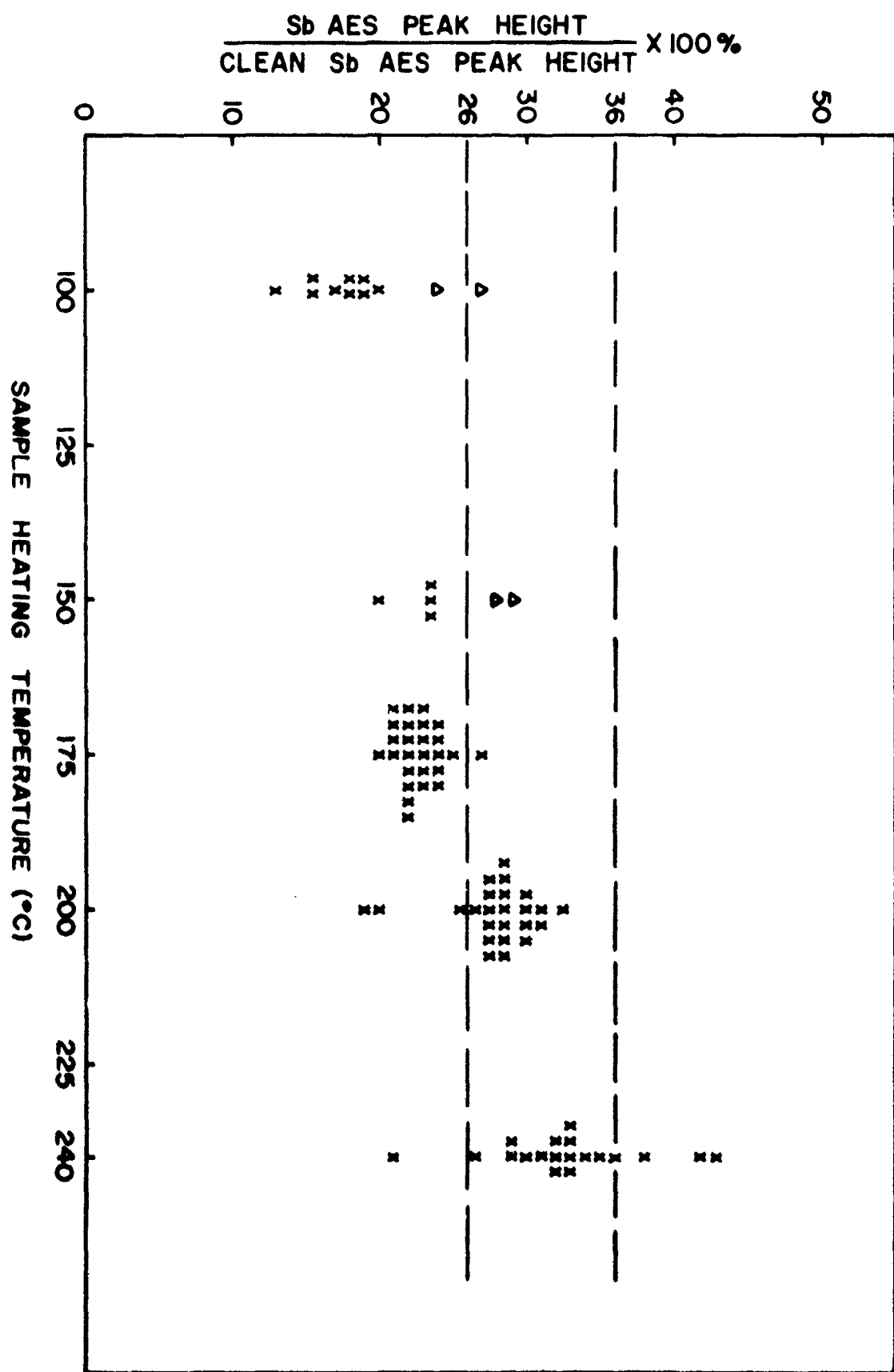


Figure 68 AES evidence of the Sb population vs. heating temperature.

Heating Temperature	Heating Period (hr:min)	
	Shortest	Longest
100°C	(3:45)	(29:30)
150°C	(0:10)	(20:40)
175°C	(0:10)	(25:25)
200°C	(1:00)	(23:30)
240°C	(0:15)	(26:30)

Figure 69 Variation in duration of heating periods.

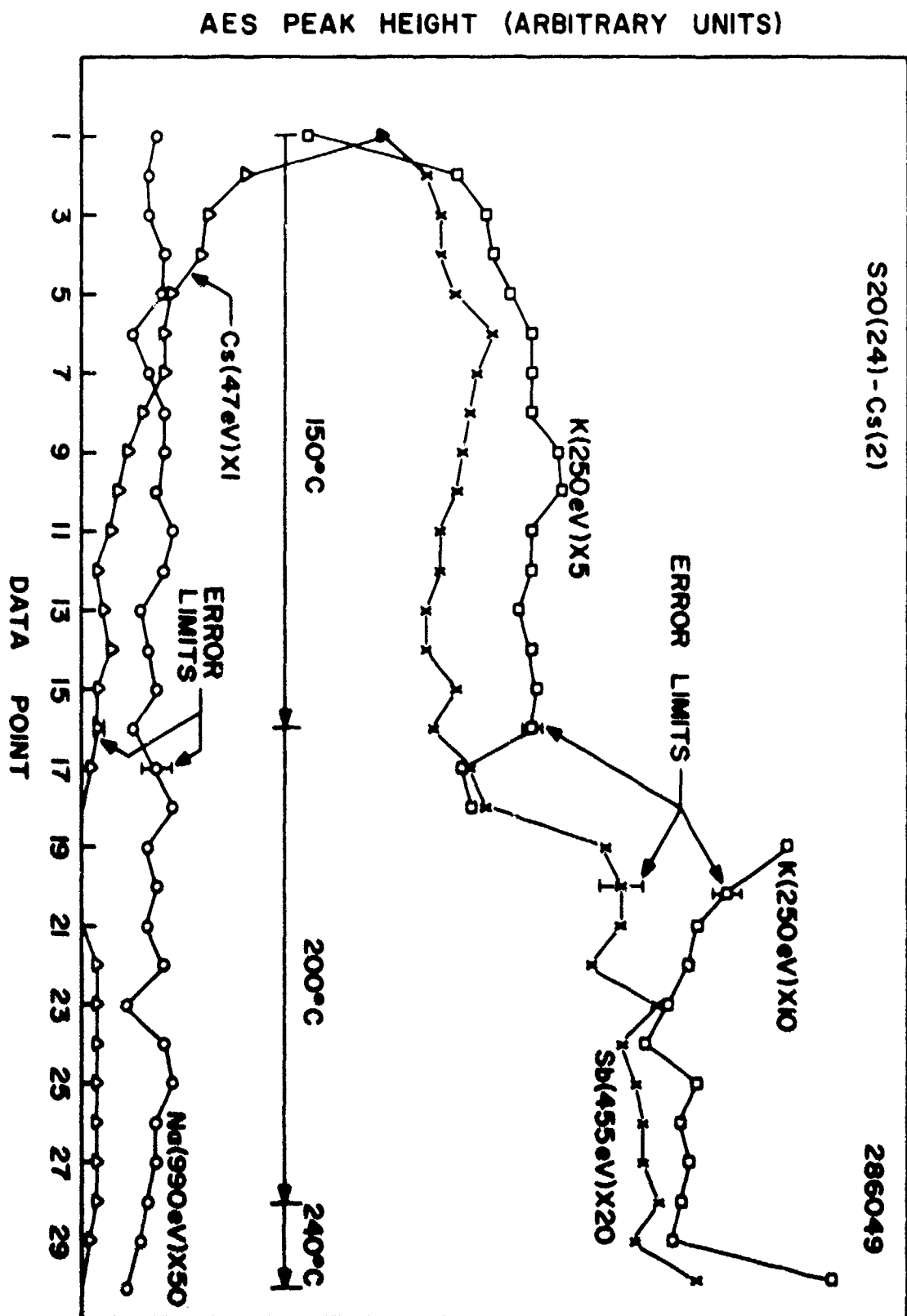


Figure 70 Summation of AES peak height changes with heating of S20(24)-Cs(2).

Data Point	Event Preceding Data Point
	Cs(2)-DEPOSITION
1	HEATING 150°C (0:30) (Hrs:Min)
2	HEATING 150°C (0:30)
3	HEATING 150°C (0:30)
4	HEATING 150°C (0:30)
5	HEATING 150°C (0:30)
6	HEATING 150°C (0:30)
7	HEATING 150°C (0:30)
8	HEATING 150°C (0:30)
9	HEATING 150°C (0:30)
10	HEATING 150°C (0:30)
11	HEATING 150°C (1:00)
12	HEATING 150°C (1:00)
13	HEATING 150°C (1:00)
14	HEATING 150°C (1:00)
15	HEATING 150°C (1:30)
16	HEATING 200°C (1:00)
17	HEATING 200°C (1:00)
18	HEATING 200°C (1:00)
19	HEATING 200°C (1:00)
20	HEATING 200°C (1:00)
21	HEATING 200°C (1:00)
22	HEATING 200°C (1:00)
23	HEATING 200°C (1:00)
24	HEATING 200°C (1:00)
25	HEATING 200°C (1:00)
26	HEATING 200°C (2:00)
27	HEATING 200°C (17:30)
28	HEATING 240°C (5:00)
29	HEATING 240°C (18:10)
30	

Figure 71 Schedule of heating temperatures and duration of heating periods for S20(24)-Cs(2).

AES PEAK HEIGHT (ARBITRARY UNITS)

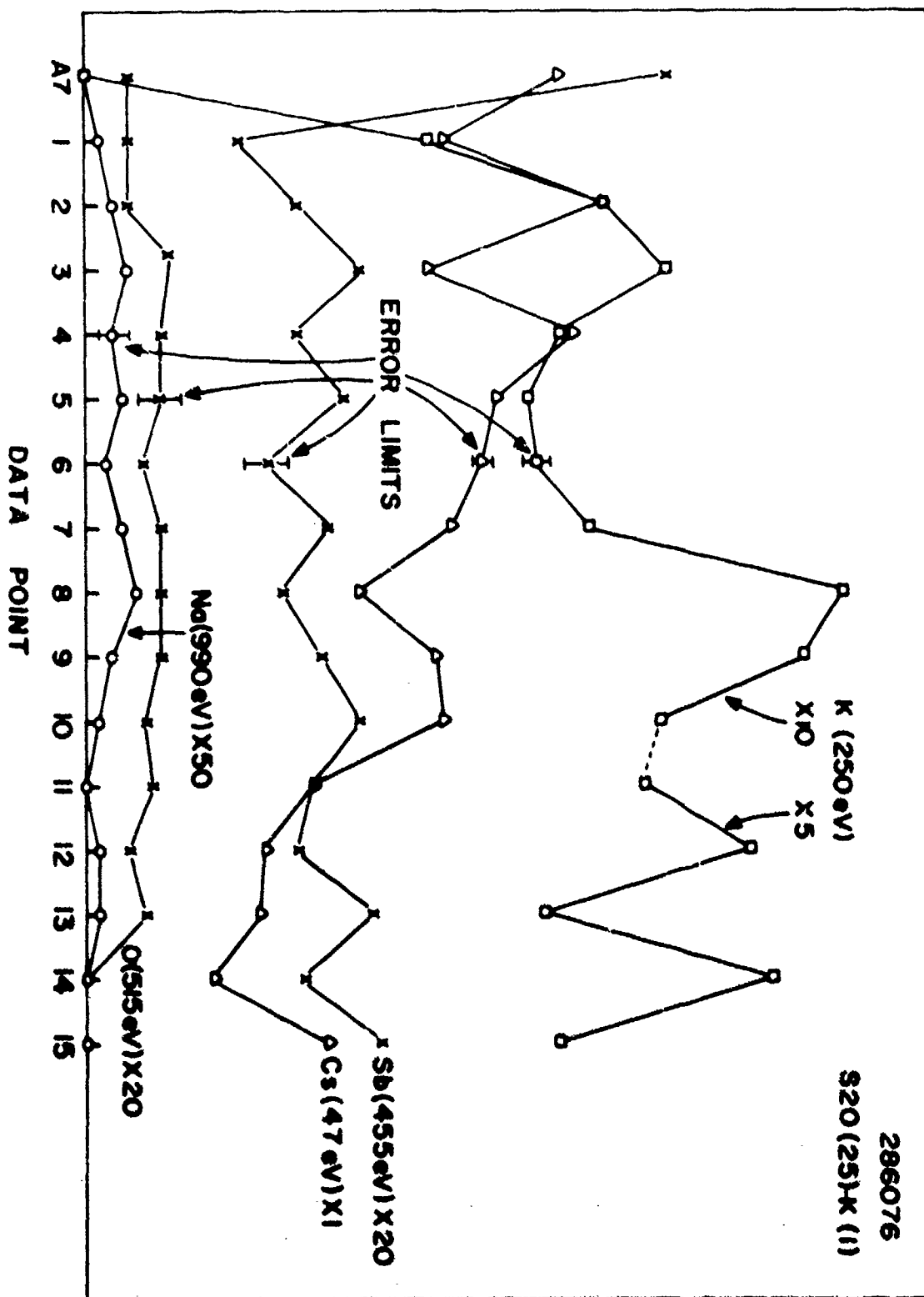


Figure 72 Summation of AES peak height changes due to K(L) depositions and heating of S20(25).

Data Point	Event Preceding Data Point	
A7	HEATING	240°C (19:35) (Hrs:min.)
1	K(1) DEPOSITION	(100°C)
2	K(1) DEPOSITION	(100°C)
3	HEATING	100°C (17:00)
4	K(1) DEPOSITION	(100°C)
5	HEATING	100°C (3:45)
6	K(1) DEPOSITION	(150°C)
7	HEATING	100°C (10:30)
8	S(1) DEPOSITION	(22°C)
9	K(1) DEPOSITION	(22°C)
10	HEATING	100°C (20:00)
11	K(1) DEPOSITION	(22°C)
12	K(1) DEPOSITION	(22°C)
13	HEATING	100°C (23:00)
14	K(1) DEPOSITION	(22°C)
15	HEATING	100°C (39:30)

Figure 73 Schedule of depositions, heating temperatures, and duration of heating periods for S20(25)-K(1).

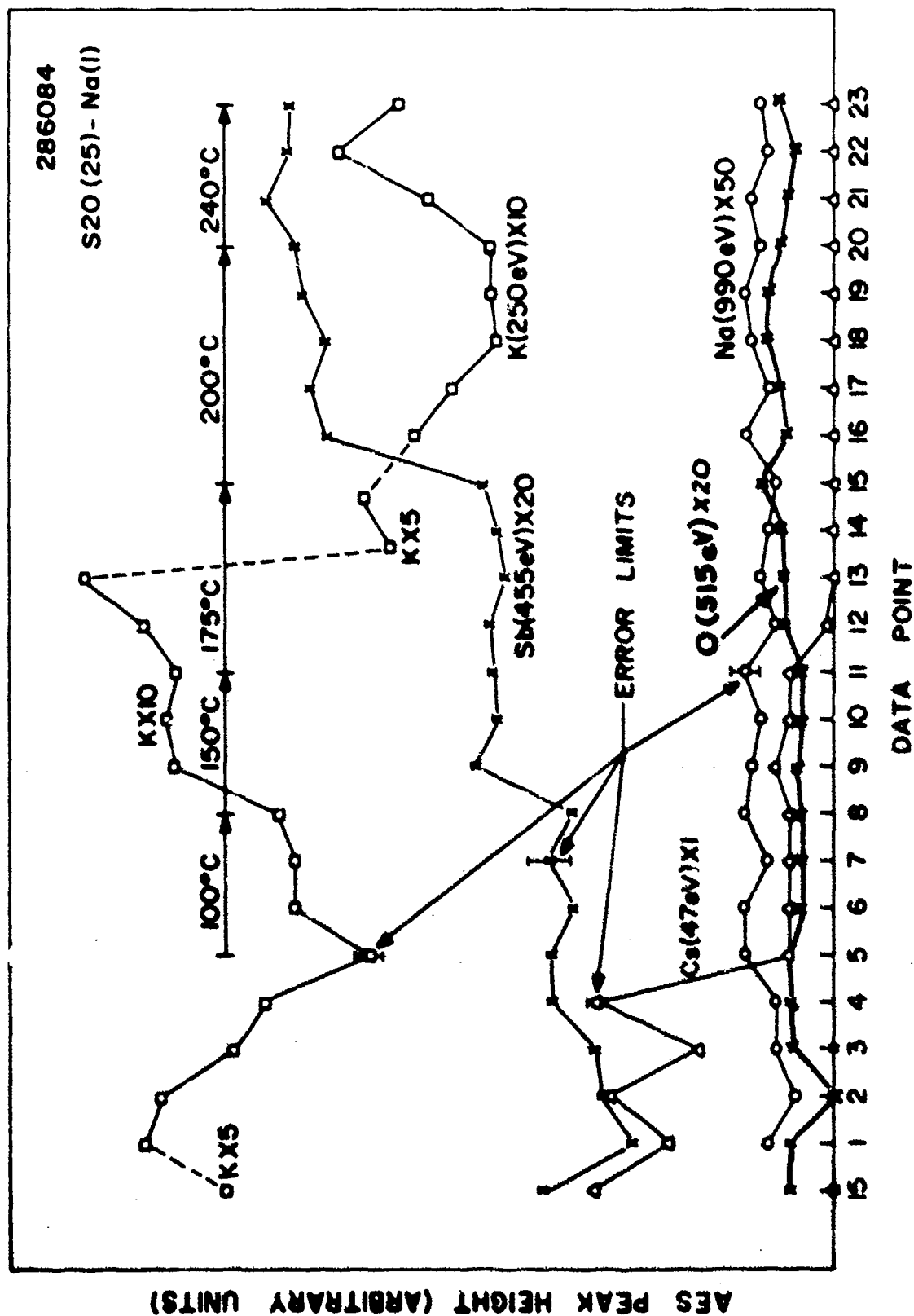


Figure 7b Summary of AES peak height changes with Na(1) deposition and heating of S2O(25).

Data Point	Event Preceding Data Point	
15	HEATING	(39:30) (Hrs:Min)
1	Na(1) DEPOSITION	
2	HEATING 100°C	(1:00)
3	Na(1) DEPOSITION	
4	HEATING 100°C	(16:15)
5	Na(1) DEPOSITION	
6	HEATING 100°C	(19:30)
7	HEATING 100°C	(4:10)
8	HEATING 100°C	(19:35)
9	HEATING 150°C	(15:15)
10	HEATING 150°C	(4:00)
11	HEATING 150°C	(16:30)
12	HEATING 175°C	(25:25)
13	HEATING 175°C	(3:00)
14	HEATING 175°C	(17:40)
15	HEATING 175°C	(7:20)
16	HEATING 200°C	(11:30)
17	HEATING 200°C	(3:00)
18	HEATING 200°C	(16:30)
19	HEATING 200°C	(6:30)
20	HEATING 240°C	(13:00)
21	HEATING 240°C	(24:45)
22	HEATING 240°C	(26:30)
23	HEATING 240°C	(23:30)

Figure 75 Schedule of depositions, heating temperatures, and duration of heating periods for S20(25)-Na(1).

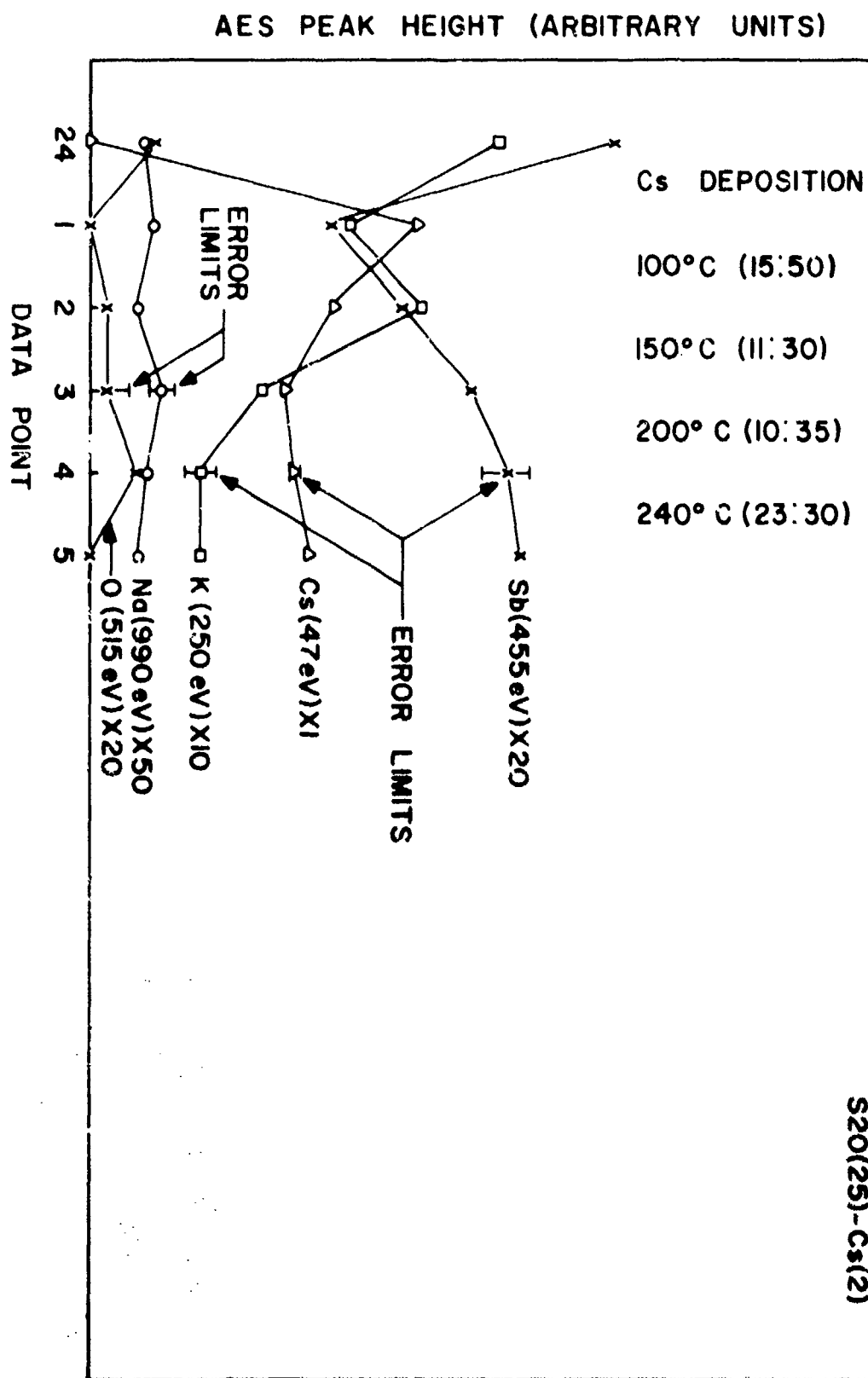


Figure 76 Summation of AES peak height changes with heating of S20(25)-Cs(2)

286092
S20(25)-Cs(2)

Sample	Figure Number	Data Point	Heating Temperature (Maximum)	Duration of Heating Period at Maximum Temperature (hrs:min)	Alkali Present at end of Heating
S20(21)-Na(1)	67	10	240°C	(11:30)	Na
S20(24)-K(2)	63-64	19	240°C	(27:30)	Na, K, Cs
S20(24)-Cs(2)	70-71	30	240°C	(23:10)	Na, K
S20(25)-Cs(1)	49-50	A7	240°C	(37:30)	Cs
S20(25)-K(1)	72-73	15	100°C	(39:30)	K, Cs
S20(25)-Na(1)	74-75	23	240°C	(87:30)	Na, K
S20(25)-Cs(2)	76	5	240°C	(23:30)	Na, K, Cs

Figure 77 Alkali specie(s) remaining in samples after maximum temperature heating of samples.